Reservoir Simulation for Play-based Development of Low Enthalpy Geothermal Resources: Application to the Delft Sandstone

Author:
Duncan Perkins
4755596

In partial fulfilment of the requirements for the degree:
MSc Applied Earth Sciences: Petroleum Engineering and Geoscience

School of Civil Engineering and Geoscience
Technische Universiteit Delft

Academic Supervisors:
Dr. F. Vossepoel (TU Delft) - **Lead Supervisor**
Dr. D. Voskov (TU Delft)
Y. Wang (TU Delft)

Industry Supervisors:
Roel Dirkx (IF technology)
Nick Buik (IF technology)
Barbara Cox (Hydreco)

Defence Comittee:
Dr. F. Vossepoel (TU Delft)
Dr. D. Voskov (TU Delft)
Dr. P. Vardon (TU Delft)

Date:
October 7, 2019

Abstract

As implementation of deep geothermal energy projects in the Netherlands increases, reservoir simulation for these geothermal systems stands to play a key role in understanding how these systems will behave and how large scale projects can be optimised to save cost and reduce risk. In this thesis, an extensive simulation study has been conducted using a new Operator based linearisation simulator (DARTS) on a geological model of the Delft Sandstone Member within the West Netherlands Basin (a prolific geothermal reservoir). The first section of the study outlines the construction of a representative geological model of the Delft Sandstone in Petrel using core, well log and seismic data. The model is quality checked by comparing derived model values with both values recorded in the literature and data from well tests. Following this, a sensitivity and uncertainty study was conducted which examines the effect of changing a wide range of model values and inputs on the thermal performance of production wells. A well placement study was then implemented, examining how well configuration, orientation and distance can affect well performance. Finally, a considerable section of the thesis investigates the role of non-reservoir lithologies in geothermal reservoir simulation and how the heat transfer from these lithologies can be accounted for utilising multi-scale upscaling.

The findings of the uncertainty and sensitivity analysis suggest that the primary uncertainty for simulation in the Delft Sandstone is the porosity and intrinsically linked permeability, with the value and spatial distribution of these properties having the largest effect on thermal performance of wells (10's of years difference in thermal breakthrough). From the well placement study, it was found that different well configurations performed variably according to local reservoir conditions (especially reservoir dip) and that optimum configuration should be decided on a case-by-case basis. It was also found that both well separation/interference and orientation have a key role in controlling the thermal productivity of wells. Finally, the section on non-reservoir lithologies finds that firstly, thermal recharge of injected water from these rocks can have a very large effect on thermal breakthrough time (10's of years for low N/G reservoir) and must not be ignored in geothermal simulations and secondly, of the three multi-scale upscaling methods implemented to more efficiently simulate conductive heat flux from the non-reservoir rocks, only multiple sub-region upscaling shows significant promise in terms of accurately accounting for heat flux and significantly reducing the number of grid cells. However, the quality of the solution for this method is still strongly linked to fluid flow rate, with higher rates resulting in better solutions.

Acknowledgements

I would firstly like to extend my thanks to Femke Vossepoel for acting as lead supervisor for this project. The advice and counsel I have received have been integral to the success of the thesis. Secondly, I would like to thank Denis Voskov, his knowledge of reservoir simulation and DARTS has proved invaluable and he has shown great tenacity in answering my long list of questions and enquiries. I would also like to thank Yang Wang, who like Denis, has been a great help in resolving technical difficulties involving reservoir simulation. Thanks is also given to Phil Vardon for his role on the defence committee and for providing useful and informative feedback on the project.

I would then like to extend my thanks and appreciation to everyone at IF technology for making me feel so welcome during my time working there. I would especially like to thank Roel Dirkx, Nick Buik and Lara Borst both for imparting with me their excellent technical knowledge and for their companionship (I will not forget the business trip to Leuven any time soon). Additionally, I would like to thank Barbara Cox for her role in orchestrating the industry side of the project and providing the necessary data.

Finally, I would like to thank my friends and family. Special thanks goes to my girlfriend, Ellen Lynch for always being there for me and of course to my parents, whose continued support has made all of this possible.

Contents

List of Figures

List of Tables

1 Introduction

1.1 Purpose and Aims

With the global temperature rising at a rate of 0.15 - 0.2^{o}C/decade and the economic and societal effects of climate change becoming more apparent, many governments are looking at how they can reduce emissions (Hansen et al., 2006). The Dutch government is no exception, having pledged to reduce green house gas emissions by 40% in 2030 and 90% in 2050 (*Netherlands Climate Policy* 2019). Currently, 91% of the Netherlands' energy comes from the combustion of fossil fuels and of that 91%, 36% comes from the combustion of natural gas (Figure 1a). Furthermore, Figure 1b shows which sectors use the natural gas. Nearly half of all the natural gas (48.5%) is used in domestic heating (*Gebouwde omgeving*) and for heating in agriculture (*Landbouw*) (*ING Economics Department* 2018). One of the major challenges facing the Dutch government is how to resolve this issue of heat supply and therefore reduce the Netherlands' reliance on natural gas. One of the proposed solutions is the use of geothermal energy.

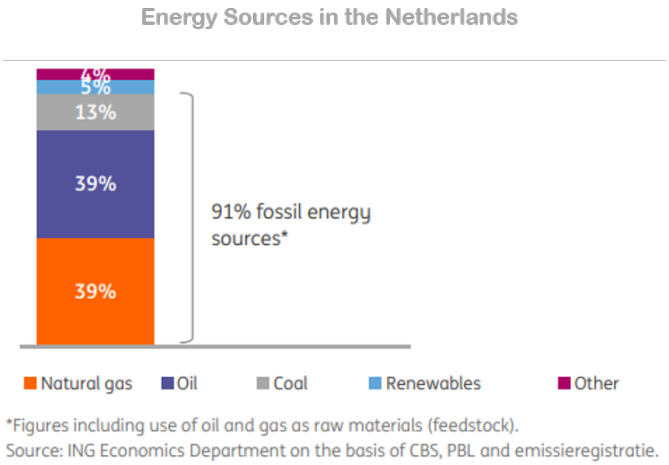

(a) Energy sources for the Netherlands

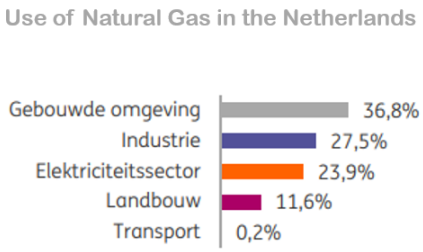

(b) Sector Usage of Natural Gas

Figure 1: Dutch energy sources (*ING Economics Department* 2018).

Geothermal energy is the utilisation of the Earth's natural heat as a source of energy. When referring to geothermal energy systems, there are three varieties:

- **High Enthalpy Geothermal Systems**: In these systems the reservoir fluid is above ~150^{o}C and is hot enough for electrical power generation. In the Netherlands, due to the steep geothermal gradient, these systems only occur at depths referred to as ultra-deep (>4km) and research into this is at a very early stage (Chandrasekharam and Bundschuh, 2008)
- **Low Enthalpy Geothermal Systems**: In these systems the temperature is lower than ~150^{o}C and in the Netherlands tends to range from 50-100^{o}C at depths of 1-4km. These temperatures are not hot enough for power generation but can be used with heat exchangers in heating networks (Chandrasekharam and Bundschuh, 2008). These systems are the topic of this thesis.
- **Shallow Geothermal systems**: Low energy systems at depths less than 0.5km. Shallow geothermal systems include ground source heat pumps and heat storage systems.

Low enthalpy geothermal energy tends to be produced using a geothermal doublet system connected to a heating network. The set up of a geothermal doublet is given in Figure 2. Two wells are drilled into a reservoir layer which is both deep enough to be of a sufficient temperature and permeable enough to allow flow of fluid through the rock. Cool water is pumped down the injection well into the reservoir, it then flows towards the producer well and as it does it accumulates heat from the rocks. This hot water is then pumped up the producer well. After being degassed and filtered, the hot water from the reservoir is then taken to a heat exchanger and used to heat fresh water in a heating network. The cooled down reservoir water is then returned to the reservoir via the injector well and the cycle continues.

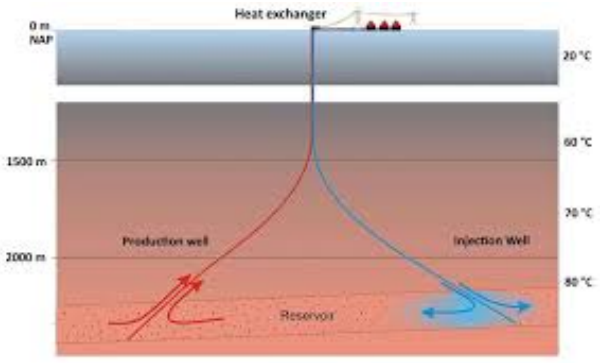

Figure 2: Geothermal doublet system (Groot, 2014).

Utilising low enthalpy geothermal energy for heating has a number of advantages over using other renewable energy sources:

1. **Efficiency** - Heat from water can be used directly to heat houses instead of inefficiently converting electricity to heat.

2. **Consistency** - Whilst some forms of renewable energy (wind and solar) may have to be supplemented by the grid in unfavourable weather conditions, geothermal energy gives a relatively constant supply of heat.

These advantages, combined with the fact that geothermal projects do not require much space (maximum of a football field, and only whilst drilling) and the energy production potential is large, means that geothermal power is being looked at as a serious contender for supplying industrial and domestic heat in the Netherlands (*Master Plan: Geothermal Energy in the Netherlands* 2018). To date, 17 deep, low-enthalpy geothermal projects have been realised in the Netherlands, with the vast majority being developed in the area surrounding Den Haag for the heating of greenhouses as shown in Figure 3 (*Master Plan: Geothermal Energy in the Netherlands* 2018). However, the first geothermal doublets for district heating are also starting to come online (Werker et al., 2017). In terms of future development, the government aims to to have 175 doublet pairs drilled by 2030, providing 50PJ of energy and 700 pairs drilled by 2050, providing 200+PJ of energy. If this is realised, low enthalpy geothermal energy production stands to become a significant industry in its own right (*Master Plan: Geothermal Energy in the Netherlands* 2018).

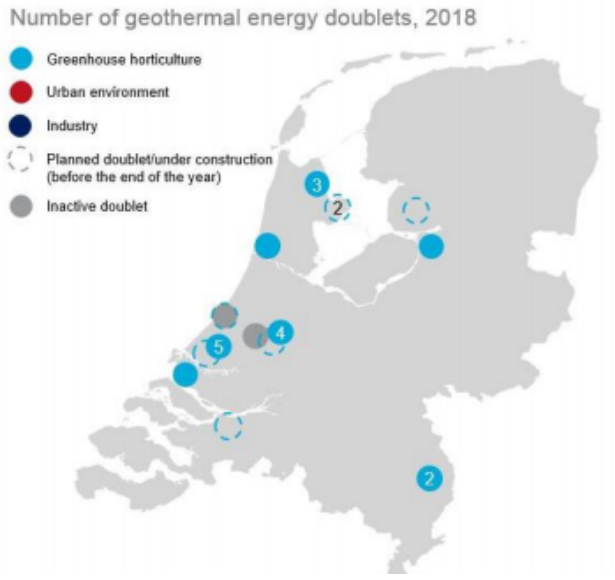

Figure 3: Location of all realised and planned deep geothermal projects in the Netherlands (*Master Plan: Geothermal Energy in the Netherlands* 2018).

One of the issues surrounding the wide-scale implementation of geothermal energy is the economic risks associated with the projects. As the cost of drilling wells to the depths economical for low enthalpy geothermal energy is high and the product being produced is not particularly valuable (at least in comparison to oil or gas), the profit margins are not very large. This is demonstrated in Figure 4, which is a Net Present Value vs time plot for a simulated geothermal project (Dongen, 2019). It is therefore very important for geothermal projects that doublets perform with optimum efficiency and that any uncertainties surrounding performance are well understood. One of the proven ways to reduce risks associated with geothermal developments and increase well performance is to use a 'play' or portfolio based approach. In a portfolio based approach, a given geothermal system is analysed as a whole and information gained from any developments are used to de-risk any future projects. Additionally, a portfolio based approach allows for larger scale and more efficient implementation of geothermal systems compared to individual projects, as well as the ability to continually improve and optimise processes as a development continues (Veldkamp et al., 2019).

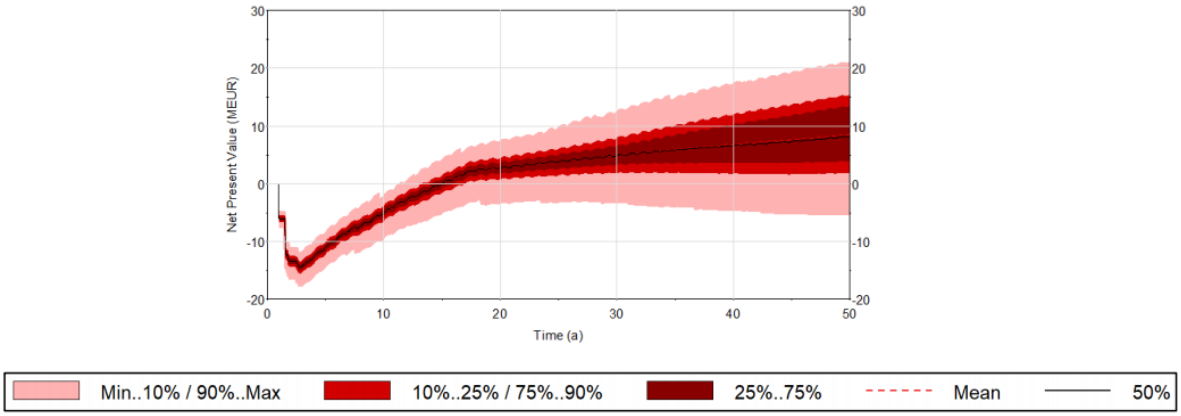

Figure 4: NPV vs time for a simulated geothermal development (Dongen, 2019).

A key aspect of implementing a portfolio based approach to geothermal systems is to try and predict how these systems will behave on a large scale. The primary way of doing this to build reservoir models based on geological data and perform numerical flow simulations, which then tell you how the system will perform. However, one of the major problems with reservoir simulation as a tool is understanding how accurate a model is, how sensitive the model is to changes in input parameters and how uncertain a given model is in terms of its spatial distribution of properties (reservoir architecture, porosity distribution etc.). The primary aim of this thesis is to investigate the sensitivity and uncertainty associated with geothermal reservoir simulations conducted on a geological model of a real, large-scale geothermal reservoir: The Delft Sandstone. In particular, the following research questions shall be addressed:

- Which geological input parameters are the most important in influencing the cold water thermal breakthrough time (referred to from here on in as thermal breakthrough)?
- How much uncertainty (in terms of thermal breakthrough time) is associated with possible variations in reservoir architecture and porosity distribution?
- How might well placement, doublet configurations and doublet orientation effect well performance?

Although uncertainty studies on oil and gas fields are commonplace, the utility of this work is based on the fact that to date, very few studies have applied these methods to low-enthalpy geothermal projects and those that have, for example Shetty et al. (2017), Wang et al. (2019) and Crooijmans et al. (2016), tend to use synthetic reservoir models not based on real subsurface data. Therefore, the application of these techniques to a large scale realistic reservoir model represents an important step in reservoir simulation of low enthalpy geothermal systems.

The secondary aim of the thesis is to examine the role of non-reservoir lithologies in low enthalpy geothermal systems and to investigate ways in which the effects of non-reservoir lithologies can be

accounted for whilst reducing the need for very large simulation grids. To date, the role of impermeable rocks in geothermal reservoirs and their influence on thermal front propagation through the reservoir has been generally overlooked. Similarly, the application of multi-scale upscaling methods is widespread in the field of oil and gas, however, application of these methods to modelling conduction from non-reservoir lithologies has not yet been investigated. As such, the research conducted in this project represents an important starting point for further research into these fields.

The thesis itself can be broken down into six main sections which together cover the research objectives:

1. A literature review covering the geology of the Delft Sandstone and the physics behind geothermal reservoir simulation.
2. The construction of a geological model of the Delft Sandstone and the quality testing of the model to ensure it is a realistic representation of the geology.
3. Sensitivity and uncertainty analysis: simulation experiments to determine the sensitivity of the model to geological input parameters and uncertainty associated with facies and porosity distribution.
4. A well placement study to look at optimum doublet configurations, distance and orientation.
5. Simulation experiments to determine the influence of non-reservoir lithologies on thermal recharge of injected water and to test the feasibility of upscaling non-reservoir lithologies for increasing computational efficiency.
6. Conclusions and recommendations for future work.

For the project, a reservoir model of the Delft Sandstone was constructed from seismic and well data and then simulation experiments were carried out using a reservoir simulator. To do this, two pieces of software were utilised. For the geological modelling, Petrel was used, which is a powerful and highly versatile piece of software developed by Schlumberger. For all of the simulation experiments, the Delft Advanced Research Terra Simulator (DARTS) was used. This piece of software was developed at TU Delft and has a large range of abilities, one of which is low and high enthalpy geothermal simulation.

It should be noted that this study has been conducted in collaboration with IF Technology (geothermal consultancy) and Hydreco (geothermal operator) and is an ongoing project, as such some of the information is commercially sensitive and so some of figures have been altered so as not to reveal this information.

1.2 Study Area

The target reservoir for this study is the Delft Sandstone in the West Netherlands Basin. This reservoir has a number of characteristics that make it suitable for the exploitation of low enthalpy geothermal energy. Firstly, the fact that the reservoir sits in an old rift basin, means the reservoir units can often extend to quite great depths and thus high temperatures. Secondly, there is significant urban development directly above the reservoir, meaning heat can be utilised directly above the source with minimal losses in terms of transporting heat. Finally, as can be seen in Figure 5, the area has oil and gas reserves. This means that the area has considerable amounts of subsurface data available, including 3D seismic and well log data.

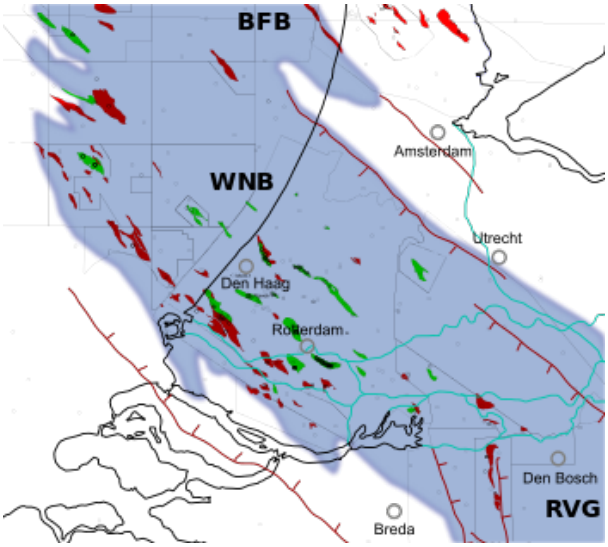

Figure 5: West Netherlands Basin and its associated oil and gas reserves (Wong et al., 2007).

The Delft Sandstone lies within three rotated half graben blocks, which from west to east are: the Westland Graben, the Pijnacker Graben and the Den Haag Graben. These are referred to repeatedly throughout the report. The size and structural layout of these half-grabens is given in Figure 6.

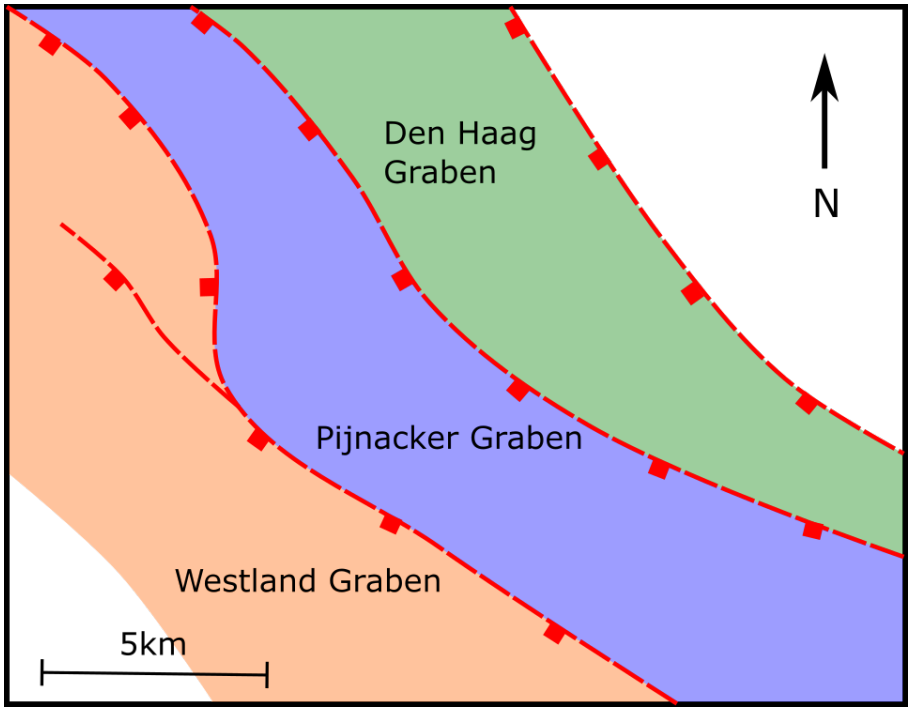

Figure 6: Simple schematic of the three half-grabens.

2 Literature review

2.1 Geology of the Delft Sandstone

The Delft Sandstone is an Upper Cretaceous fluvial reservoir found within the confines of the West Netherlands Basin. The sandstones constitute an important reservoir not only for geothermal purposes but also for oil and gas deposits in the West Netherlands Basin and for this reason it has been extensively studied in terms of depositional history and sedimentology (Wong et al., 2007; Jager et al., 1993). This section covers the geological history of the West Netherlands Basin, the facies architecture/proposed structure of the reservoir and the properties of the sandstone.

The start of the Delft Sandstone's geological history began in the late Jurassic (155Ma) when the break up of the Pangea super-continent through rifting was well underway. Rifting, which had started in the modern day North Sea in the Triassic, spread southwards and reached the Netherlands resulting in the formation of a NW-SE trending rift basin referred to as the West Netherlands Basin (WNB) (Figure 5) (Wong et al., 2007). A cross section through the WNB from SW to NE (Figure 7) shows that it consists of a complex sequence of grabens and half-grabens which formed as a result of the extensional forces associated with the rifting (Duin et al., 2006). The subsidence that accompanied the formation of the grabens and half grabens resulted in the creation of large amounts of accommodation space, into which sediments of the Nieuwerkerk Formation were deposited (Wong et al., 2007; DeVault and Jeremiah, 2002). The syn-sedimentary depositional nature of the Nieuwerkerk Formation is evident from the very variable thickness seen within the WNB, with the thickness next to major bounding faults reaching in excess of 1km and whilst the thickness on structural highs is often less than 100m (Willems, 2017; Den Hartog Jager, 1996).

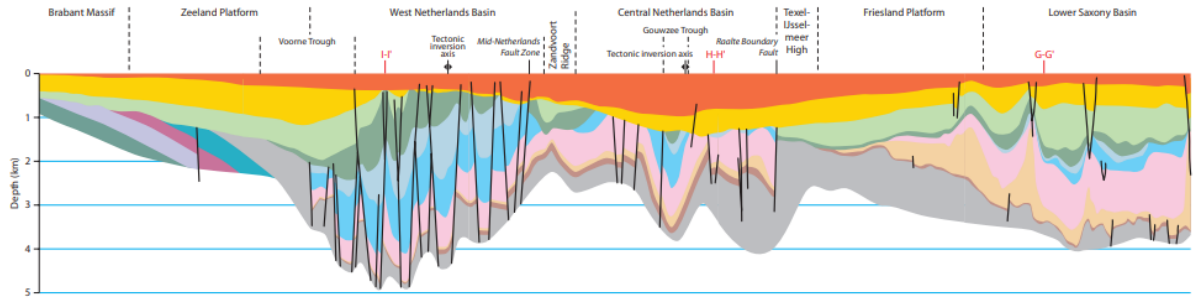

Figure 7: SW-NE cross section through the WNB and onshore Netherlands (Duin et al., 2006).

The Nieuwerkerk Formation itself is composed of three members, which from base to top are: the Alblasserdam Member, the Delft Sandstone Member and the Rodenrijs Member, although the continuity of the Delft Sandstone Member throughout the WNB brings into question whether it is indeed a single member or whether it should be classed as multiple members (Donselaar et al., 2015; Willems et al., 2017; DeVault and Jeremiah, 2002). With the exception of the Rodenrijs Claystones at the very top of the Nieuwerkerk which has some fauna indicating significant marine influence, the deposits of the Nieuwerkerk are almost exclusively fluvial in origin and were deposited by river systems flowing NW from the continental interior (DeVault and Jeremiah, 2002). The Delft Sandstone represents a high net/gross (N/G) section of the Nieuwerkerk formation when compared to the Alblasserdam Memeber or the Rodenrijs Claystones. The variation in reservoir quality between the members of the Nieuwerkerk Formation is believed to be related to the balance of accommodation space creation vs sediment supply (Donselaar et al., 2015). During times of high accommodation space creation (e.g. major rifting phases), fluvial deposits were laid down rapidly resulting in a high proportion of fine overbank deposits compared to sand (Alblasserdam Member). During times of tectonic quiescence, when the accommodation space creation and sediment supply were much more evenly matched, lateral movement of the fluvial channels displaced much more of the fine material leaving a much higher N/G reservoir (Delft Sandstone) (Donselaar et al., 2015). This concept is demonstrated in Figure 8.

Following the deposition of the Delft Sandstone Member, a major marine trangression is recorded, first with the deposition of the lagoonal and coastal plain deposits of the Rodenrijs Claystones and then by

the deposition of fully marine shales and sandstones of the Rijnland Group (Willems et al., 2017; Donselaar et al., 2015). At a similar time (Early Cretaceous), the active rifting of the WNB ceased due to the shifting of the rift axis to the west and the opening of the North Atlantic Ocean, this meant the basin went into its sag-phase and the process of slowly infilling the basin began (Wong et al., 2007). Tectonic activity in the basin did not resume until the Late Cretaceous to Early Tertiary at which point compressive forces from the Alpine Orogeny to the south caused the basin to undergo tectonic inversion. This inversion has given the WNB its anticlinal pop-up structures which make excellent structural traps for oil and gas fields (Duin et al., 2006). One of these typical structures is shown in Figure 11.

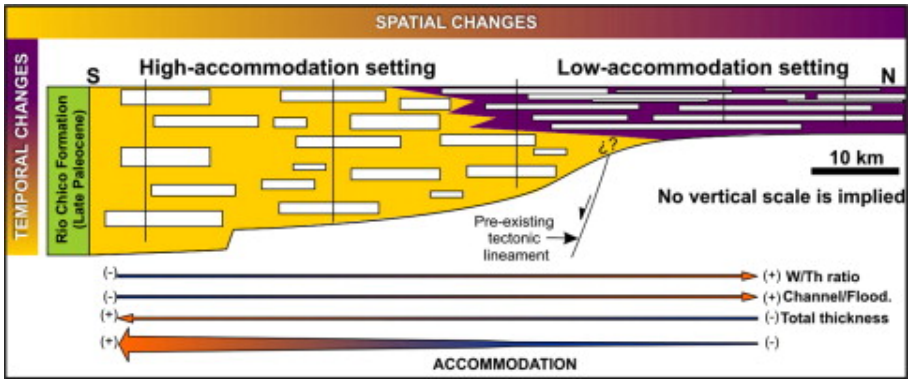

Figure 8: Fluvial reservoir architecture in different depositional settings (Foix et al., 2013).

The primary reservoir facies for the Delft Sandstone Member are point bar deposits which have been deposited on the inner loops of meander systems. These can be identified from cores and well logs which show well-defined basal erosional surfaces and a tendency to fine upwards, as is shown in Figure 9 (Wiggers, 2017). Other less common reservoir facies include crevasse splays and braided river deposits. Non-reservoir facies primarily consist of shales and clays deposited on the floodplain of the fluvial system (Donselaar et al., 2015; Wiggers, 2017).

Academic views on the internal structure of the Delft Sandstone are very varied and have changed significantly over time. Originally, Den Hartog Jager (1996) suggested the Delft Sandstone is a single continuous and relatively homogenous sandstone body which sits above the Alblasserdam Member. However wells drilled in the Delft Sandstone member show a great deal of variability depending on both vertical and lateral position within the reservoir unit. Around the city of Den Haag, wells drilled in the east of the Delft Sandstone Member tend to show that the bottom of the sandstone is sand rich and the top is sand poor whilst wells drilled in the west show the opposite (Willems et al., 2017). Recent palynological studies conducted by Willems et al. (2017) suggest that this spacial distribution of sand can be explained by the fact that the major trunk of the fluvial system moved from east to west between the different graben systems over time, resulting in deposition of sand at different vertical and lateral positions depending on the time. This system which is depicted in Figure 10, nicely explains the observed distribution of High N/G reservoir in the Delft Sandstone Member.

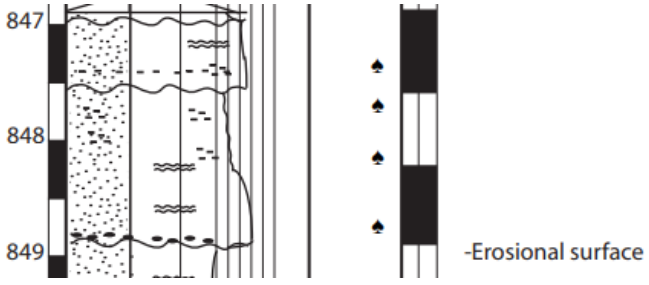

Figure 9: Sedimentary log of the Delft Sandstone made from core analysis showing clear erosional surfaces and fining upwards sequences (Wiggers, 2017).

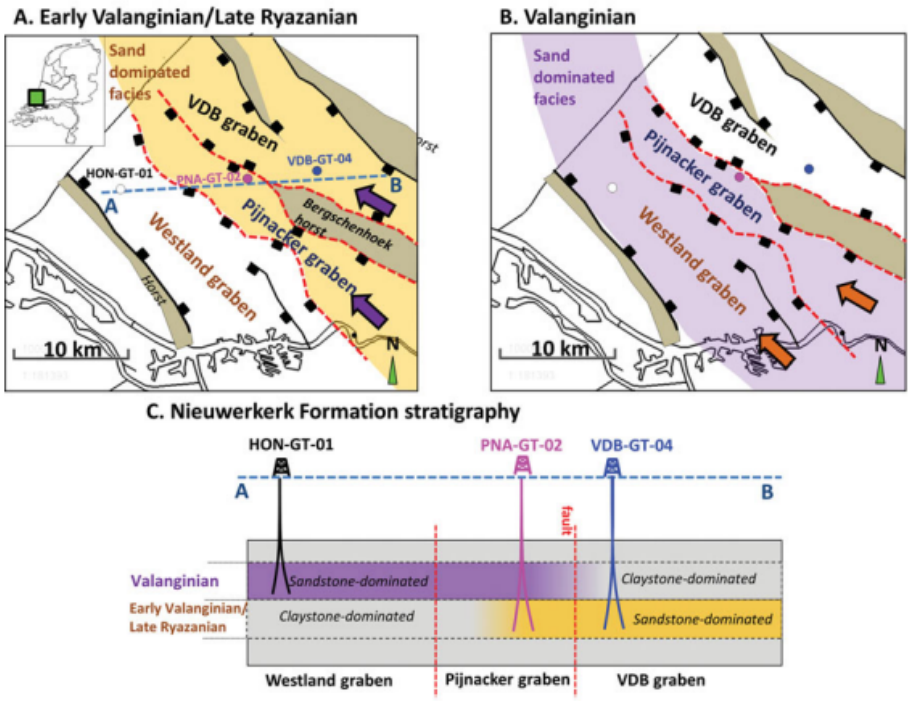

Figure 10: Migration of the Delft Sandstone's fluvial depositional system through time and how that has affected the reservoir structure and composition (Willems et al., 2017).

Although the reservoir quality of the Delft Sandstone Member is quite variable, dependant on position in the reservoir, the reservoir properties are on average quite good compared with other fluvial reservoirs. Average N/G from available well logs is reported as 0.65 and porosity for net reservoir ranges between 17 and 30% (Donselaar et al., 2015). In terms of temperature, the depth range of 2000-2300m for the reservoir gives temperatures ranging between 65-75^{o}C based on a geothermal gradient of 3^{o}C/100m (Donselaar et al., 2015).

2.2 Geothermal Reservoir Simulation

2.2.1 Governing Equations

Geothermal simulation fundamentally differs from simulation of petroleum reservoirs or groundwater in that understanding the flow of energy as well as mass in the reservoir is a necessity. This adds an added element of complexity to geothermal reservoir simulation (O'Sullivan et al., 2001). Three fundamental equations are used for geothermal reservoir simulation. These are Conservation of Mass, Conservation of Energy and Darcy's Law for fluid flow in porous media (O'Sullivan et al., 2001).

Conservation of Mass states that for a closed system, the mass of a system must remain constant over time. What this also implies, is that for an open system any change in the mass of a system must be balanced by mass coming into or out of the system. With this said, the mass balance for fluid with multiple phases and multiple components in porous media can be written as shown in equation 1. The first term is the change in mass with time, the second term describes the flux of mass in and out of the system due to flow and the third term describes a source term in case any mass is introduced or removed from the system not at the boundary, for example at a well (Khait and Voskov, 2018).

$$\frac{\delta}{\delta t}\left(\phi \sum_{j=1}^{n_p} x_{cj}\rho_j s_j\right) - \nabla \cdot \sum_{j=1}^{n_p} x_{cj}\rho_j u_j + \sum_{j=1}^{n_p} x_{cj}\rho_j \tilde{q_j} = 0 \quad c = 1, .., n_c \tag{1}$$

where:

- t = time

- ϕ = porosity
- x_{cj} = mole fraction of component c in phase j
- ρ_j = density of phase j
- s_j = saturation of phase j
- n_p = number of phases
- n_c = number of components
- q_j = source term for phase j
- u_j = Darcy velocity of phase j

Darcy's Law (equation 2) is used to determine the velocity of a fluid through porous media given the viscosity of the fluid, the permeability and the pressure gradient. For simplicity the effects of gravity are ignored.

$$u_j = K\frac{K_{rj}}{\mu_j}\boldsymbol{\nabla} p_j \tag{2}$$

where:

- K = permeability tensor
- K_{rj} = relative permeability of phase j
- μ_j = viscosity of phase j
- p_j = pressure of phase j

Conservation of Energy is very similar to conservation of mass. It has a change of energy term, a flow term and source term, the only difference being that energy moves through the subsurface via two methods: conduction and convection. Flow of heat by convection is controlled again by Darcy's law (equation 2), whilst conduction is controlled by the temperature gradient and the thermal conductivity of the material that the heat is conducting through (Khait and Voskov, 2018). This is shown in equation 3.

$$\frac{\delta}{\delta t}\left(\phi\sum_{j=1}^{n_p}\rho_j s_j U_j + (1-\phi)U_r\right) - \boldsymbol{\nabla}\cdot\sum_{j=1}^{n_p} x_{cj}\rho_j h_j u_j + \boldsymbol{\nabla}\cdot(\kappa\boldsymbol{\nabla}T) + \sum_{j=1}^{n_p} h_j\rho_j\tilde{q_j} = 0 \tag{3}$$

where:

- U_j = internal energy of phase j
- U_r = internal energy of the rock
- h_j = enthalpy of phase j

2.2.2 DARTS

Equations 1 and 3 are continuous forms of the governing equations. For reservoir simulation, the equations need to be in discretized form. In DARTS, a backwards Euler approximation in time is used for discretization (Khait and Voskov, 2018). Equations 4 and 5 show the finite volume discretized form of the conservation equations.

$$V\left[\left(\phi\sum_{j=1}^{n_p} x_{cj}\rho_j s_j\right)^{n+1} - \left(\phi\sum_{j=1}^{n_p} x_{cj}\rho_j s_j\right)^{n}\right] - \Delta t\sum_{l}\left(\sum_{j=1}^{n_p} x_{cj}^{l}\rho_j^{l}\Gamma_j^{l}\boldsymbol{\nabla}p^{l}\right) + \Delta t\sum_{j=1}^{n_p}\rho_j x_{cj} q_j = 0 \tag{4}$$

$$\begin{aligned} V\left[\left(\phi\sum_{j=1}^{n_p}\rho_j s_j U_j + (1-\phi)U_r\right)^{n+1} - \left(\phi\sum_{j=1}^{n_p}\rho_j s_j U_j + (1-\phi)U_r\right)^{n}\right] \\ -\Delta t\sum_{l}\left(\sum_{j=1}^{n_p} h_j^{l}\rho_j^{l}\Gamma_j^{l}\boldsymbol{\nabla}p^{l} + \Gamma_c^{l}\boldsymbol{\nabla}T^{l}\right) + \Delta t\sum_{j=1}^{n_p}\rho_j h_j q_j = 0 \end{aligned} \tag{5}$$

where:

- V is volume
- Δt is the time step
- l = connection l in the grid
- $\Gamma_j^l = \frac{\Gamma^l}{\mu j}$ where Γ^l is the harmonic average of permeability between two grids cells
- $\Gamma_c^l = \Gamma^l \kappa$
- n = time step
- $q_j = \tilde{q_j} V$

These discretized conservation equations represent systems of non-linear equations. The traditional way to solve these systems of equations is using the Newton-Raphson method. This method involves linearising the non-linear equations using Newton linearisation, constructing a Jacobian matrix at each non-linear iteration, solving the linear equations and then getting a residual. Once the residual is below a given tolerance the solution for the next time step is found. The Newton-Raphson method solves the linearised equations in the following form:

$$J(\omega^k)(\omega^{k+1} - \omega^k) + r(\omega^l) = 0 \tag{6}$$

where:

- J is a Jacobian matrix which is assembled in each iteration
- ω is the value you are trying to attain
- k is a non-linear iteration number

Unfortunately, if the system is complex, with numerous phases and components, this linearisation can become very complicated and lead to various sources of error (Khait and Voskov, 2018). DARTS uses a novel method for linearisation developed by Voskov (2017), known as operator-based linearisation. The method involves splitting the constitutive equations (equations 4 and 5) into operators and then processing one set of operators using multi-linear interpolation and the other set of operators using the standard Newton-Raphson method. A number of publications have proven this method to be a fast, robust and effective way of linearising the discretized mass and energy equations (Khait and Voskov, 2018; Voskov, 2017; Khait and Voskov, 2017). The process of operator-based linearisation is mathematically complex and beyond the scope of this report. For a full explanation, please refer to Voskov (2017).

3 Geological Modelling

In this section, a detailed account is given of the construction of the geological model of the Delft Sandstone using available seismic and well log data. More specifically, the section covers what data was available for model construction, the construction process itself, the logic behind any decisions made during this process and validation of the model through comparison with literature and well test results. Throughout this process, where feasibly possible, uncertainties have been acknowledged and quantified.

3.1 Data Available

The two main data sources used for the construction of the geological model were seismic data and well data. The seismic data consisted of a number of different 3D two-way travel time data sets of varying quality which have been combined into a single cube.. In terms of well data, data from 15 different wells both geothermal and oil/gas wells was used for model construction. Table 1 gives a complete summary of the data available for each well and what it was used for in the modelling process.

Well name	Well type	Inside model boundaries	Synthetic seismic well correlation	Horizon/ Layering Constraint	Logs	Used for Gamma-Porosity relation	Porosity log generated	Core
DEL-03	O/G			X	N/A			
DEL-08	O/G			X	N/A			
HAG-01	O/G	X		X	SP, RES		X	
HAG-02	O/G	X		X	GR, SP, RES		X	
HAG-GT-01	GT	X		X	GR		X	
HAG-GT-02	GT	X		X	GR		X	
KDZ-02-S1	O/G		X	X	GR, DT, RHO, NPHI, RES	X		
LIR-45	O/G				GR, DT, RHO, NPHI, RES	X		
MKP-11	O/G				N/A			X
PNA-13	O/G	X		X	N/A			
PNA-GT-01	GT	X		X	GR		X	
PNA-GT-02	GT	X		X	GR		X	
RTD-01	O/G				GR, DT, RHO, NPHI, RES	X		
RWK-01	O/G				N/A			
VDB-GT-04	GT				GR		X	

Table 1: Wells used in the study and the data available for them. N/A implies the well either does not have well logs or its well logs are unsuitable. Key: O/G = Oil/Gas, GT = Geothermal, GR = Gamma Ray, DT = Sonic, RHO = Density, NPHI = Neutron porosity, RES = Resistivity.

All of the well data and much of the seismic data used for this project is publicly available on NLOG.

3.2 Seismic Interpretation

The seismic interpretation process incorporates the defining of the three-dimensional shape of the reservoir in the subsurface via the tracing of key reflectors in two-way travel time (TWT) seismic sections and determining the position of the reservoir in terms of depth by time-to-depth conversion.

For this study, five reflectors were chosen for seismic interpretation due to the ubiquity of these unit boundaries in wells in the area and because these reflectors represent relatively strong impedance contrasts and thus are easily recognisable on seismic section. The five reflectors are listed below:

- Base North Sea
- Base Ommelandan
- Base Rijnland
- Base Rodenrijs

- Base Alblasserdam

Normally, to match the depth of the horizons as recorded in the wells to reflectors on the seismic section, synthetic seismic sections (sections created from well log sonic and density data) are used. However, as can be seen in Table 1, only a single well has the data available for seismic sections (KDZ-02-S1). Therefore, in this well a synthetic seismic match has been conducted whilst in other wells (HAG-GT wells) a manual match between patterns in gamma ray logs and the seismic section has been used. This manual matching was conducted by IF technology. The synthetic seismic for KDZ-02-S1 and the quality of match with section reflectors can be seen in Figure 78 in Appendix A.

Seismic interpretation was then carried out over the area of interest. The procedure for interpretation was as follows:

1. Fault interpretation along inlines.
2. Horizon interpretation between wells with markers in TWT (KDZ-02-S1 and HAG-GT-01).
3. Horizon interpretation on a grid of inlines and cross lines (inlines ~400m and crosslines ~800m).

A typical inline cross section across the graben system is shown in Figure 11. What is apparent from the section is that there are a number of complex structural features, including pop-up structures and faults which are both reverse and normal depending upon depth. This complexity is a result of the structural inversion of the WNB due to the Alpine Orogeny in the early Tertiary. Intersections of Y-type faults at the reservoir level cause difficulties for gridding algorithms and as such, the structure of some of the pop up structures have been simplified such that throw is preserved (Figure 12).

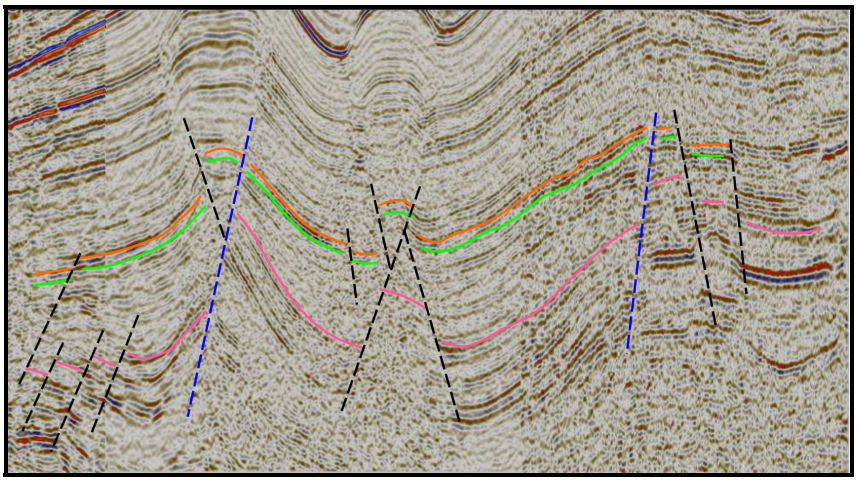

Figure 11: Seismic inline cross section though the Pijnacker and Den Haag Graben. Base Rijnland = orange, Base Rodenrijs = green, and the Base Alblasserdam = pink. Blue faults represent the major fault block bounding faults which act as boundaries for the model.

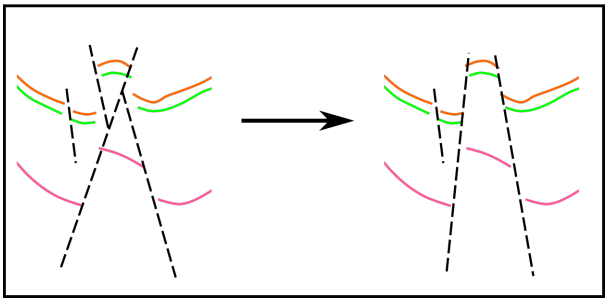

Figure 12: Simplification of the central pop-up structure.

Following determination of reservoir structure through seismic interpretation, the horizons in time required conversion to depth. This is done using a velocity model. For this , the following equation for

velocity is utilised:

$$V(z) = V_0 + Kz \tag{7}$$

Where $V(z)$ is the velocity of a given layer at a given depth z, V_0 is the velocity at the start of the layer and K is the velocity gradient.

V_0 for different geological units in the Dutch subsurface can be sourced as maps from NLOG. K is a set value for each unit, these values can be found in Table 14 in Appendix A (Van Dalfsen et al., 2006). Using the velocity model and two-way travel time, the true vertical depths (TVD) of the different reflectors were determined. To quality check the velocity modelling, the process was initially carried out without any correction of the generated surface to the depths of the horizons as recorded in the wells. Table 2 records the difference observed between the horizon surfaces at the wells and the actual position of the well top in the well. We can see from Table 2, that the difference in TVD is all under 50m, which is close to seismic resolution at that depth, and as such the accuracy of the velocity modelling is deemed acceptable.

Well	**TVD of Base Rijnland Well Top**	**TVD of Base Rijnland horizon converted via velocity model**	**Difference**	**T/Z relationships**
Well A	1642.86	1688.49	45.63	
Well B	2006.23	2013.64	7.41	
Well C	1711.06	1705.12	-5.94	X
Well D	2109.28	2111.42	2.14	X
Well E	1822.1	1861.66	39.56	X
Well F	1727.77	1712.32	-15.45	
		AVG	12.225	

Table 2: Difference in depth between time to depth converted seismic surfaces and their respective well tops.

Figure 13 shows a depth map of the Base Rodenrijs horizon/top of the reservoir created from the time to depth conversion process.

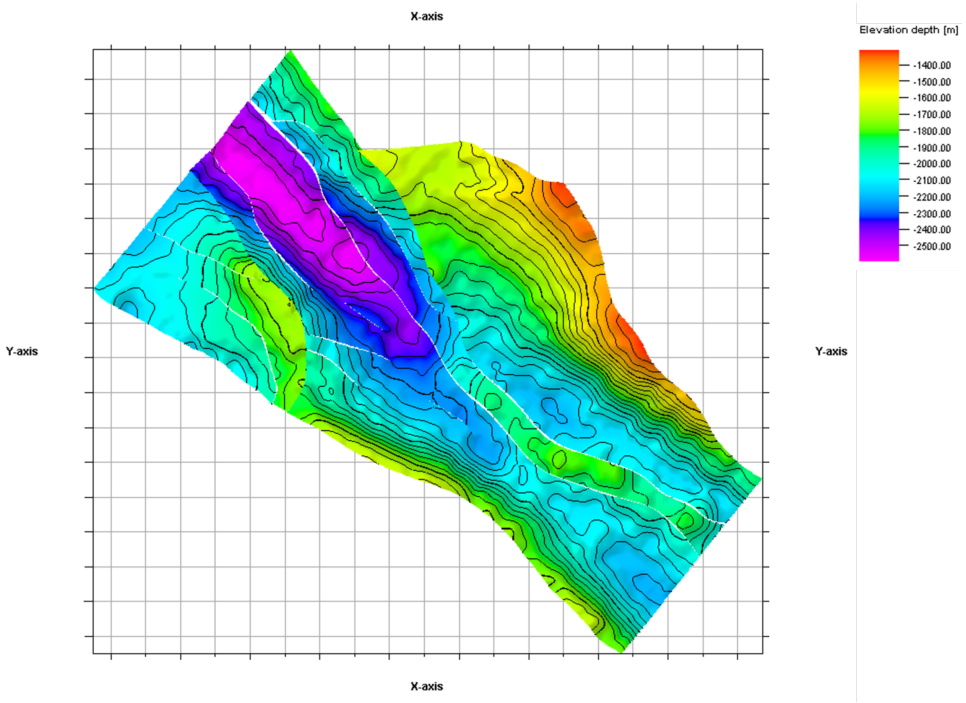

Figure 13: 2D depth map of the top of the reservoir based on the seismic interpretation of the Base Rodenrijs reflector.

3.3 Petrophysics

Petrophysical properties measured and derived from well logs form the basis for populating the static geological model. The primary purpose of the petrophyscial analysis is the accurate determination of porosity and permeability.

3.3.1 Porosity

The standard method for porosity derivation utilised by the oil and gas industry is through the use of the combined neutron porosity (NPHI) and density logs (RHOB). However, a look at Table 1 shows that none of the wells within the model boundaries have had NPHI or RHOB logs run. Therefore, a different approach was required to calculate porosity. As gamma ray (GR) is the only well log available in many of the wells, the solution was to determine a relationship between GR and porosity in oil/gas wells which could be used to derive porosity in the geothermal wells. To derive this relation, data was used from three oil wells which had suitably large amounts of data and were in close enough proximity to the model area (Table 1). For the three wells used, the range of recorded GR values was highly variable probably due to differences in the logging tool and its calibration. Therefore, the GR data for the wells was normalised to a volume of shale fraction given by the equation below:

$$V_{shale} = \frac{GR_{log} - GR_{sand}}{GR_{shale} - GR_{sand}} \tag{8}$$

Where V_{shale} is the volume of shale, GR_{log} is the GR log reading at a given depth, GR_{sand} is the GR value of clean sand and GR_{shale} is the GR value of pure shale (Crain, 2002).

It was originally intended to plot volume of shale against total porosity calculated from both density and neutron porosity. However, neutron porosity is strongly affected by the presence of clay (clay has a lot of bound water which gets picked up by the logging tool). The standard way to correct for this is by using a V_{shale} correction. However, this would result in the plotting of a parameter containing V_{shale} against V_{shale} which automatically results in correlation. As such, only the density was used to calculate total porosity using the equation below:

$$\phi = \frac{\rho_{matrix} - \rho_{bulk}}{\rho_{matrix} - \rho_{fluid}} \tag{9}$$

Where ϕ is the total porosity, ρ_{matrix} is the density of the rock matrix, ρ_{bulk} is the density of the matrix and fluid combined and ρ_{fluid} is the density of the pore fluid (Crain, 2002).

Equation 9 requires the density of the matrix and density of the fluid to be known. The density of the fluid can be fairly well constrained as fluid samples of brine in the reservoir have been measured for salinity and temperature. These values can then be used to calculate density (1064.8 Kg/m^3). It should be added that the possibility of oil and gas being present (lower density fluids) was accounted for by removing any areas of high resistivity (indicative of oil and gas) from the porosity calculations. The matrix density is a far more difficult value to estimate because no lithology logs of the wells exist and even if they did, the matrix density of shale (of which a large portion of the reservoir is composed) is notoriously variable. To avoid negative porosity values, a matrix value for sandstone is used. As the porosity of sandstone, and not shale, is the key variable to be found, this is an appropriate simplification.

Figure 14 shows the relationship between total porosity and the volume of shale for the Delft Sandstone in three oil and gas wells. A negative correlation can clearly be observed in all three of the wells. By combining the data from the three wells and applying a geometric mean regression, a relationship was derived which links the volume of shale (and thus gamma ray) to total porosity (Figure 15). The relationship is given in equation 10.

$$V_{shale} = -1.8544\phi + 0.4876 \tag{10}$$

The porosity value calculated from equation 10 is total porosity, which accounts for ineffective clay matrix porosity which does not contribute to flow. Therefore, the value was converted to effective porosity (ϕ_{eff}) using the following commonly used equation (Crain, 2002):

$$\phi_{eff} = \phi - V_{clay} * 0.1 \tag{11}$$

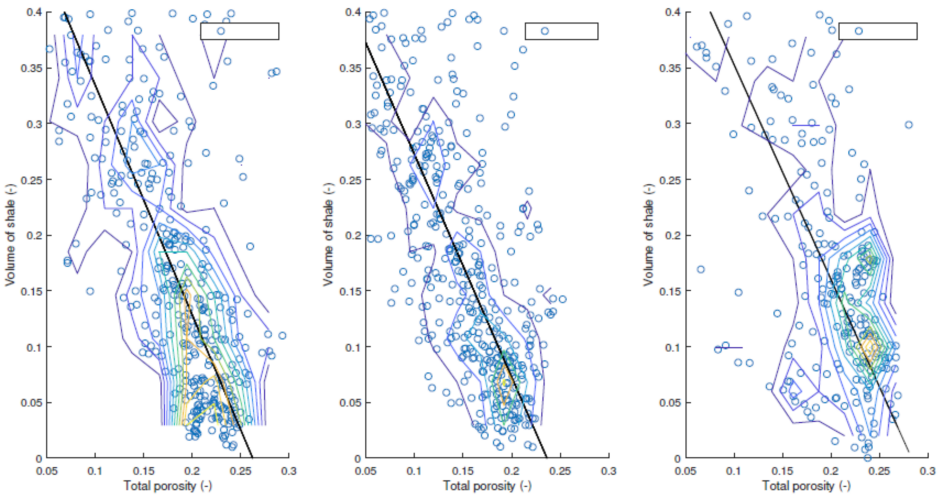

Figure 14: Total Porosity vs Volume of Shale for three wells.

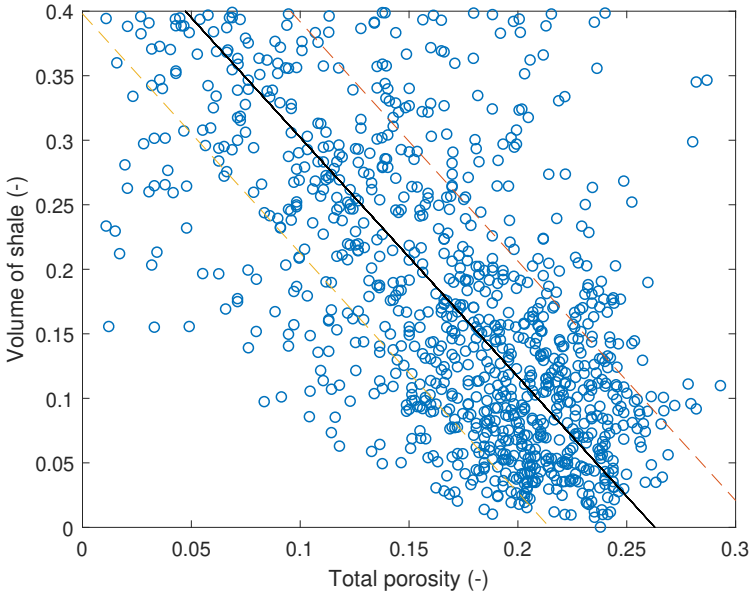

Figure 15: Total porosity vs Volume of shale for all three wells combined.

At this point, it is important to note that the data from the three wells all lie in a fairly similar depth range (between 1850 and 2250 meters depth, with an average depth of 2020 meters). From Figure 13, we can see that the reservoir lies over a very large depth range. This variation in depth will result in variable amounts of compaction and so this should be accounted for when calculating porosity. To do this, a porosity correction has been performed. This correction was applied after the property modelling and therefore is discussed in section 3.7.

3.3.2 Permeability

The derivation of permeability from porosity requires a porosity-permeability (poro-perm) relationship. For this project, two data sets were available for the derivation of a porosity-permeability relationship: core data and well test data. Core data has the advantage that it is plentiful but it is not on the correct scale for reservoir simulation, whilst well tests are on a more appropriate scale but there are far fewer measurements. To weight the well tests more strongly against the core data, the core porosity and permeability data was sorted into 1% porosity bins and then averaged both arithmetically

and geometrically. The different averages and the well tests were then fitted with polynomial trend lines depicted by the black and blue lines in Figure 16. From Figure 16, we can see that the line fitted to the arithmetic mean of the core data and the well tests gives the best fit and thus the equation of this line (equation 12) constitutes the primary porosity-permeability relationship used for the study.

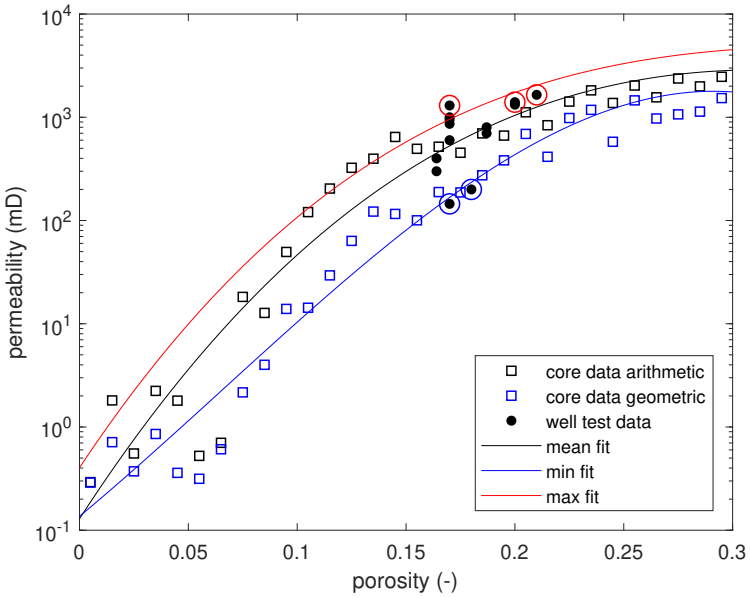

Figure 16: Porosity - permeability relationship.

$$K_h = e^{110.7440\phi_{eff}^3 - 171.8268\phi_{eff}^2 + 74.9227\phi_{eff} - 2.0470} \tag{12}$$

Where K_h is the horizontal permeability.

As permeability is logarithmic in nature, the porosity-permeability relationship is key to understanding uncertainty, therefore maximum and minimum poro-perm relationships have also been derived. As the well tests give the best indication of reservoir scale permeability, the maximum and minimum relationships should fit with the maximum and minimum values of well test permeability. Coincidentally, the polynomial trend line through the geometrically averaged core data fits very well with the lowest most well test values (denoted by blue circles in Figure 16) and therefore was taken as the minimum poro-perm relationship. For the maximum poro-perm relationship, a line was fitted to the three well test data points circled in red in Figure 16 and a few points just acting to restrain the curve at very high and low porosity values. This method, although quite rough, gives a geologically plausible range of permeability uncertainty from the porosity-permeability relationship.

Permeability in the vertical direction is nearly always lower than in the horizontal direction, primarily due to the nature of geological layering. It is therefore important to attempt to estimate the difference in vertical and horizontal permeability through a K_v/K_h ratio. To do this a very simple method was used. In general, a reasonable approximation of the average permeability when flow is across multiple rock layers (as is the case for vertical flow) is given by the harmonic average of the individual layer permeabilities (equation 13), whilst a reasonable approximation of the average permeability when flow is along rock layers (horizontal flow) is given by the arithmetic average of the individual permeabilities (equation 14) (Qi and Hesketh, 2005). With this in mind, four wells had sections of uninterrupted net reservoir (sections with porosity constantly higher than 0.05) identified and extracted. The permeability values for these sections of reservoir were then averaged harmonically and arithmetically, thereby giving a rough idea of the difference in vertical and horizontal permeability. The results of this analysis are displayed in Table 3.

$$\overline{K} = \frac{n}{\sum_{i=1}^{n} \frac{1}{K_i}} \tag{13}$$

$$\overline{K} = \frac{\sum_{i=1}^{n} K_i}{n} \tag{14}$$

Well	Reservoir Unit	Average Kh (mD)	Average Kv (mD)	Kh/Kv	Kv/Kh
Well A	1	1330.6	95.1	13.99159	0.071472
Well A	2	1231.2	34.9	35.27794	0.028346
Well B	1	1520.5	508.9	2.987817	0.334693
Well B	2	1292.3	402.4	3.211481	0.311383
Well B	3	1390.1	882	1.576077	0.634487
Well B	4	1576.2	356.7	4.418839	0.226304
Well C	1	976.4	51.3	19.03314	0.05254
Well C	2	754.9	56.6	13.33746	0.074977
Well C	3	623.5	196.6	3.171414	0.315317
Well D	1	1105.8	276.3	4.002172	0.249864
Well D	2	1559.6	187.2	8.331197	0.120031
Well D	3	1213	865.2	1.401988	0.713273
Well D	4	1017.6	486.7	2.090816	0.478282
			Max	1.401988	0.713273
			Min	35.27794	0.028346
			Average	8.679378	0.115216

Table 3: K_v/K_h from well analysis.

3.3.3 Properties of the Formation Water

To calculate temperature, a linear temperature-depth relationship was used, this relationship was provided by IF-technology and was based off bottom hole data from wells in the area. Similarly, data for total dissolved solids (TDS) and temperature were used to calculate density of the reservoir brine (Fofonoff and Millard Jr, 1983).

Pressure in the reservoir is assumed to be hydrostatic and therefore the pressure in the reservoir is simply given by equation 15. The assumption of the pressure being hydrostatic is based on the lack of data to determine otherwise.

$$P = \rho g z \tag{15}$$

Where P is pressure, ρ is the density of brine and g is the gravitational constant.

3.4 Conceptual Geological Model

For construction of a static geological model, a blueprint/idea of the reservoir structure and geology is required. This generally takes the form of a conceptual geological model, which is derived from a number of pieces of evidence including: seismic, well logs and literature on the formation in question. A summary outlining the most important features of the Delft Sandstone to be included in the conceptual model is given below:

- The Delft Sandstone consists of fluvial sandstones and flood plain deposits deposited in an active syn-rift environment, with the fluvial system flowing in what is now an SE-NW direction.
- The rate of deposition was most likely primarily controlled by subsidence rate, with evidence given by the fact that the Alblasserdam can be seen to thicken towards normal faults.
- The prime reservoir lithology consists of fining upwards point bar deposits which were deposited on the inner bends of meander loops.
- The point bar sands occur as both stacked and isolated deposits. This was most likely controlled by the balance of accommodation space vs sedimentation rate, with periods of low accommodation space generation allowing reworking of the floodplain and slow sediment accumulation, which in turn allows for stacking of point bar deposits and removal of flood plain fines.
- Evidence from palynology shows that the Delft Sandstone was not deposited all at once, instead the main fluvial system moved from the Den Haag Graben towards the west over time. This has resulted in the sand occurring at different stratigraphic levels within the individual grabens.

This information has been combined and is depicted in the conceptual geological model shown in Figure 3.4.

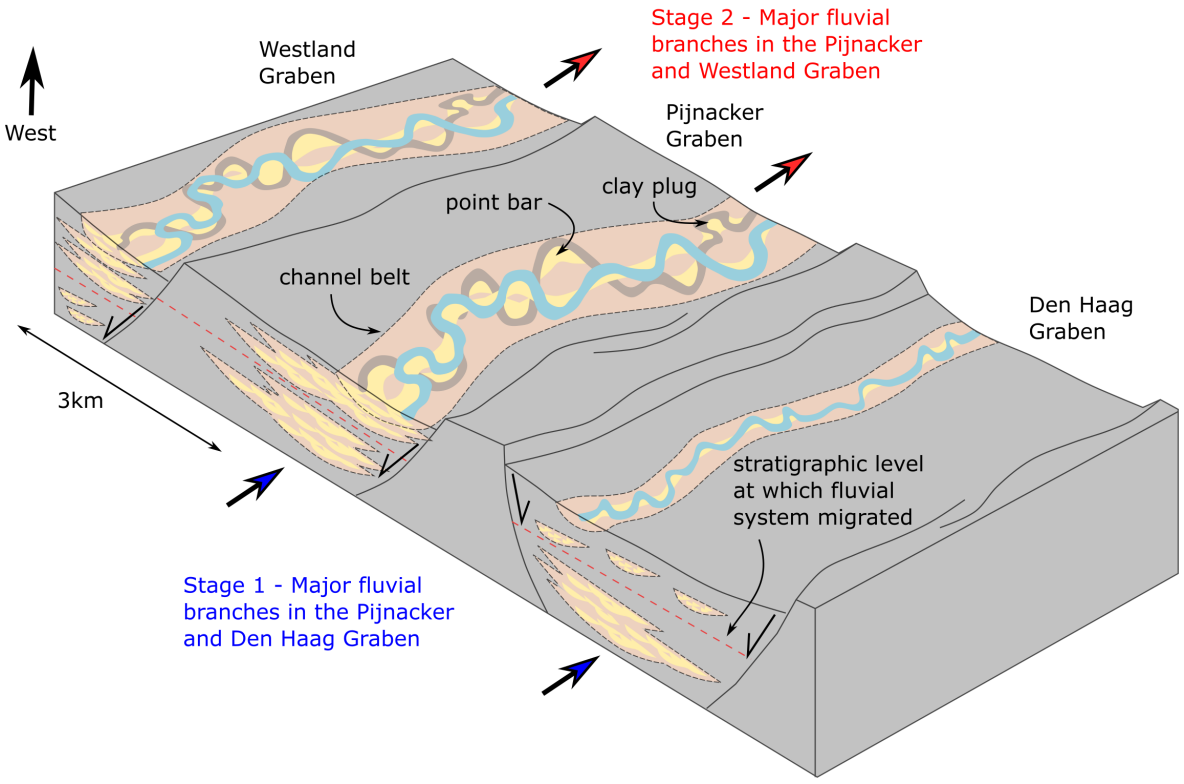

Figure 17: Conceptual geological model of the Delft Sandstone. The model depicts the structural environment of deposition, the depositional architecture and how deposition has changed over time.

3.5 Reservoir Structure

As outlined in the conceptual geological model and as shown in a cross section through five of the wells (Figure 19), the distribution of high N/G reservoir is very variable both vertically and horizontally. We can see from Figure 19, that in the northeast, poor quality reservoir overlies high quality reservoir and that in the southwest, high quality reservoir overlies poorer quality reservoir. To account for this distribution, a two layer reservoir system was utilised whereby the reservoir was divided up into a top sandstone and a bottom sandstone layer. The boundaries of these sandstone layers (which can be seen in Figure 19) are picked such that they coincide with large vertical changes in reservoir quality. The way the two layer concept works across the graben systems is depicted in Figure 18.

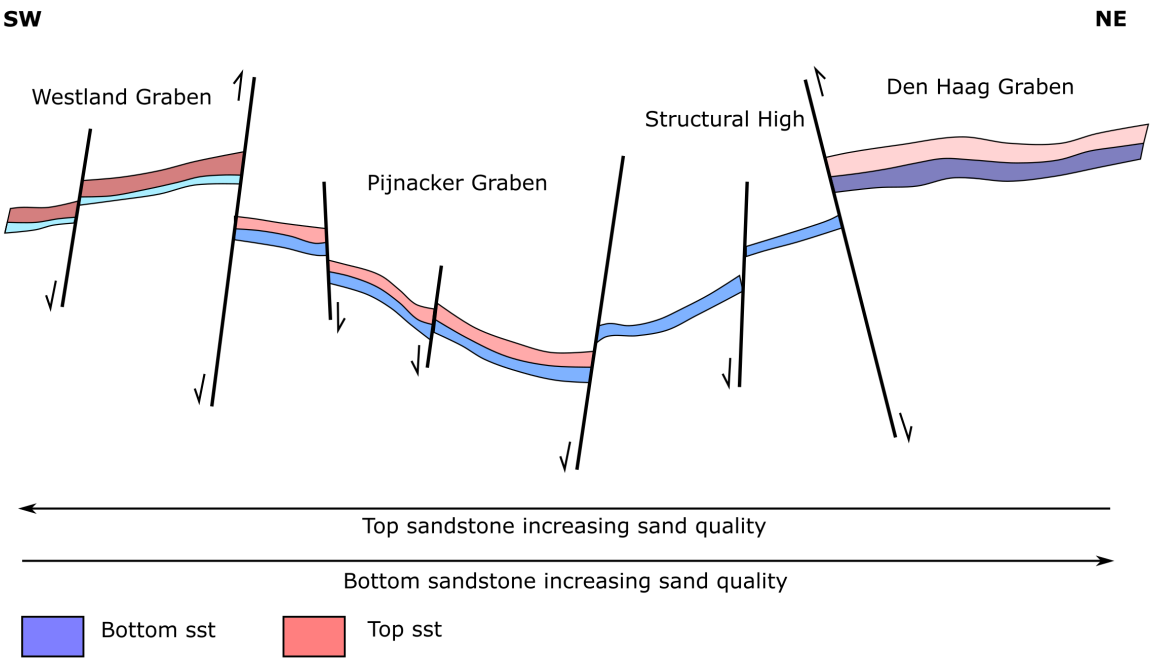

Figure 18: 2D inline section across the graben showing reservoir compartmentalisation. Darker colours represent higher quality reservoir.

The two layer system allows for the large vertical changes in reservoir quality observed in the well logs to be accounted for. It also allows for lateral changes in reservoir quality to be accounted for, as the property modelling process was applied to the top and bottom sandstone separately in each graben system.

Figure 19: West to East well section flattened on the top reservoir horizon showing 5 wells. Shown in the figure is the facies log, effective porosity log, unit log and the position of the layer boundaries.

3.6 Facies Modelling

The aim of the facies modelling process is to create a reasonable approximation of the geology of a reservoir in a three-dimensional cartesian grid. The first step in this process was defining the number of facies which are represented in the model. Fluvial systems are notoriously complex in terms of their facies composition, with typical fluvial systems containing point bars, crevasse splays, braided channels, clay plugs, coal, flood plain clays/shales etc. In this study, the fluvial system has been simplified into only two constituent facies: meander belt facies and flood plain facies. The reasons for this are two fold: Firstly identifying all the facies types correctly using only a gamma ray log is not trivial, whereas splitting it down into the two categories makes this subdivision of well logs much simpler. Secondly, fluvial facies in reality can change over very short distances (10's to a few 100's of metres). With the fact that the reservoir that is being modelled is ~15km long and ~7km wide, the number of cells needed to capture the spatial variation in the fluvial facies would result in prohibitively long simulation times. In contrast, meander belts tend to be larger in scale (km's) and as such can be modelled on a coarser grid with reasonable simulation times. An average grid cell size of 80x80m is used for the model. This size represents a compromise between capturing details of geological variation whilst also keeping the model a manageable size (~two million grid cells).

The meander belts were effectively modelled as large channels using Petrel's object based modelling capabilities (a method whereby discrete objects can be defined in the grid such as channels, meander belts, lobes etc). To conduct this object based modelling, both the proportion of the facies and the dimensions of the objects in question were required. Proportions of the facies in each layer could be determined from a facies logs, a simple log which divides the wells up into the two facies types (Figure 19). To determine the facies proportion in a layer within a certain graben, an average of the facies proportions from all the wells within that graben was used. To determine the dimensions of the channel belts, data was analysed from three studies (Delft Sandstone (Loerakker, 2009), Delft Sandstone (Jeremiah et al., 2010) and the Huesca alluvial fan (Donselaar and Schmidt, 2005)). In particular, data on the vertical thickness of point bar deposits was collected and is displayed in Table 15 in Appendix A. There are numerous pieces of literature published which have tried to link the thickness of point bar deposits to the width of meander belts. Figure 20 shows three different relationships from three different studies: Lorenz et al. (1985), Fielding and Crane (1987) and Collinson (1977). For the base case of this study the relationship from Lorenz et al. (1985) is used (Equation 16) simply because it gives middle range values for meander belt widths. The uncertainty associated with these relationships is analysed and discussed in section 4.4.2.

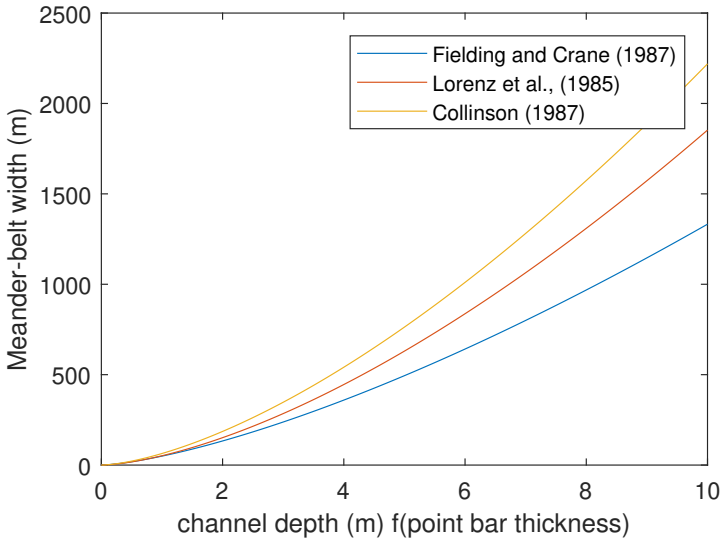

Figure 20: Three different relationships between channel depth (a function of point bar thickness) and meander belt width.

$$W = 7.44 * (6.8 * D^{1.54})^{1.01} \tag{16}$$

Where W is the meander belt width and D is the channel depth.

Using the point bar thickness data and the Lorenz relationship a range of meander belt widths were derived. These are shown in Figure 21 and are also recorded in Table 15 in Appendix A. Using the minimum, maximum and mean of these values to create a triangular distribution, the model could be populated with meander belts (Figure 22). Orientation of the meander belts can be well constrained because the fluvial deposits are syn-rift and thus align with the graben fault system (~315°).

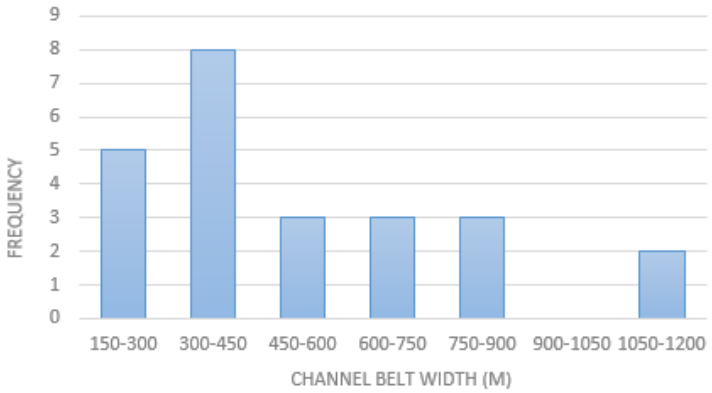

Figure 21: Frequency of different meander belt widths based on the thickness of fluvial point bar deposits.

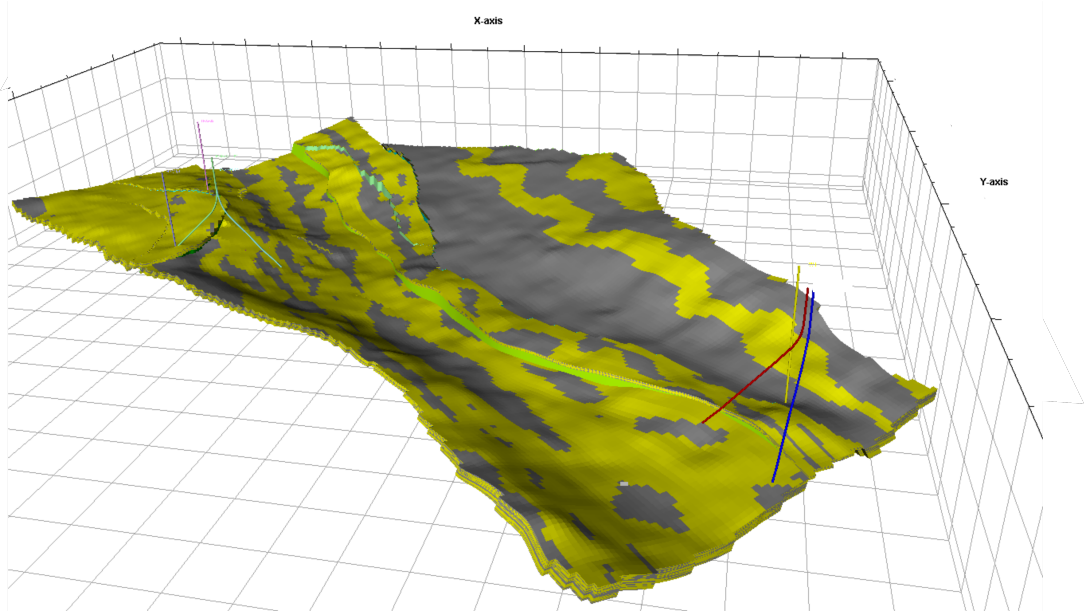

Figure 22: 3D facies model viewed from the south. Meander belts are shown in yellow whilst flood plain clays are in grey.

3.7 Porosity Modelling

The final stage in the geological modelling process is the extrapolation of porosity from the well logs through the rest of the grid. As porosity is key to determining permeability and thus flow, it is essential to have a geologically plausible porosity distribution.

The standard practice for distributing porosity across the grid is simply to upscale the porosity logs arithmetically so that there is one porosity value per cell and then use the upscaled porosity distribution

to control the distribution of porosity which is applied to the grid. However, Figure 23 shows that the upscaled porosity values of the well logs (green) are not a particularly good match with the non-upscaled porosity distribution. Therefore, a Beta distribution (purple) was fitted to the well log data instead. This shows a better match with the non-upscaled data (especially in terms of modal porosity).

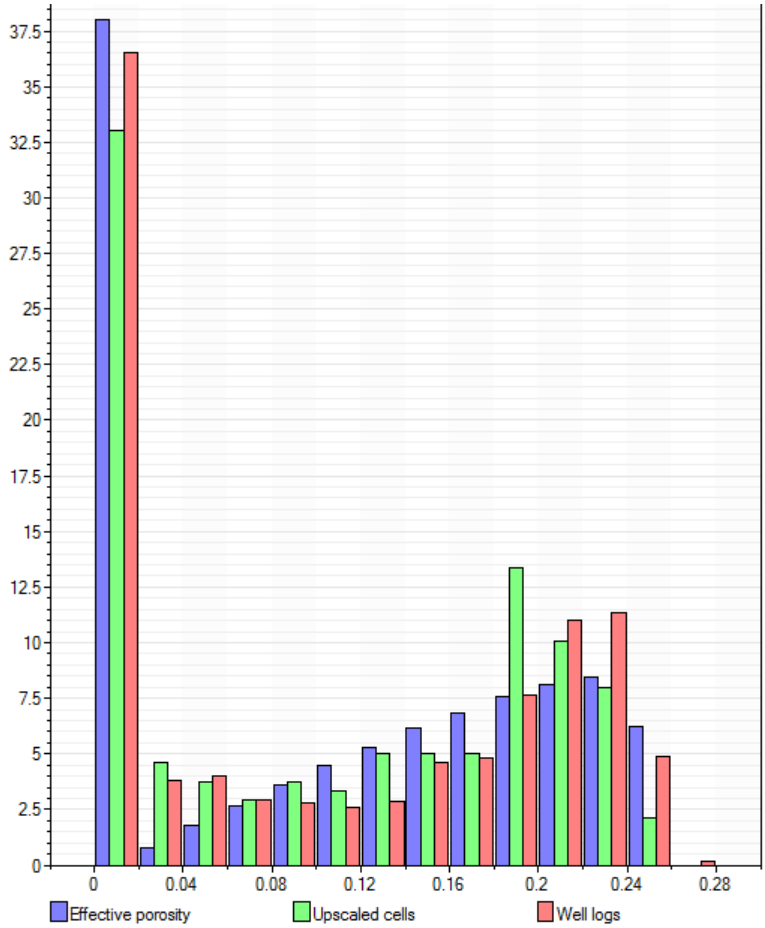

Figure 23: Model porosity distributions: well log porosity (red), upscaled well log porosity (green) and beta/grid porosity (blue).

In terms of porosity modelling for the flood plain facies and the meander belt facies, considerably different approaches were taken. For the flood plain facies, a constant value of 0.01 for porosity and 0.01mD for permeability were applied across the grid to ensure that this facies did not contribute to flow. This has the benefit of making the model simpler and the results easier to interpret, however it also has the disadvantage that it is an oversimplification. It would be very difficult however, to model the floodplain facies in such a way so as to accurately represent any existing porosity and permeability distribution. For modelling of the meander belts, the beta distribution is used in combination with Sequential Gaussian Simulation (SGS) to populate the model. Due to the complexity of the method, SGS shall not be explained in detail, however, what it effectively does is it relates porosity values over a given range whilst matching the porosity field to a given porosity distribution in a stochastic manner. The relation range chosen for SGS was 700m along the channel axes and 300m across. These values give a distribution which is supposed to represent point bars in the meander belt system. A comparison between a meander belt from the grid and a conceptual meander belt is shown in Figure 24, the resulting match is reasonable given the constraints. The porosity distribution for the whole model is shown in Figure 25.

As discussed in the section 3.3.3, porosity values require correction to account for the effects of compaction. This is done with the aid of a porosity-depth relationship provided by IF-technology.

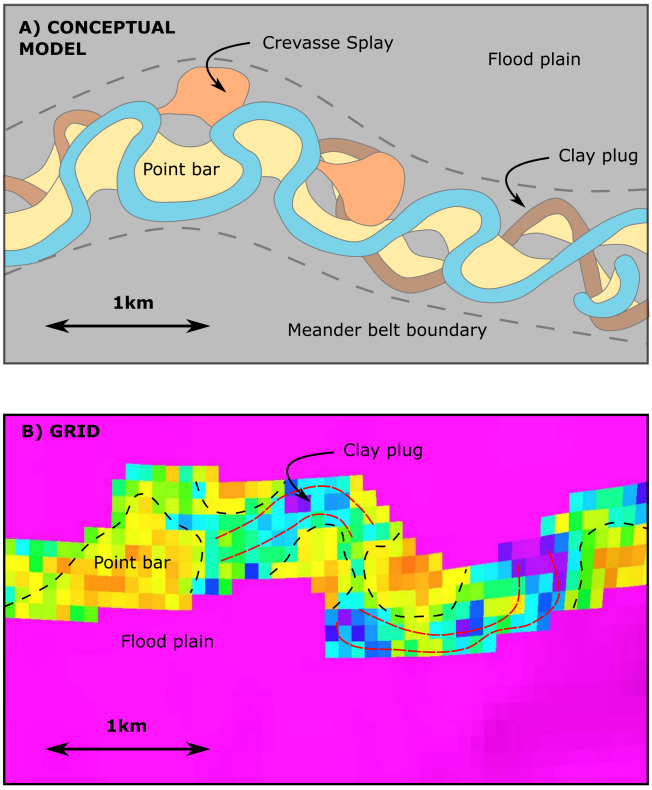

Figure 24: Comparison between an ideal conceptual meander belt system (top) and the distribution of porosity in the grid (bottom). Orange and yellow represent areas of high porosity whilst purples and blue represent lower porosity.

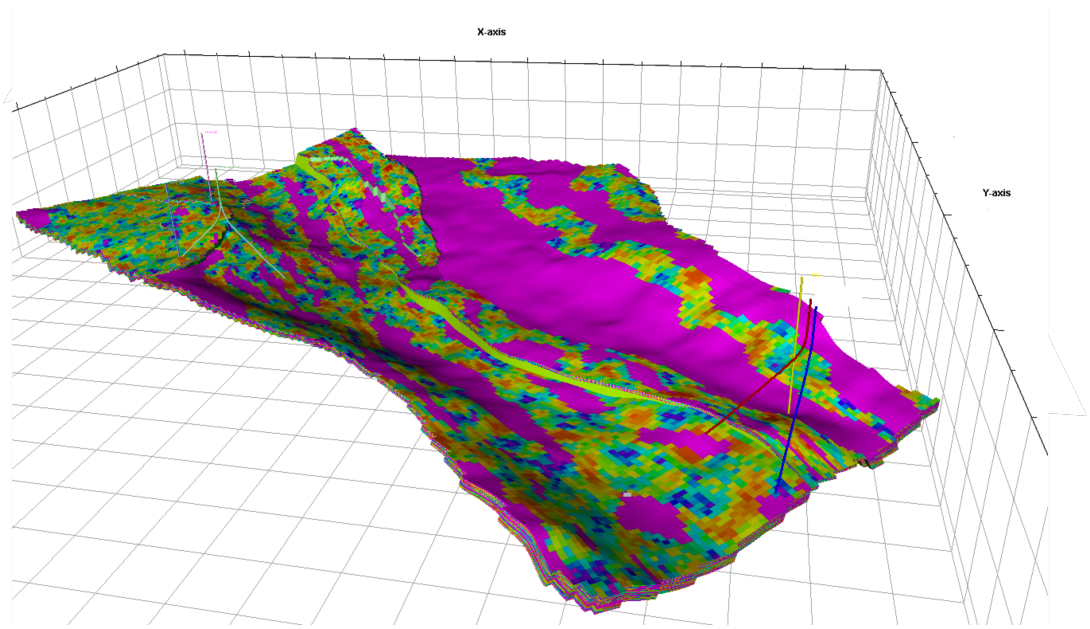

Figure 25: 3D porosity model viewed from the south. The red represents 25% porosity whilst the pink is 1% porosity.

The average depth of the data used to form the porosity-Vshale relationship (equation 10) was 2020m. Based on this depth value, a reference value of porosity was calculated using an IF Technology porosity-depth relationship. In a similar process, a hypothetical porosity value was generated for each cell in the entire grid based on each cells TVD. By dividing the cell's hypothetical porosity value with

the reference value, a multiplier is produced which is either positive or negative depending on whether the cell in question is above or below the reference depth. This multiplier for each grid cell could then be used on the effective porosity value for that grid cell to correct the value for its depth.

With the porosity model complete, other properties such as permeability, temperature, pressure could be calculated for each grid cell using relationships derived in section 3.3.3.

3.8 Model Validation

To confirm that the model is plausible in terms of its properties, comparisons are made with both reported values from literature and from well test results. Table 4 shows some of the average properties taken from the model.

Parameter (average value)	Value
Porosity (-)	0.12
Horizontal permeability (mD)	569.7
Vertical permeability (mD)	65.5
N/G	0.68
Porosity of net reservoir (-)	0.18
Horizontal permeability of net reservoir - from average porosity (mD)	677.32
Vertical permeability of net reservoir (mD)	68.92
Temperature (^{o}C)	74.64
Pressure (bar)	216.41

Table 4: Average reservoir properties from the geological model.

These derived properties match relatively well with the values reported by Donselaar et al. (2015) (section 2.1).

Comparisons were also made between average permeability values derived from the well log data and well test data for wells in the Delft Sandstone. For the comparison, data from Hydreco has been used in addition to data produced from Horner plot analyses carried out as part of this study. A description of the Horner plot analysis is given in Appendix A. The results of the comparison are shown in Figure 26.

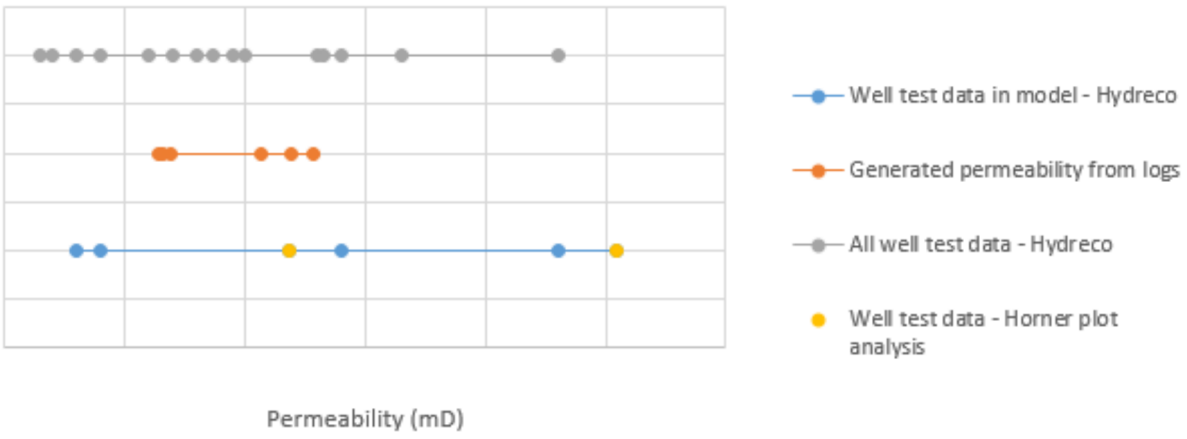

Figure 26: Average reservoir permeability from well testing and from generated logs (x scale is removed for confidentiality reasons).

From the comparison, it is clear that the permeability values generated by the petrophysical methods described in section 3.3.3 lie well within the recorded range of permeability recorded for the Delft Sandstone and this would still be the case even if the upper end anomalous results were to be removed from the analysis.

4 Sensitivity and Uncertainty Analysis

As mentioned in the introduction (section 1.1), understanding the uncertainties of the model and how sensitive the model is to its input parameters is vital for good reservoir simulation. The aim of this section is to conduct a thorough sensitivity and uncertainty analysis on the geological model created in section 3 to get an idea of which factors are most import in controlling thermal front propagation within the Delft Sandstone.

4.1 Models

This subsection outlines which models have been used for the simulation experiments, what boundary and initial conditions have been used and why these conditions have been chosen.

4.1.1 Grids

Two different grids have been used for simulation experiments conducted in the sensitivity and uncertainty analysis and the well placement study. These are given below:

- **Full model** - All two million grid cells from all three of the grabens.
- **Small model** - A sub-section from the southeast of the Pijnacker Graben which consists of approximately 100,000 grid cells.

The full grid model is used for simulations involving the interaction of multiple well pairs and is therefore utilised primarily in the well placement section (Section 5). For the running of multiple simulations, as has been executed in the sensitivity and uncertainty analysis, the full grid simulation takes too long to run (~30 minutes). Therefore, the smaller grid is used to save on computational time. Figure 27 shows the two grids.

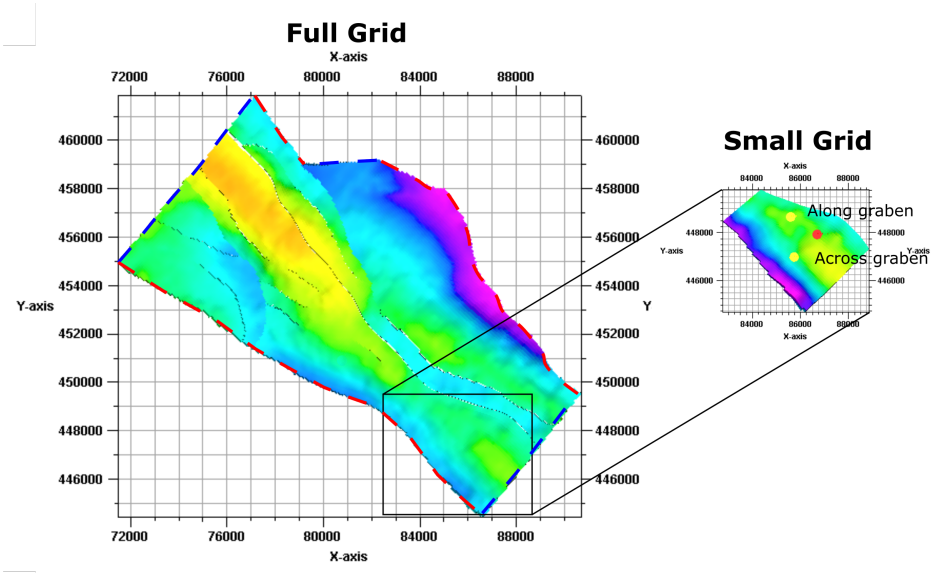

Figure 27: Pressure maps showing the extent of the large grid and the small grid. Blue dashed lines indicate boundaries open to flow. Red dashed lines indicate boundaries closed to flow.

4.1.2 Boundary Conditions

In terms of boundary conditions, two factors need to be addressed. How the cells on the boundary of the model behave and how the well cells behave. For the cells on the model boundary, it was assumed that at either ends of the graben system there are very large volumes of reservoir from which water would be able to flow. This is a reasonable assumption as works by Duin et al. (2006) show that the graben systems extend a long way offshore and inland. To mimic extension of the reservoir, cells on these boundaries have been assigned very large volumes. These boundaries are referred to as open

boundaries. Along the boundaries to the northeast and southwest are large displacement faults, these are assumed to be sealing and so the boundary is left closed.

The wells in the simulation were controlled one of two ways: bottom-hole pressure (BHP) or flow rate. For control with BHP, injection and production wells are set to 20 bar above and below average initial reservoir pressure respectively. As wells are not in reality controlled by BHP, the values chosen are not of paramount importance as long as they allow direct comparison between wells. 20 bar drawdown/injection pressure resulted in thermal breakthrough at reasonable times and for this reason this value was chosen. In reality, wells are controlled by rate. When simulating rate controlled wells, care needs to be taken to stop the wells surpassing realistic BHP conditions (e.g. 100's of bar above/below initial reservoir pressure). To stop this, BHP constraints were applied to rate-controlled wells. For injection, the constraint was 5 bar below the fracture pressure at the top of the reservoir. The fracture gradient was set as 0.15bar/m. For production wells, the drawdown limit was set at 50 bar below average initial reservoir pressure, this value is based on the maximum drawdown achievable by down-hole geothermal pumps. The target rate was set at $8640\text{m}^3/\text{day}$, this represents a well running at $450\text{m}^3/\text{day}$ for 80% of the time (wells will not be working for part of the year for work-overs and maintenance). Wells are all vertical and perforated through the entire reservoir interval. A table summarising the above conditions is shown below.

Well Type	Pressure Control	Rate Control
Injector	20 bar above inital reservoir pressure	$8640\text{m}^3/\text{day}$ BHP constraint: 5 bar below fracture pressure at the top of the reservoir
Producer	20 bar below inital reservoir pressure	$8640\text{m}^3/\text{day}$ BHP constraint: 50 bar below average initial reservoir pressure at the bottom of the well

Table 5: Well control summary

4.1.3 Initial Conditions

Three variants of initial temperature and pressure conditions have been used dependant on the desired complexity of the simulation, these are:

- **Constant temperature and constant pressure** - used in sensitivity and box model experiments where the aim is to see the magnitude in difference between simulations, not to model reality.
- **Constant temperature and variable pressure** - a constant initial temperature (or more accurately enthalpy) results in a much clearer thermal breakthrough in producer wells when compared to variable initial temperature. The clear thermal breakthrough has the advantage that it allows much better comparison between wells in different locations. Pressure is set as variable to try to model reality. These initial conditions are only used in the well placement section (Section 5).
- **Variable temperature and variable pressure** - used when aiming to find the true performance of a well in terms of both breakthrough time and total thermal energy available. Variable temperature profiles can make comparisons between wells more difficult.

In terms of thermal properties of the reservoir, all cells were given a uniform thermal conduction and heat capacity value. In reality this is a simplification. However, investigation of other factors was given priority following the sensitivity analysis. The values used are typical of siliciclastic rock types:

- **Thermal conduction** - $2.3\text{W}/\text{m}^{-1}\text{K}^{-1}$
- **Heat capacity** - $2.2\text{MJ}/\text{m}^3\text{K}^{-1}$

4.1.4 Definition of Thermal Breakthrough

For comparisons of results between simulation experiments, a set temperature drop which represents clear thermal breakthrough is required. For the well placement study and the sensitivity and

uncertainty analysis, a temperature drop of 2^{o}C is used, simply because this is a value which is small enough that it is reached by the vast majority of simulations but is large enough that it is only reached when temperature decline due to thermal breakthrough has happened (i.e. it is not surpassed by small initial temperature drops that occur in some simulations).

4.2 Sensitivity Analysis

4.2.1 Method

Sensitivity analysis involves the systematic changing of input parameters to determine which parameters have the largest effect on the results of simulations. For this study, five important input parameters were chosen for sensitivity analysis. These are:

- Permeability (constant porosity)
- Porosity (and through the poro-perm relationship, permeability)
- Kv:Kh
- Thermal Conductivity
- Initial Temperature

The method for conducting the sensitivity analysis is very simple. The model created in Section 3, referred to as the base case, forms the benchmark from which the sensitivity analysis was conducted. For each sensitivity experiment, the parameter in question was changed by $\pm$10% from the benchmark value. Simulations were then run and the difference in the solutions recorded.

The experiments were run on the small grid so as to save on computational time and were run with pressure control. As it is the difference in the solutions that is important for sensitivity analysis and not the actual value of the solutions themselves, using pressure control was deemed acceptable. For the same reason, it was also acceptable to use constant initial temperature and pressure. The run time for the simulations is 50 years. The doublet configuration was set so that the doublet was aligned across the graben axis with the injector and producer well spaced 1300m apart.

4.2.2 Results and Discussion

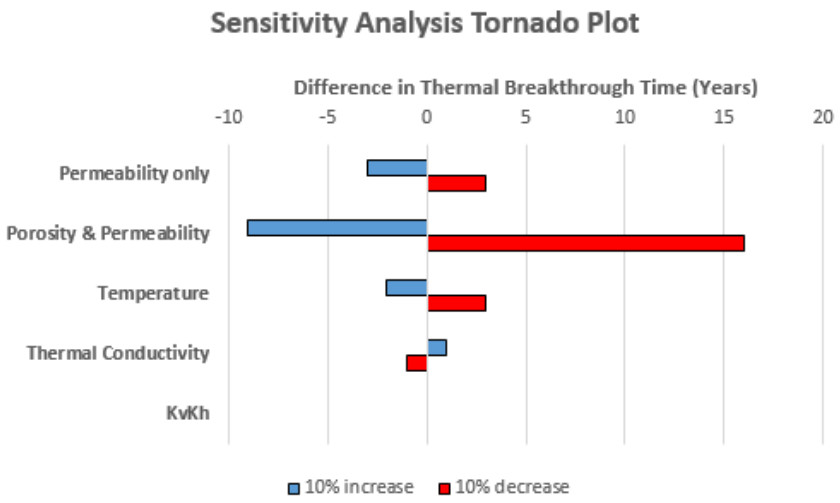

Figure 28: Sensitivity of thermal breakthrough times (relative to base case) to various input parameters.

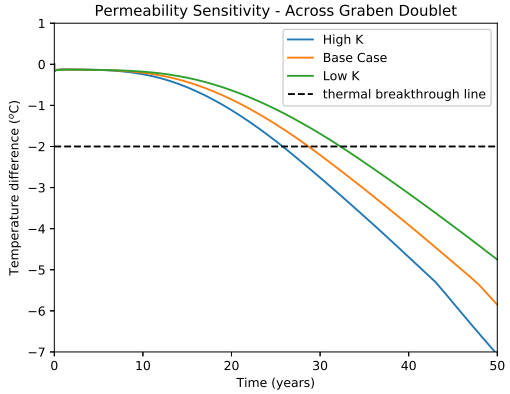

(a) Permeability only

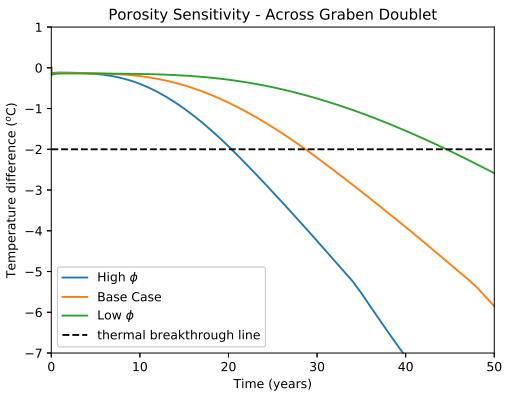

(b) Porosity (and permeability)

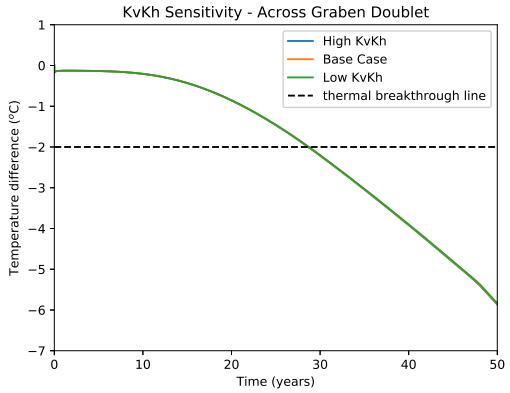

(c) Kv:Kh

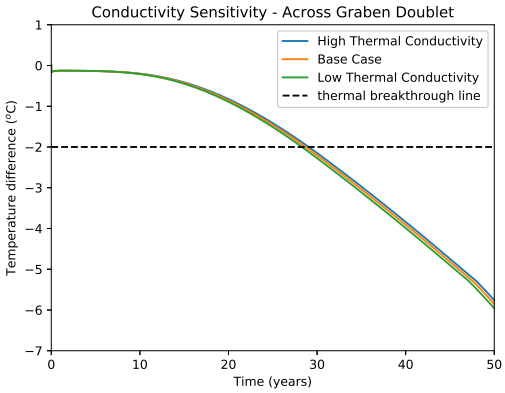

(d) Thermal conductivity

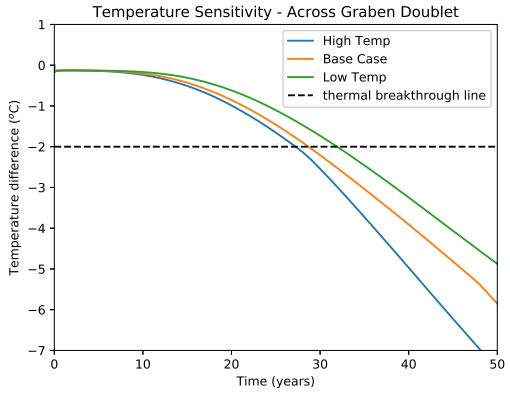

(e) Initial temperature

Figure 29: Temperature change at the producer well vs time for sensitivity analysis

Figure 29 shows the results of the sensitivity analysis in terms of thermal breakthrough vs time, whilst Figure 28 is a tornado plot which summarises the information shown in the graphs. Immediately evident from Figure 28, is the importance of porosity & permeability in controlling thermal breakthrough time. This result reflects the importance of the porosity-permeability relationship. Because of the logarithmic nature of permeability, small changes in porosity lead to very large changes in permeability, which in turn greatly effects the flow rate achievable for a given pressure. This conclusion is consolidated by the fact that the second most important factor is a 10 percent change in permeability alone.

The result for initial temperature appears counter-intuitive at first. However, it should be noted that the experiment is measuring change in temperature relative to initial reservoir temperature and with the higher initial temperature comes stronger thermal gradients, which in turn leads to more rapid cooling rates. Finally, Figure 28 shows us that the rate of thermal conductivity and the Kv:Kh are much less important in influencing thermal breakthrough. The result for thermal conductivity is not that surprising, as the rate at which heat conducts through rock is minimal compared to the rate at which heat advects as part of a water body. However, the result for Kv:Kh is surprising, as one would expect the progress of flow across the meander belt systems to be slowed by a lower Kv:Kh ratio due to the increased resistance to water moving vertically between channels.

4.3 Property Uncertainty Analysis

In the geological modelling part of the report (Section 3), there are a number of instances where the derived petrophysical relationships have considerable uncertainty, this is especially the case for the Vshale-porosity relationship (Figure 15) and the porosity-permeability relationship (Figure 16). In this section, the effect of this uncertainty on thermal breakthrough times is analysed.

4.3.1 Method

The methodology for this experiment is in many ways similar to that of the sensitivity analysis. For the Vshale-porosity uncertainty, two new versions of the porosity model were made using the minimum and maximum relationships shown in Figure 15. The porosity values were then converted to permeability using the standard (black line) porosity-permeability relationship (Figure 16). For the permeability uncertainty, the base case porosity values were converted to different values of permeability using the maximum and minimum porosity-permeability relationships (blue and red lines in Figure 16).

As the aim of this section is to try and determine a more realistic set of thermal breakthrough times, more realistic boundary and initial conditions were used including rate control for the wells and variable initial temperature and pressure as the starting conditions. Because rate is being used, the results for both temperature change and pressure are analysed. Simulations have been run on the small grid, for 70 years, with the across graben doublet orientation.

4.3.2 Results and Discussion

Figure 31 shows the results of the property uncertainty analysis in terms of thermal breakthrough vs time, whilst Figure 30 is a tornado plot which summarises the information shown in the graphs.

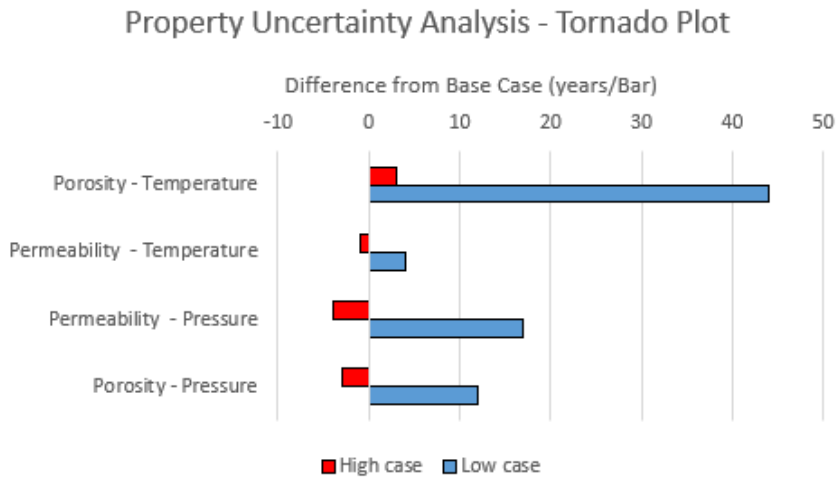

Figure 30: Variation in thermal breakthrough time and BHP relative to the base case for the property uncertainty analysis. Porosity = uncertainty on the Vshale-porosity relation given a set poro-perm relation. Permeability = uncertainty on the poro-perm relation given a set Vshale-porosity relation.

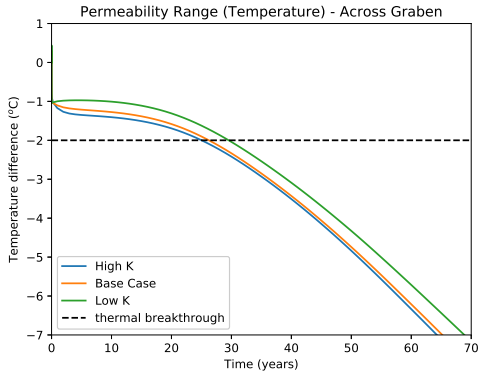

(a) Thermal breakthrough - permeability

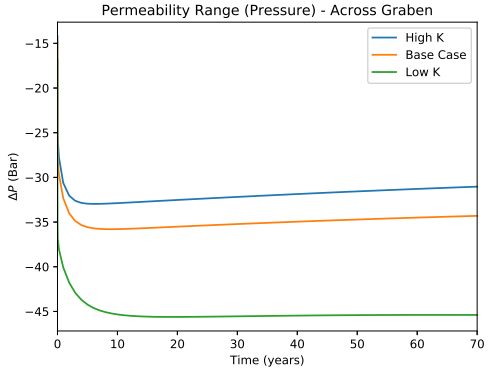

(b) BHP at producer well - permeability

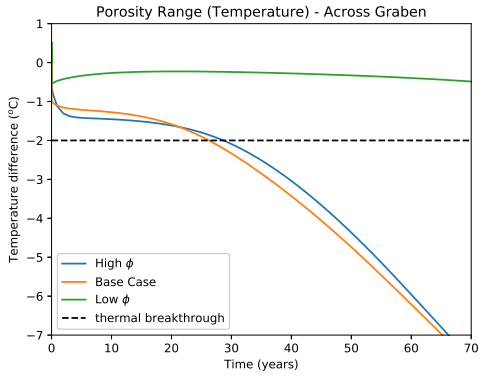

(c) Thermal breakthrough - porosity

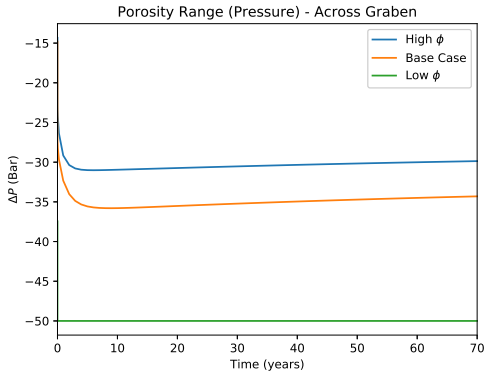

(d) BHP at producer well - porosity

Figure 31: Temperature change at the producer well vs time for the property uncertainty analysis.

From Figure 30, we can see that the Base Case porosity, rather counter-intuitively, represents the earliest of the breakthrough times, with both high and low porosity cases causing an increase in time before thermal breakthrough. This can be explained by the fact that the low case porosity results in a sufficiently low permeability that the producer and injector wells hit their BHP constraints (Figure 31d). This means injection and production rates are lower and thus breakthrough takes much longer. For the high porosity case, the excellent permeability means the injection/production rate can easily be maintained with a low drawdown and therefore there is no difference in rate between the base case and high case. The only difference between the two cases is that the added porosity means there is a larger volume for water to flow through in the reservoir. This has the effect of slowing down the thermal front leading to a longer breakthrough time. The results of permeability variation are simpler. In all cases, the BHP constraints are not crossed, meaning that injection/production is always at a constant rate (8640m^3/day) and breakthrough time is fairly similar in all cases. However, the pressure drop in the producer well required to achieve this rate is much higher in the case of the low permeability scenario than in the Base Case scenario or high permeability scenario (Figure 31b).

4.4 Uncertainty Analysis

During the construction of the geological model (Section 3), two processes relied heavily on stochastic methods: facies modelling and porosity modelling. As these processes are stochastic, the base case model represents only one realisation of many possible realisations. Examples of different statistical realisations of facies and porosity for the small grid are shown in Figure 32 and 33.

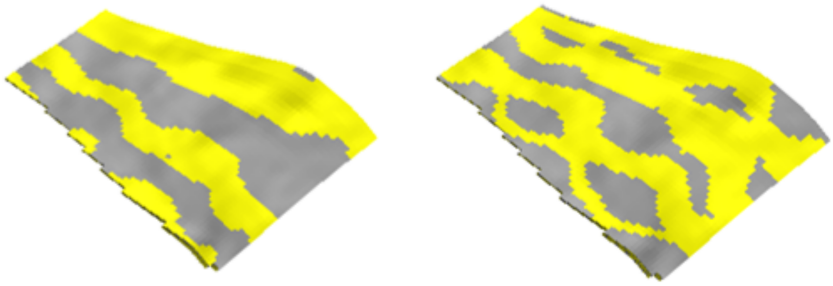

Figure 32: Different facies realisations for the small grid, both grids have the same statistics in terms of facies proportion and honouring well data.

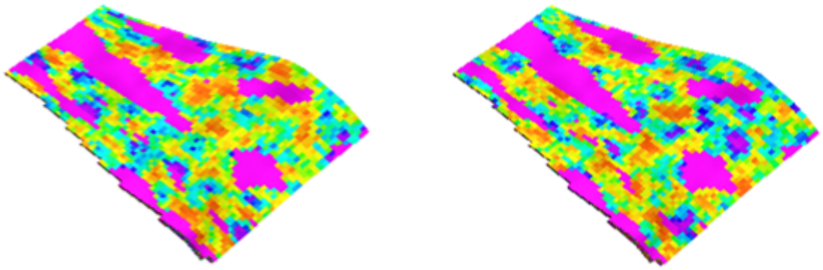

Figure 33: Different porosity realisations for the small grid, both realisations are statistically the same in terms of porosity but spatially, the porosity is distributed differently.

Different realisations do not all behave the same way in terms of local flow and heat transfer. By running simulations on a number of these realisations, one can get an idea of how uncertain the geological model is. Additionally, during the facies and porosity modelling processes, certain values were used to constrain the statistical distributions (channel dimensions, facies proportions, SGS range). These values, like all geological values, have an error associated with them. In this uncertainty analysis, both the the variability associated with different realisations of facies and porosity distribution and the uncertainty associated with the input values controlling the stochastic processes is analysed.

4.4.1 Method

For this section, six different simulation experiments have been run, with each experiment consisting of twenty simulations/realisations. Ideally, far more realisations would have been implemented, however, each of the realisations of the geological model had to be created manually. This was highly time consuming and therefore in the interest of time, the number of realisations was capped at twenty.

Experiment 1: Facies Distribution

In this experiment, the aim was to determine the influence of the position of the meander belts on the thermal breakthrough times. For this, 20 different realisations of the distribution of the meander belts were made. In every realisation, the proportion of the meander belt sand to flood plain clay is the same. Additionally, SGS with the same seed was used for all the realisations. What this means is that if a meander-belt is placed in the same position, in two different simulations, it would have the same spatial porosity distribution. This concept is shown in Figure 34. It should be noted that in all of the realisations the statistical distribution of porosity is the same (the same mean, range etc).

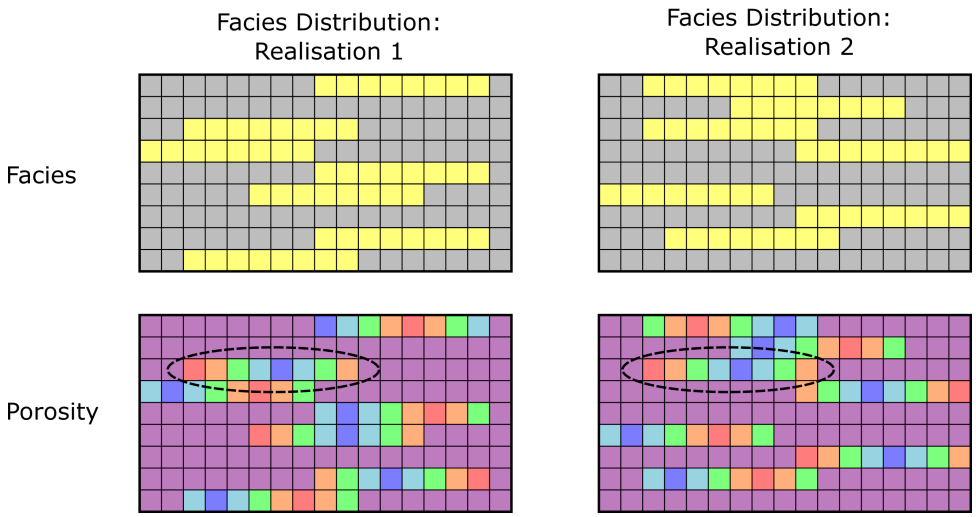

Figure 34: Two hypothetical facies realisations. The dotted circle highlights the fact that if meander belt cells lie in the same position in the grid, then the porosity distribution in those cells will be the same in the two realisations.

Experiment 2: Porosity Distribution

In this experiment, the distribution of the meander belt facies is the same in every realisation (the same as the base case). However, the spatial porosity distribution within the meander belts is different in every case. This is demonstrated schematically in Figure 35. Again, it is important to stress that although the spatial distribution of porosity is different, the statistics of the porosity distribution are the same.

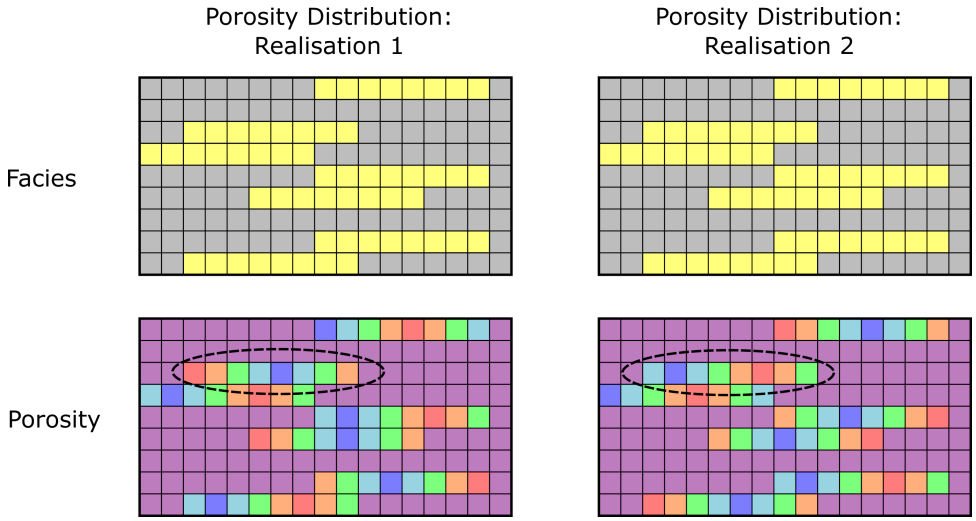

Figure 35: Two hypothetical porosity realisations. The dotted circle highlights the fact that although the meander belt cells are in the same position, the porosity distribution is different.

Experiment 3: Channel Dimensions

In the facies modelling process (Section 3.6), channel dimensions were assigned using the Lorenz et al., 1985 relationship. However, this was only one of three relationships from the literature that could have been used. For this experiment, different facies realisations were created using a range of point bar vs meander-belt width relationships which were drawn at random from the the area shown in Figure 36. Meander belt position was variable and the spatial porosity distribution kept constant as in Experiment 1. N/G in each realisation was always the same.

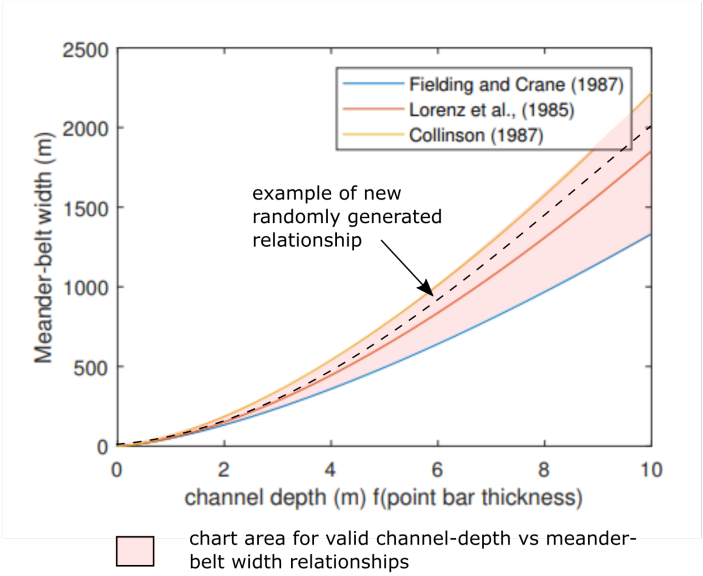

Figure 36: Meander-belt width vs channel depth. The red area represents the range of of possible relationships given by the literature.

Experiment 4: Facies Proportion

In the facies modelling process (Section 3.6), the facies proportion is taken from a facies log and this is assumed to be representative of the whole reservoir. In reality, the average facies proportion could easily be more or less than is given by the logs. To test the effect this has on uncertainty, facies realisations were made with randomly chosen facies proportions (N/G) ranging from -10% to +10% of the base case value. Like in Experiment 1 and 3, meander belts positions vary between realisations, whilst the spatial porosity is kept the same.

Experiment 5: SGS Range

During porosity modelling (Section 3.7), an SGS range of 500m along the graben axis and 300m across the graben axis was used. However, this figure was based on geological intuition and in reality could be very different. To test the effect of this uncertainty in the range of the SGS, porosity was varied from between 750m and 250m ($\pm$0.5) along axis and 150m to 450m across axis ($\pm$0.5). As with experiment 2, the same same facies realisation is used every time and the spatial distribution of the porosity is different in each realisation. However, as with all the other experiments up to this point, the statistics of the porosity distribution are the same in all the realisations.

Experiment 6: Combined Uncertainty Analysis

The final experiment involves combining all of the above factors and uncertainties. That is to say that for every realisation: the meander belt position varies, the meander belt dimensions vary, the overall N/G varies, the spatial porosity distribution is different and the SGS range is different. In addition to all these factors, the uncertainty associated with the Vshale-porosity relationship is accounted for in the different realisations by randomly choosing a Vshale-porosity relationship to generate porosity. Every random relationship lies within the maximum and minimum bounds as shown in Figure 15. What this means, is that for each realisation the statistical distribution for the porosity is different as well. The aim of this experiment is to get a rough idea of the full range of possible thermal breakthrough times when all factors are combined.

All of the experiments outlined above were run on the small grid, using rate control and with a doublet aligned across the graben (Figure 27).

4.4.2 Results and Discussion

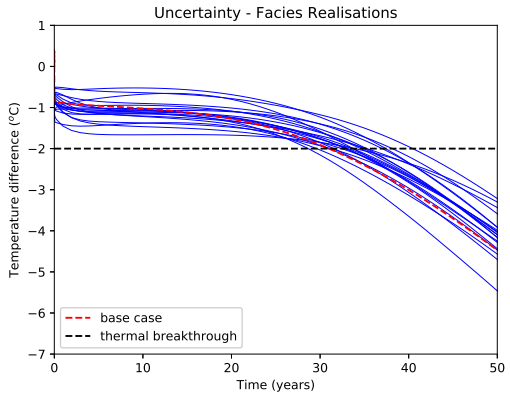

(a) Experiment 1: facies distribution

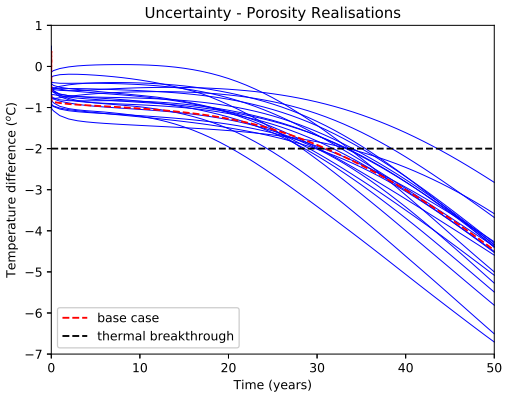

(b) Experiment 2: porosity distribution

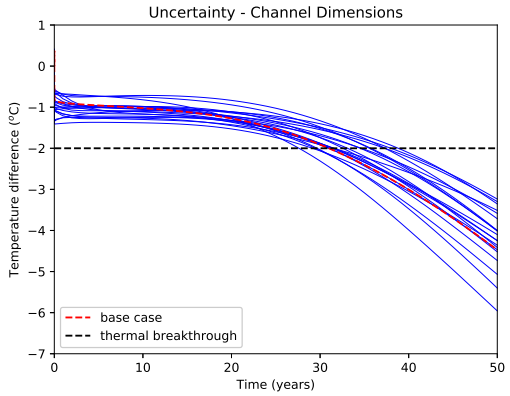

(c) Experiment 3: channel dimensions

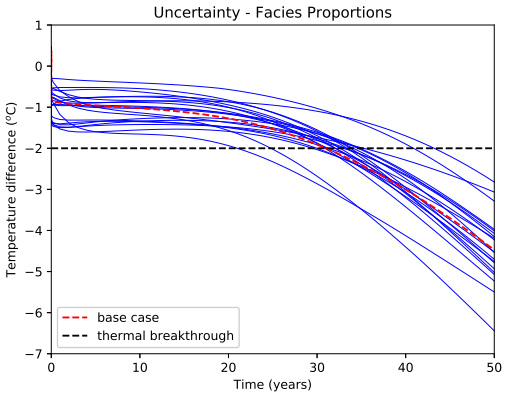

(d) Experiment 4: facies proportions

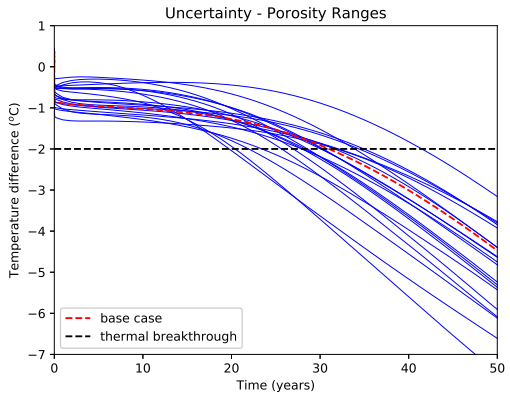

(e) Experiment 5: SGS range

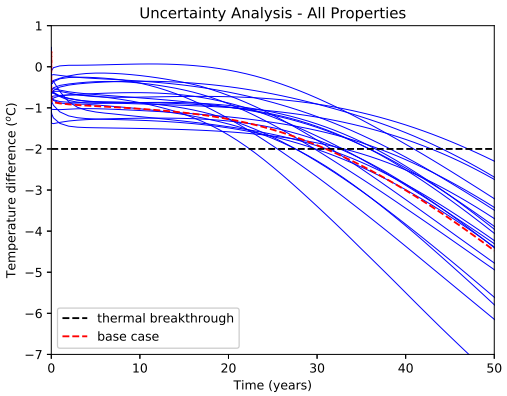

(f) Experiment 6: Combined

Figure 37: Change in temperature at the producer well vs time for the uncertainty analysis experiments.

Figure 37 shows the results of of uncertainty analysis runs. Table 6 shows summary statistics for each of the ensembles in Figure 37, whilst Figure 38 shows the standard deviation of the ensemble members in graphical format.

Experiment	Base Case thermal breakthrough (years)	Mean thermal breakthrough of ensemble members (years)	Standard deviation of ensemble members (years)	Total range of ensemble members (years)
1 (Facies)	31	33.9	2.68	11
2 (Porosity)	31	31.8	4.81	24
3 (Channel Dimensions)	31	33.1	3.2	11
4 (Facies Proportions)	31	32.6	4.55	22
5 (SGS Range)	31	29.1	5.11	21
6 (All)	31	34.3	6.19	26

Table 6: Summary statistics for the uncertainty analysis

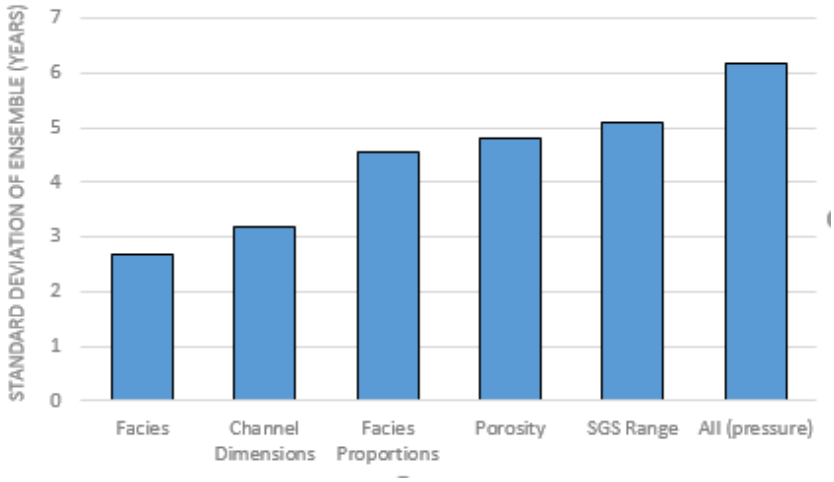

Figure 38: Standard deviation for the experiments of the uncertainty analysis.

Perhaps the most important result from the uncertainty analysis, is that from Experiment 6, where all uncertainty parameters have been combined (final row of Table 6). By combining different channel configurations and sizes, different porosity distributions within channels and incorporating the uncertainty on the porosity values themselves within the realisations, most of the major causes of geological uncertainty are accounted for and thus a good idea can be gained of the likely range of breakthrough times that may be expected. Although the range of uncertainty is quite large (26 years from shortest to longest breakthrough and 6.2 years standard deviation), it is promising to see that none of the 20 simulations run have such poor reservoir characteristics that BHP limits are completely surpassed and the wells cannot produce at the desired rate (as was the case for the lowest porosity scenario in the property uncertainty analysis (Figure 31c)). This suggests that given the range of uncertainty for properties within the Delft Sandstone, geothermal doublets should perform reasonably. However, this result should be treated with caution due to the number of realisations it is based off of. 20 realisation is definitely not enough to cover all combinations and all the ranges for each of the inputs and thus, ideally, many more realisations would be run.

The running of experiments where only one factor is changed at a time also gives an insight into which factors contribute the most to uncertainty in thermal breakthrough time. From Figure 38 it can be seen that different meander belt distributions (Facies) and sizes (Channel Dimensions) seem to cause far less variation in thermal breakthrough than changes in porosity distribution. This is probably because with the high N/G nature of the Delft sandstone, there are always enough flow paths from producer to injector to allow reasonably similar breakthrough times independent of the way the channels are spaced. In contrast, if the porosity distribution inside the channels is changed then this may completely alter the position of the high permeability flow paths meaning water takes far longer or shorter times to reach the producer, hence the variability associated with different porosity distributions is high (Figure 38). We can also clearly see from Figure 38, that the proportion of facies does play a significant role, this is understandable considering that variable amounts of sand in the

reservoir both changes the volume of the reservoir available for flow and dictates the tortuosity of flow paths in the reservoir (few channels mean the flow will have to take a longer more tortuous route).

Finally, we can see from Figures 37a to 37f, that there is initial spread in the temperature distribution of the different ensemble members. This is believed to be the result of a combination of factors. Firstly, the different permeability distributions around the well in each simulation causes variation in the pressure drop experienced by the well, this in turn results in variable enthalpy/temperature changes. Secondly, the simulator version used does not account for gravitational effects and therefore there is some pressure equalisation which also occurs early on in simulations, this may also influence the spread. Regarding the second point, work conducted by Wang and Voskov (2019a) suggests that the influence of the gravitational effect is minimal.

5 Well Placement

Positioning, number and arrangement of wells can play an important role in determining the productivity of a geothermal development. In particular, these factors strongly control the temperature of the water produced, pressure changes in the reservoir and production lifetime. In this section, a study is carried out on the effect of well configuration, spacing and orientation on thermal breakthrough times in the Delft Sandstone. It should be noted, that due to time limits imposed on the project, the study of well configurations is relatively rudimentary and is focused on identifying the major influences of well position on thermal breakthrough.

5.1 Well Configuration

When placing geothermal doublets, two main considerations need to be taken into account: productivity of the doublet and pressure response of the reservoir (this of course excludes logistical considerations such as surface location, length of well, etc but that is outside the scope of this study). Because the wells will be under a residential area, strong pressure depletion of the reservoir is not acceptable, therefore all configurations of wells considered have a 1:1 producer-injector ratio to try to maintain reservoir pressure. With this said, the two configurations considered are as follows: line-drive (Figure 39a) and diagonal configuration (Figure 39b).

(a) Line-drive configuration

(b) Diagonal configuration

Figure 39: Different well configurations with an injector:producer ratio of 1. Producer wells are in red and injector wells are in blue.

5.1.1 Method

To examine the performance of each of the configurations shown in Figure 39, two experiments were run, each with three sets of two doublets arranged in either line-drive or diagonal configuration. The layout of the producers and injectors on the large grid for both experiments is shown in Figure 40. The reason for using three sets of four wells was to determine if local reservoir characteristics affect the performance of the two doublet configurations differently. The experiments were run for 50 years using rate control and with variable initial temperature and pressure. Faults were set as closed to stop communication between doublet sets in different grabens. For this experiment, wells were set at a standard distance of 1.3km apart (a value used by IF technology for injector-producer separation). A more detailed study of the effect of distance between wells has been carried out in the next section.

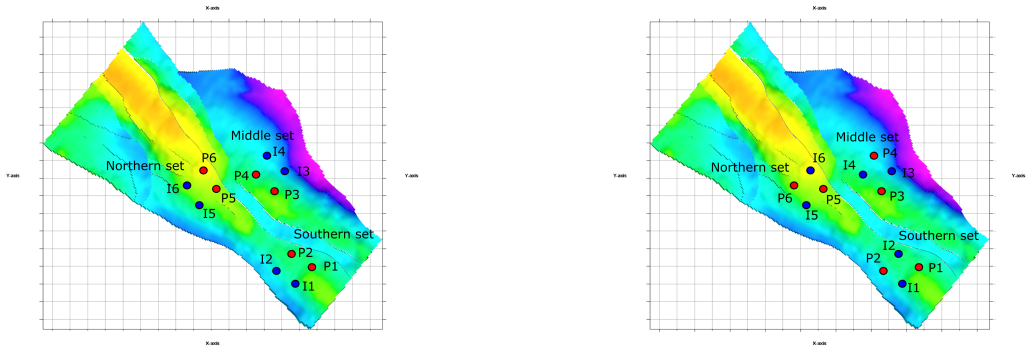

(a) Line-drive configuration

(b) Diagonal configuration

Figure 40: Well positions for the well configuration experiment.

When analysing well performance, it is important to consider both energy production but also how much the wells perturb the pressure field. If the pressure field is altered too much then problems with compaction/subsidence and induced seismicity are likely. For analysing reservoir pressure, the two well configurations for the southern set were also run on the small grid with exactly the same well distances, well controls and boundary conditions as used on the larger grid. The reason pressure wasn't analysed on the full grid, is due to complications related to plotting the full grid data.

5.1.2 Results and Discussion

To be able to compare the performance of the well sets from each section of the reservoir, each set has been analysed separately. Additionally, to determine overall production well performance, an average of the production temperature for the two producers in each set has been taken. This gives an effective way of comparing the performance of the sets of four wells in the two configurations. The production temperature curves for each individual producer in a given set may be found in Figure 81, Appendix B. The results of the experiments are shown in Figure 41.

For pressure analysis, maps of vertically averaged pressure (an average of all the grid cells in the z-direction at every x,y position) were made of the small grid. Vertically averaged pressure is used because the meander belt systems mean there can be locally, very variable pressure in each layer. An average gives a much better idea of general reservoir pressure. The pressure maps for in-line and diamond configurations are shown in Figures 42b and 42a.

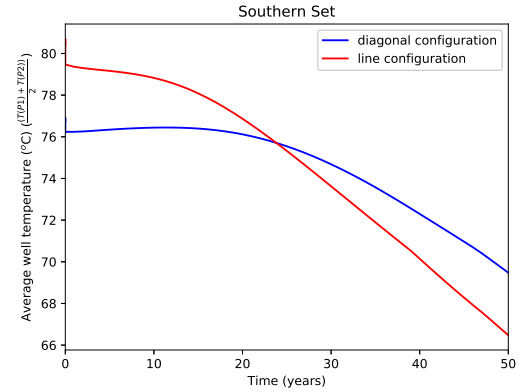

(a) Southern set

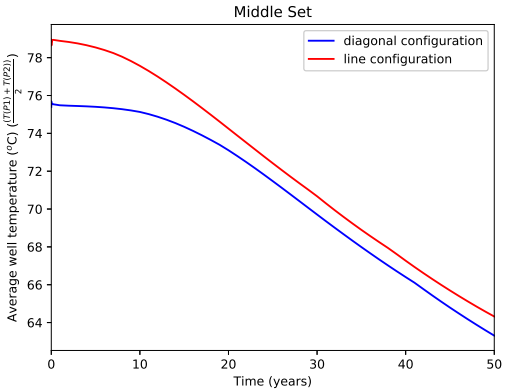

(b) Midde set

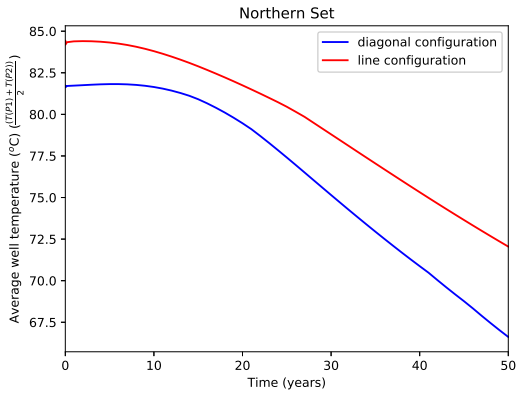

(c) Northern set

Figure 41: Average temperature at the production wells vs time for different well sets - well configuration experiments.

For the northern and middle set of wells (Figure 41c and 41b) the line-drive configuration clearly performs better than the diagonal configuration as shown by the higher average temperature of

production. The reason for this higher average temperature is that in the line-drive configuration both producer wells sit in the deeper and thus hotter section of the reservoir, whereas in the diagonal configuration one of the producer wells will always be sat up-dip in a cooler section of the reservoir. In the southern set, where the reservoir is both thicker and flatter, the situation is slightly different. Although initially the wells of the line-drive are more thermally productive, the temperature quickly drops off to below that of the diagonally configured wells which show greater thermal longevity. The cause of this steeper thermal breakthrough for the line-drive configuration is believed to be the result of a faster rate of propagation through the reservoir, which is in turn linked to differences in the pressure fields which are generated by the two configurations (Figure 42).

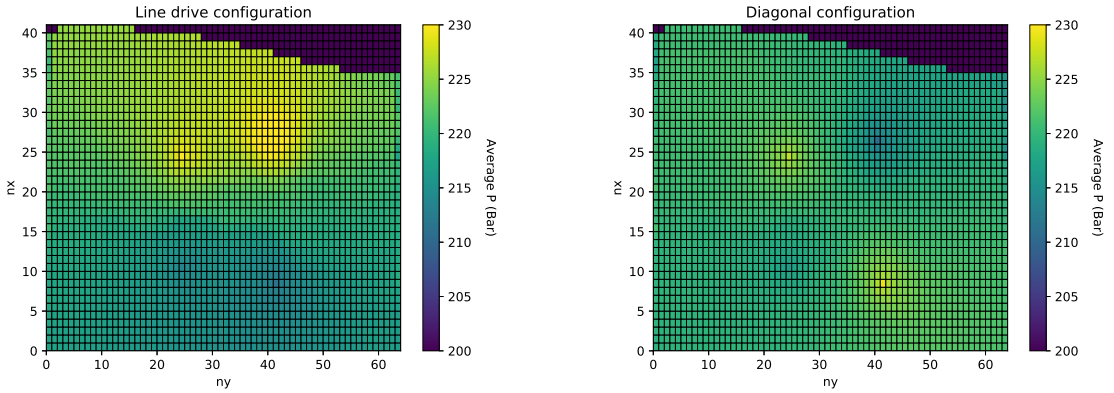

(a) line-drive configuration

(b) diagonal configuration

Figure 42: Vertically averaged reservoir pressure maps for the small grid - well configuration experiments

From Figures 42a and 42b, it is obvious that the diagonal configuration results in a much more even and less extreme pressure distribution. The smaller pressure gradients generated by the diagonal configuration are the reason for the delayed thermal breakthrough when compared to the line-drive configuration in which pressure build-up/depletion on each side of the graben causes more rapid fluid flow. In addition to the faster breakthrough, large scale build-up or depletion in certain areas of the graben, especially those close to fault systems, can cause changes in stress field, fault reactivation and seismicity. Therefore, with the well configurations, there is a slight 'catch-22'. The line-drive configuration tends to perform better in terms of thermal production thanks to having two producer wells down-dip, however, it is at the expense of maintaining an even pressure distribution throughout the reservoir which can result in reduced lifetime of the doublet and potentially seismicity issues. It is therefore suggested that for choosing doublet configurations, a study should be conducted examining the conditions of the local reservoir (including the reservoir thickness, the reservoir slope, the proximity to fault systems and the interference from any other doublets) and based on this study the most productive configuration should be chosen.

The findings of this section are slightly at odds with those reported in the work by Willems (2017). Willems suggests that the more even pressure distribution and greater longevity associated with diagonally configured doublets, means that this configuration is preferable for geothermal developments. This is true for models which are homogeneous and have constant initial temperature, however, the findings of this section suggest that if the reservoir is significantly sloping and the change in temperature along dip is significant that this diagonal configuration may not be optimal.

5.2 Well Spacing

Well spacing appears at first glance to be a fairly straight forward subject which does not need a great deal of investigation. It is logical that the further one puts an injector and producer well apart, the longer the thermal breakthrough time. However, in this section the nature of the relationship between distance and breakthrough time is examined in detail along with how doublet systems interact with each other to affect breakthrough time.

5.2.1 Method

Experiment 1

The aim of the first experiment is to examine the importance of convective and conductive heat flow on thermal breakthrough time. For the experiment, a homogeneous box model has been used. Figure 43 shows the set up for the experiment. In each simulation set, a more distant producer well is used in combination with the injector. For each simulation set, the simulation is run twice. In the first simulation, the model was run so that heat transfer only occurs by advection, there is no energy transfer with the rock at all. In the second simulation, the model was run with both conduction and advection. The DARTS simulations were run using rate controlled wells for 100 years. Full details of the box model and simulation parameters are given in Table 16 in Appendix B. For every simulation set, the thermal breakthrough times (a drop of 2^{o}C in the producer well) were recorded. The results are shown in Figure 46.

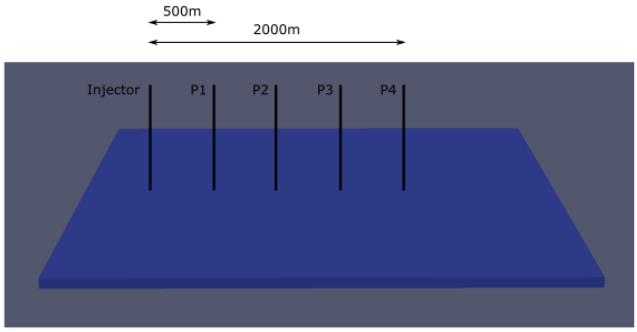

Figure 43: Box reservoir and doublet positions for the thermal breakthrough vs distance experiment (Experiment 1).

Experiment 2

Experiment 2 has been run to verify the results of Experiment 1 on the geological grid. For this experiment, the small grid was used with wells configured diagonally and spaced equidistantly at distances of 2000m, 1500m 1000m and 500m as is shown in Figure 44. The wells were rate controlled and the simulation was run with all heat transfer mechanisms active for 100 years. As in Experiment 1, the breakthrough times for the producer one well were recorded for the different inter-well distances. The results of the experiment are shown in Figure 47.

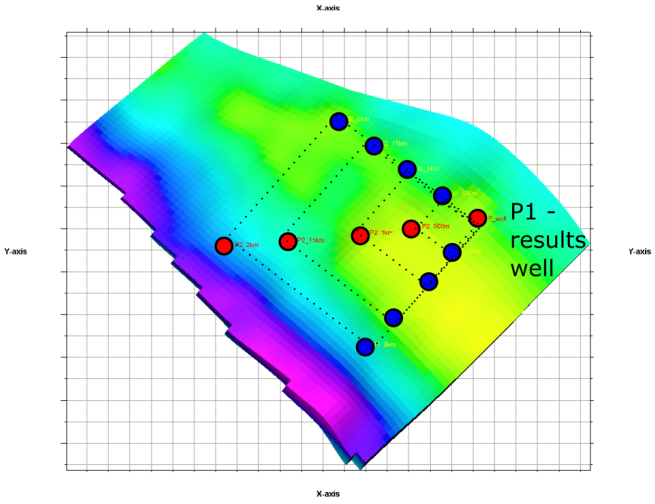

Figure 44: Well configurations for the thermal breakthrough vs distance experiment (Experiment 2). Black dotted lines link the wells used in each simulation run.

Experiment 3

This final well distance experiment examines the influence of the proximity of in-line doublets on both breakthrough time and pressure distribution. For the experiment, six doublets were placed on the small grid in a configuration which is shown in Figure 45. Distance between producer and injector wells is constant at 1.3km. For the experiment, initially only the Base Case well pair were run so as to act as a benchmark for the other experiments. Then simulations were run with two doublets as is outlined in Table 7. Wells were run using rate control. The results of the experiment are shown in Figures 48 and 49.

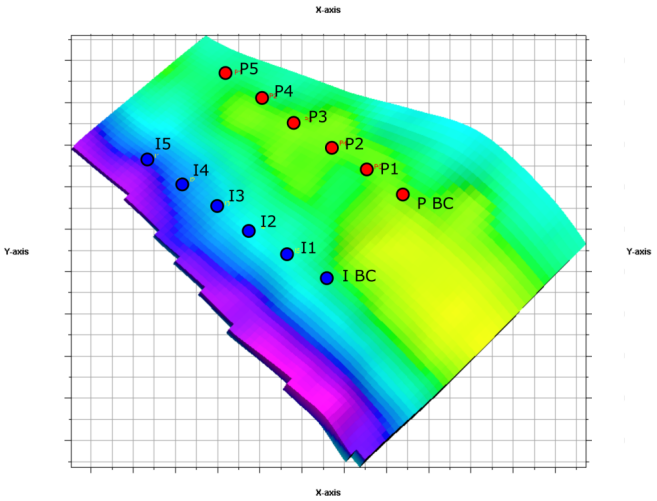

Figure 45: Well distribution for the in-line interference experiment (Experiment 3)

Simulation number	Producers and Injectors used	Distance between doublets (m)
BC	PBC-IBC	N/A
1	PBC-IBC, P1-I1	500
2	PBC-IBC, P2-I2	1000
3	PBC-IBC, P3-I3	1500
4	PBC-IBC, P4-I4	2000
5	PBC-IBC, P5-I5	2500

Table 7: Experiment summary for in-line interference experiment (Experiment 3)

5.2.2 Results and Discussion

The results of Experiment 1 give an interesting insight into the effect of changing well distance and the role that advection and conduction play. From Figure 46, it can be seen that in both the advection only case and the conduction & advection case, the increase in breakthrough time is exponential with respect to inter-well distance. The exponential nature of the curves can be explained by looking at the radial form of Darcy's law (equation 17). From the equation, we see that the radial term is logarithmic. What this means, is that any increase in radius will greatly increase the area through which flow can occur, which in turn slows the velocity of the injected water front. For propagation of the thermal front in geothermal wells, this effect is magnified, because not only does the increased area reduce the flow rate but it also greatly increases the contact surface area between the water and the rock allowing increased thermal recharge. The importance of this effect can be observed in Figure 46 by looking at the difference in solution between the advection only and advection & conduction solution. We can see that the thermal breakthrough time for the advection only solution is far less than the advection & conduction solution at large distances. What this means in practice, is that small increases in the distance between the injector and producer well can lead to very large increases in thermal breakthrough time.

$$q = \frac{k2\pi h\Delta P}{\mu Ln(\frac{r}{r_w})} \tag{17}$$

Where: q = volumetric flow rate, k = permeability, h = height of reservoir, h = pressure difference between P at radius and P at the well, μ = viscosity, r = radius and r_w = radius of the well bore.

The findings of Experiment 2 are much the same as Experiment 1, with a large increase in thermal breakthrough time as the wells of the diamond configuration are moved apart. Towards the end of the experiment the curve appears to level out. This is believed to be a result of the boundary faults redirecting injected water towards the producer well, thus influencing the breakthrough time.

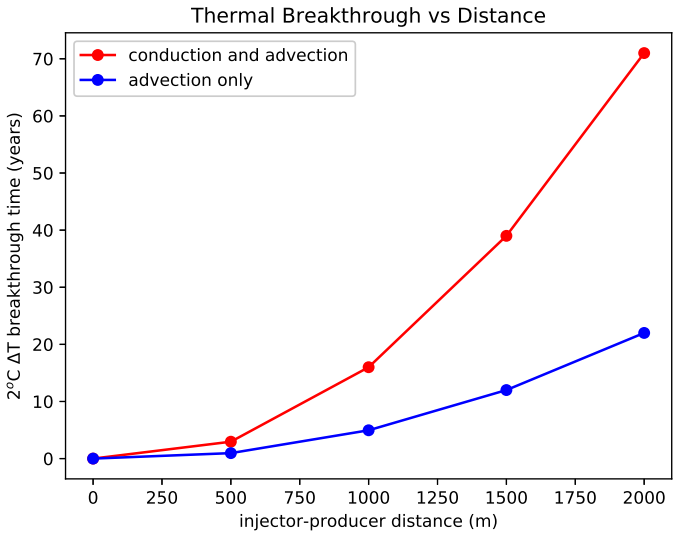

Figure 46: Thermal breakthrough times for injector and producer pairs at varying distances (Experiment 1).

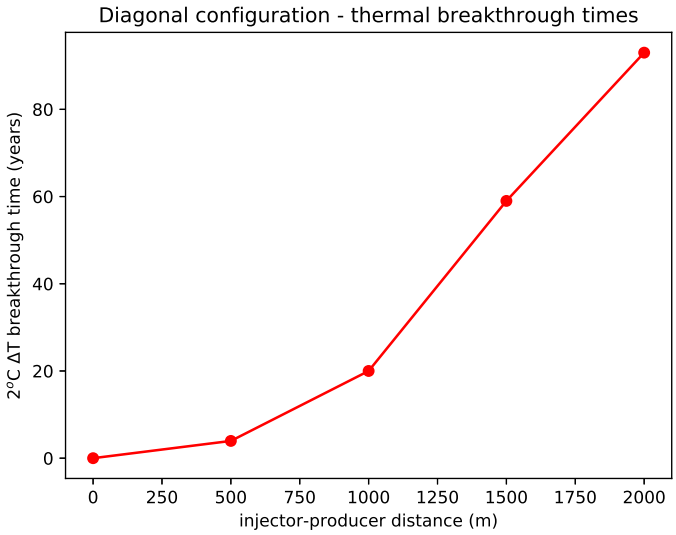

Figure 47: Thermal breakthrough times for injector and producer pairs at varying distances (Experiment 2).

The results of Experiment 3 are given in Figure 48. The results clearly show that the addition of any extra

doublet, even if at quite large distances away (2.5km), has quite a detrimental effect on breakthrough time when compared to that of the single base case doublet. However, once a second doublet is present, reducing the distance between those pairs only reduces the breakthrough time by a fairly small amount as shown by the shallow linear gradient in Figure 48. In terms of pressure distribution, Figures 49a and 49b show the vertically averaged pressure distribution for the small grid from the simulations whereby the line-drive configured doublets are set at 2.5km and 1km apart respectively. The maps show that if doublets are moved close enough together then the pressure depletion/build-up becomes greater over a larger area. This again has implications for fault stability and induced seismicity. Note that the right hand injector well in Figure 49a shows high local pressure as the reservoir is much thinner in this area.

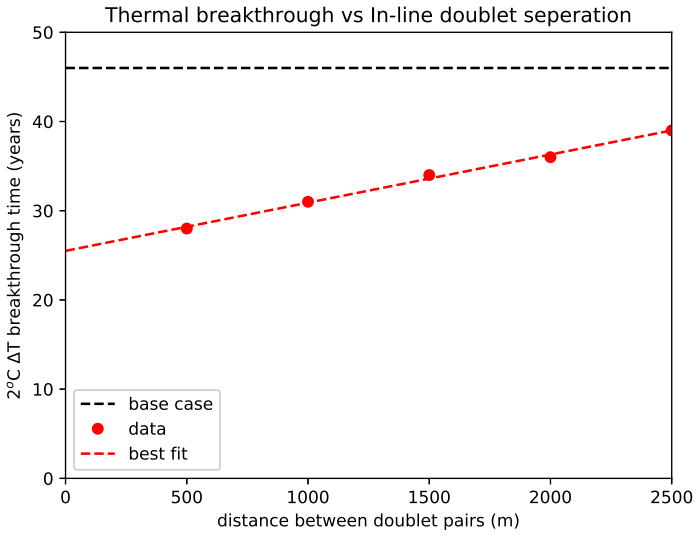

Figure 48: Thermal breakthrough times for well P BC with a second doublet at varying distances along the graben (Experiment 3).

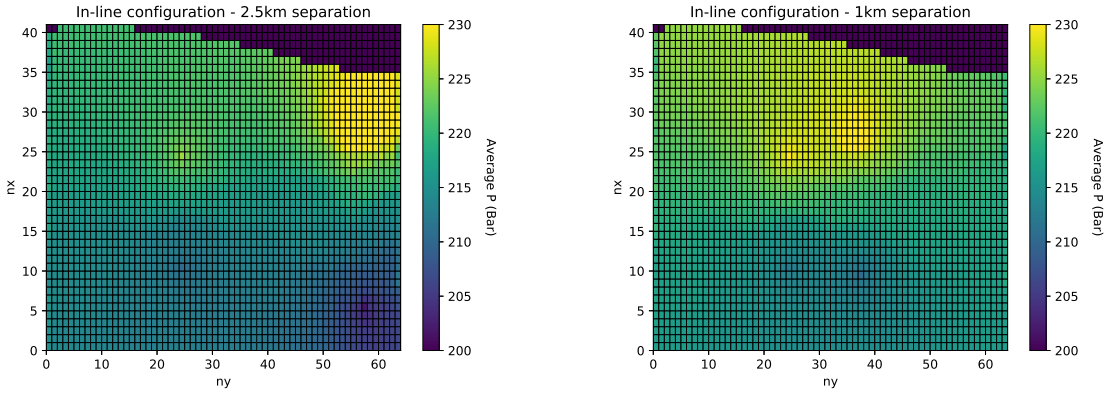

(a) doublet separation = 2.5km

(b) doublet separation = 1km

Figure 49: Vertically averaged reservoir pressure for the small grid - in-line interference experiment (Experiment 3)

5.3 Well Orientation

In the geological modelling section (section 3), it is mentioned that the fluvial system deposits are aligned along the graben axis. This alignment introduces a tendency for flow to move more easily in certain direction than in others, this is referred to as geological anisotropy. The aim of this section is to

examine what effect this anisotropy has on well performance for doublet pairs aligned in various directions.

5.3.1 Method

In this section, two experiments have been run. The first experiment is designed to try and determine the average difference in breakthrough times between wells aligned along the graben axis and wells aligned across the graben axis. The second experiment is designed to examine the effect of well orientation on the uncertainty distribution.

Experiment 1

In this experiment, the large grid is used in combination with six doublet pairs. Two simulations have been run. In the first, the doublets are orientated perpendicular to the graben axis and in the second, the doublets are orientated parallel to the graben axis. This layout is depicted in Figure 50. The wells are set at a standard 1.3km apart and are run using rate control.

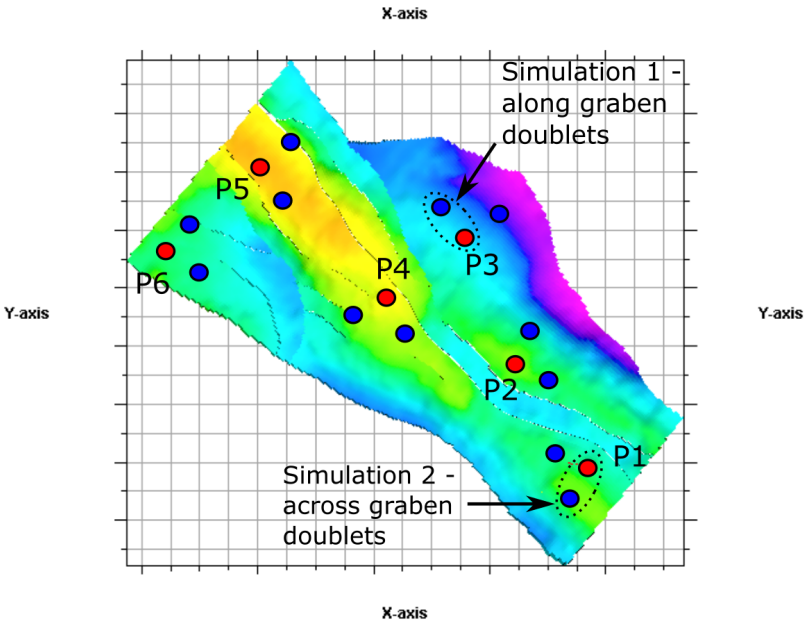

Figure 50: Positions of doublets aligned across and along the graben axes - well orientation experiment (Experiment 1).

Experiment 2

In this experiment, the small grid is used and with only one doublet pair in the model. Like in the previous experiment, two simulation sets have been run, once with the doublet aligned across the graben axis and once with the doublet aligned along the graben axis (as shown in Figure 27). However, unlike the previous experiment, for each doublet alignment, 20 realisations have been run. These realisations of the small grid are the same as those created for Experiment 6 in the uncertainty analysis section (section 4.4.1). The experiment has been run with rate control and with the wells spaced 1.3km apart.

5.3.2 Results and Discussion

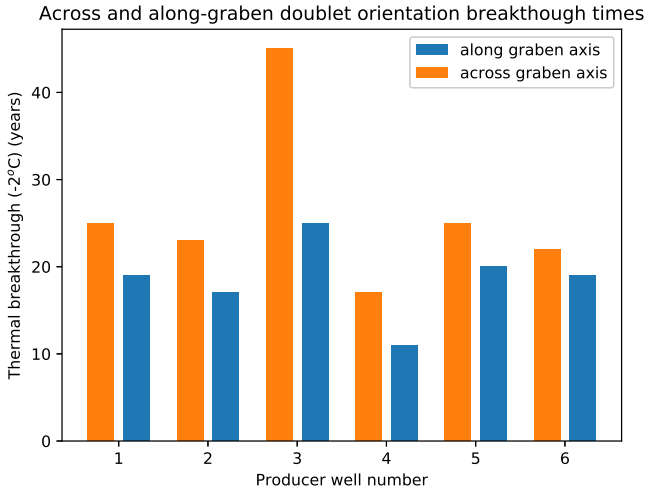

Figure 51: Thermal Breakthrough times for geothermal doublets aligned both across and along the graben axes (Experiment 1).

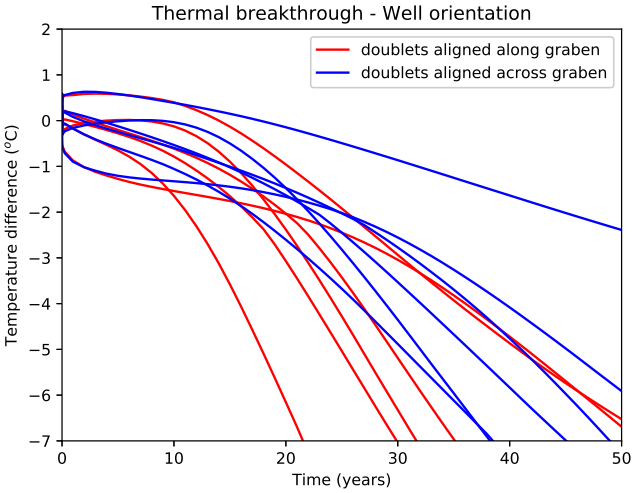

Figure 52: Temperature drop vs time curves for the producer wells of doublets aligned both across and along the graben axes (Experiment 1).

Figure 51 shows that there is a clear tendency for thermal breakthrough to happen faster if wells are orientated in a direction parallel to the meander-belt systems. This is probably because the direct flow paths created by the channels allow for better pressure communication, faster flow and less non-reservoir thermal recharge than if water has to tortuously find its way across the meander-belt systems. This is reflected in the differing shapes of the curves shown in Figure 52, whereby the doublets flowing across the grabens have much shallower temperature decline gradients than their along graben counter-parts. On average, the anisotropy tends to be about 1.4 times the breakthrough time for a doublet aligned across the graben axis when compared to a doublet aligned along the axis, so in terms of longevity it makes sense to align geothermal doublets across the meander-belt systems. Of course, there is a risk that if wells are placed across the graben to get the longer breakthrough times, and N/G or other reservoir properties turn out to be poorer than expected, then the wells may not communicate at all and ability to inject and produce will be severely hampered. However, the work carried out in the uncertainty analysis section suggests that this is unlikely (Figure 37f).

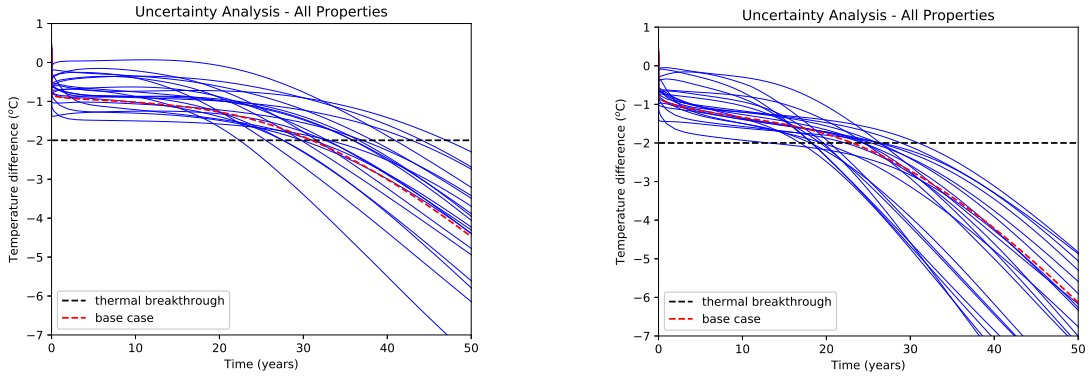

(a) Across graben

(b) Along graben

Figure 53: Temperature drop at producer well vs time - well orientation uncertainty analysis (Experiment 2).

From comparison of Figures 53a and 53b, it can be seen that the uncertainty in breakthrough time in along graben flow is less than that of across graben flow. The suggested explanation for this is the variability of flow pathways. In along graben flow, there will always be flow paths which directly connect the producer and injector wells allowing fairly rapid breakthrough at a similar breakthrough time, independent of channel configuration. Whereas with across graben flow, the flow paths will be far more variable allowing for much more variation in flow velocity and thermal recharge leading to a larger variety in thermal breakthrough times.

6 Geothermal Simulation of Non-Reservoir Lithologies

When examining the conservation of energy equation for low enthalpy geothermal simulation (equation 3 in section 2.2), it was noted that heat energy is transferred through the reservoir in two different ways. The first is via convection, whereby heat is transferred through the bulk movement of molecules, which are in this case water. The second is via conduction, which involves the transfer of heat by vibrations of adjoining particles and atoms. Out of these two methods, heat transfer by convection represents a much more efficient way of transferring heat due to the very high velocities at which fluid will move compared to the velocity at which heat will travel via conduction. However, because convection can only occur when there is bulk movement of particles, this heat transfer mechanism is limited to porous and permeable areas of the reservoir. This means there are large portions of the reservoir, where porosity and permeability do not allow flow and in which the only heat transfer mechanism is conduction. Until recently, it was thought that these internal non-reservoir lithologies played very much a secondary role in controlling the rate of thermal front propagation. However, recent work by Wang and Voskov (2019b) shows that this is not the case and that thermal recharge from non-reservoir lithologies plays a key role in preventing thermal breakthrough, especially in lower N/G reservoirs.

To confirm the results of Wang and Voskov (2019b) and to demonstrate the magnitude of the thermal recharge effect, we utilise DARTS simulation experiments conducted on variations of the small grid model (Figure 27). Four different variations of the small grid have been produced, with variable N/G. The N/G values of the four variations are as follows:

- Reservoir 1 - 30% meander belt deposits
- Reservoir 2 - 50% meander belt deposits
- Reservoir 3 - 70% meander belt deposits
- Reservoir 4 - 90% meander belt deposits

For each of these models, two simulations were run. In the first simulation, all the grid cells are active (both reservoir and non-reservoir cells). In the second simulation, all non-reservoir cells (the floodplain facies) have been removed from the model meaning these cells no longer contribute to the model via conduction. This concept is depicted in Figure 55. For both of the simulation cases, flow should be very similar as any cells contributing to flow are still in the model, therefore any difference in the results can be attributed to the effects of conduction from the non-reservoir lithologies. These DARTS simulations have been run using rate control with the same boundary conditions as described in Section 4.1. The simulations are run for 50 years.

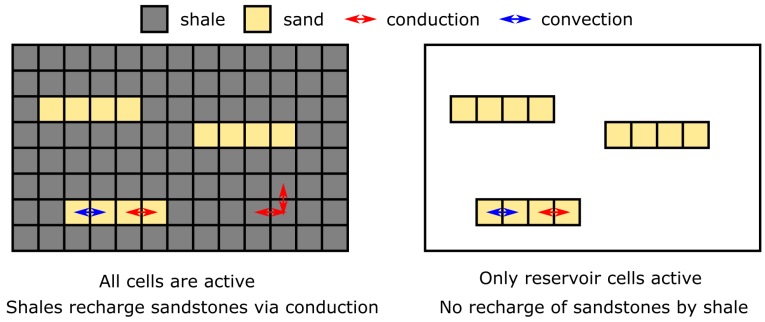

Figure 54: Different simulation set ups for demonstrating the effect of thermal recharge from non-reservoir lithologies.

The results of the experiments are shown in Figure 55. From this figure one can understand the importance of non-reservoir lithologies in thermally recharging injected water. Figures 55b and 55c show that in realistic N/G ranges of fluvial reservoirs, the thermal breakthrough curve is very different depending on whether one accounts for thermal recharge from non-reservoir lithologies or not. Additionally, what is striking is that even though there is a 40% N/G reduction between Figures 55d and 55b the thermal breakthrough time for the solution whereby all the cells are active does not

change much. This is not because the fluid is travelling at the same speed through the reservoir, as is shown by the fact that the dashed solution (only reservoir cells active) is breaking through earlier with reducing N/G. The only plausible explanation for this is that in the lower N/G reservoir, there is a proportionally higher percentage of the reservoir cells in contact with non-reservoir lithology, this in turn results in more reheating of the injected fluid and thus breakthrough time remains reasonably constant.

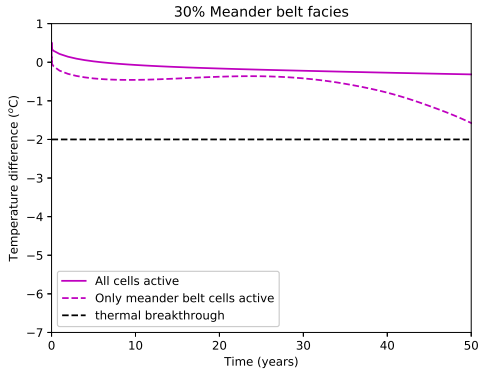

(a) 30% meander belt sand

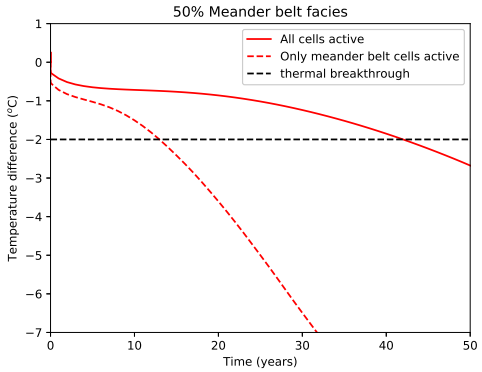

(b) 50% meander belt sand

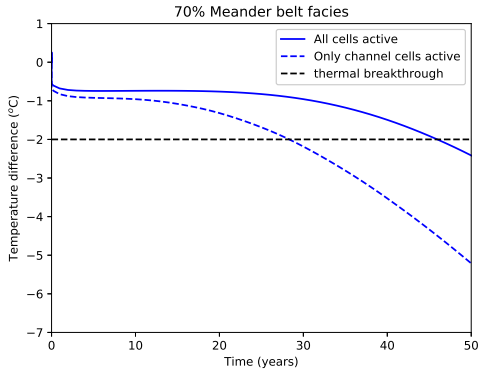

(c) 70% meander belt sand

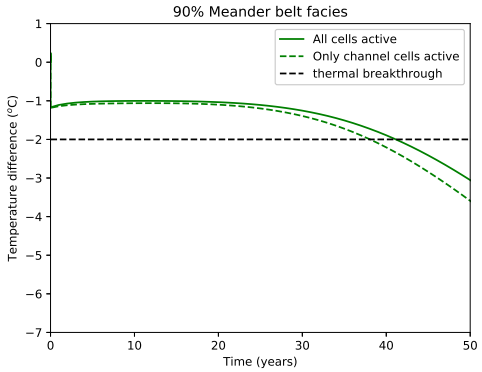

(d) 90% meander belt sand

Figure 55: Temperature change versus time curves which demonstrate the influence of thermal recharge from non-reservoir lithologies on breakthrough time.

Also measured during these simulation experiments was the time taken for each of these simulations to run. These values are displayed in Table 8. The table shows that there is a significant difference in run time between a full-model run and an only reservoir cells run and that this difference is accentuated given lower N/G values. At the small model scale and for single simulation runs, the difference in simulation time is only a matter of seconds and is therefore not of great significance. However, if the models contain millions of cells (as the full model does) and multiple realisations are being run, then the difference in computational run-time time can quickly add up to hours. Therefore, it is clear that if the number of cells in the model could be greatly reduced whilst still accurately accounting for the effects of thermal recharge from non-reservoir lithologies, that would be beneficial.

N/G of Reservoir	**Simulation run time (full model)**	**Simulation run time (non-reservoir cells inactive)**
0.3	189.76	61.52
0.5	237.22	153.78
0.7	264.72	200.10
0.9	233.28	203.26

Table 8: Simulation run times.

The standard way of reducing number of cells in models is through upscaling, a process whereby the properties of multiple cells in the grid are averaged to form one larger cell. Usually, this process is applied across the entire grid, however in highly heterogeneous fluvial reservoirs such as the Delft Sandstone, doing this can result in the loss of important geological details. These geological details and structures are key in governing permeability distribution and flow within the reservoir and as such, full grid upscaling can result in inaccurate simulation results. One of the ways to solve this loss of detail, is to use multi-scale upscaling methods. In these methods, certain areas of the grid remain at a fine scale and other areas are upscaled. In the remainder of this report we look at the feasibility of using multi-scale upscaling methods to upscale non-reservoir lithologies in such a way so that the flow of heat is preserved whilst the numbers of cells within the grid are significantly reduced.

6.1 Models

For the upscaling experiments, three different models have been used for simulation with DARTS. For the local and flow-based upscaling a small synthetic fluvial model of the Nieuwerkerk formation was used, this being the same model utilised by Shetty et al. (2017). The reasons for using a simpler model as opposed to part of the geological model created as part of this thesis are as follows:

- The oblong shape makes for simpler implementation of upscaling.
- The model has a low N/G (0.35) which makes the effect of shale reheating well pronounced and therefore results are easy to interpret.

Figure 56 depicts the model used for analysis along with the position of the injector and producer wells.

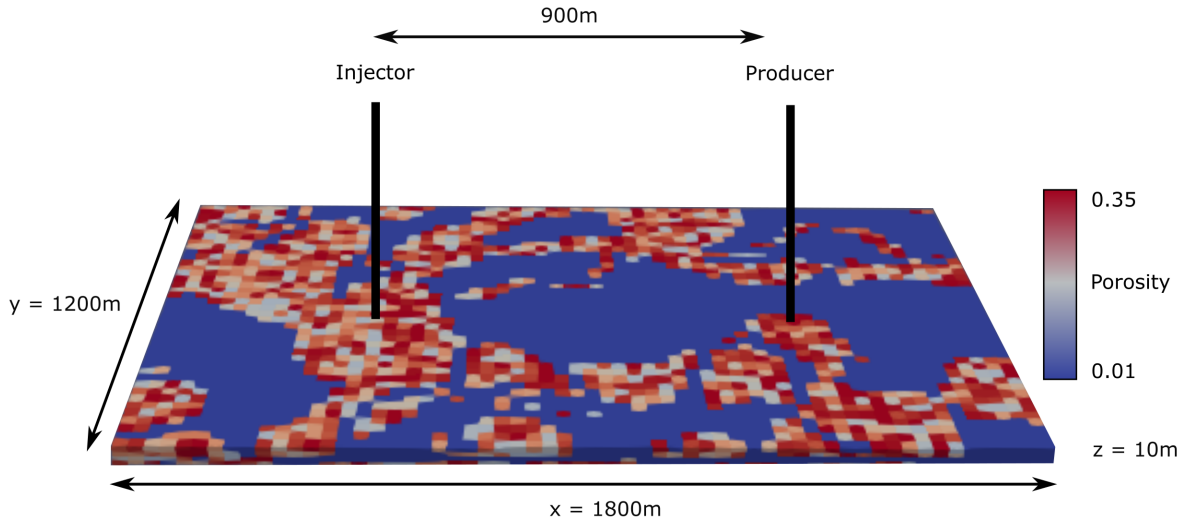

Figure 56: Porosity map of the synthetic model used for the local and flow-based upscaling experiments taken from Shetty et al. (2017).

The parameters used for the DARTS simulations and the model's parameters and boundary conditions are given in Table 17 in Appendix C.

For the multiple sub-region upscaling, simpler models have been used due to the complexity of implementing the upscaling on a grid in which the shale bodies are irregularly shaped. The first of these two models consists of a single rectangular block of non-reservoir lithology surrounded by reservoir cells. The basic layout of the model is shown in Figure 57.

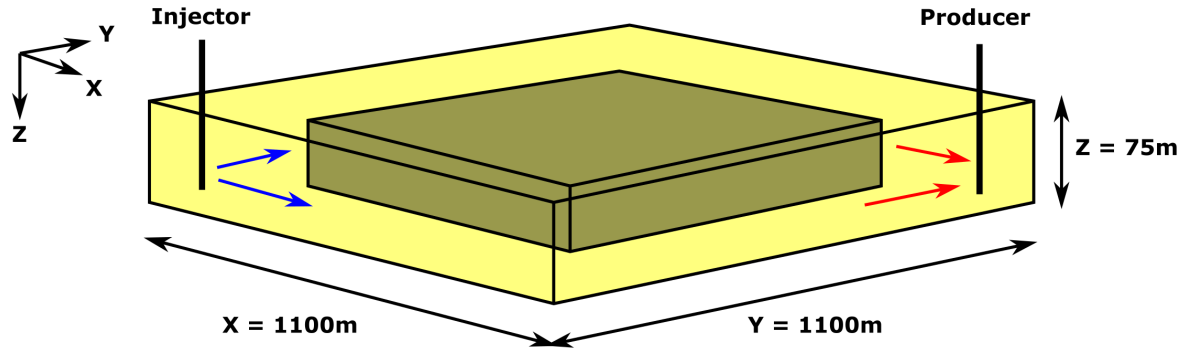

Figure 57: Model 1 used for the multiple sub-region upscaling. Reservoir = yellow, non-reservoir = dark green.

The second model used for multiple sub-region upscaling was designed to be an intermediary model, more complex than Model 1 but less complex than the synthetic fluvial model. The model has a 'sugar cube' layout, meaning it consists of cubes of non-reservoir lithology surrounded by reservoir cells. This is designed to represent a very simplified channel system running through shale flood plain deposits. A 2D slice through the model is shown in Figure 58.

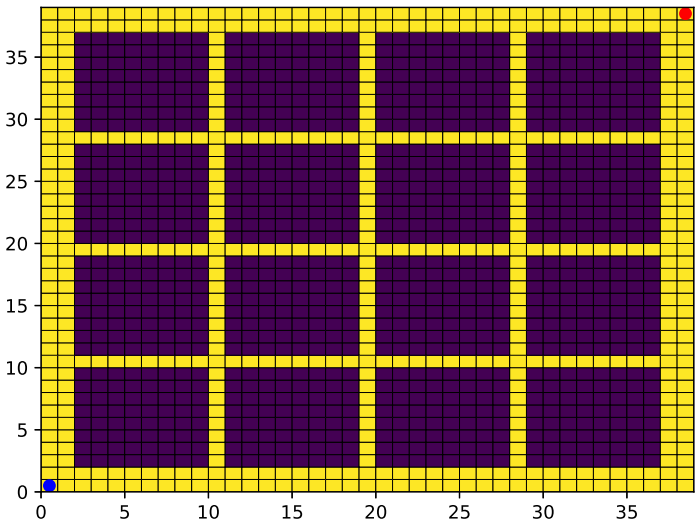

Figure 58: 2D slice through Model 2 showing facies distribution. Non-reservoir lithology = dark blue, reservoir sands = yellow, injector well = blue, producer = red.

The parameters used for DARTS simulations and the Model 1 and Model 2 parameters and boundary conditions can be found in Tables 18 and 19 in Appendix C.

6.2 Local Upscaling

Initially, a very simple method of local upscaling was implemented. With local upscaling methods, the properties of a given upscaled cell are calculated independently of the rest of the grid. The benefits of local methods are that they are very simple and quick to calculate, however, they can be inaccurate. The purpose of utilising simple methods initially was to check if they were suitable (in which case no further investigation was necessary) and also to identify possible problems associated with upscaling for heat flow.

6.2.1 Method

The first stage for all of the upscaling methods was the division of the model into regions to be upscaled. For both local and flow-based upscaling, a coarse cartesian grid was used to divide the finer grid into cubic regions of a pre-determined size. Within these regions, any non-reservoir cells would go on to be upscaled into a single cell via the following method. Figure 59 shows how the division of the grid into regions has been implemented.

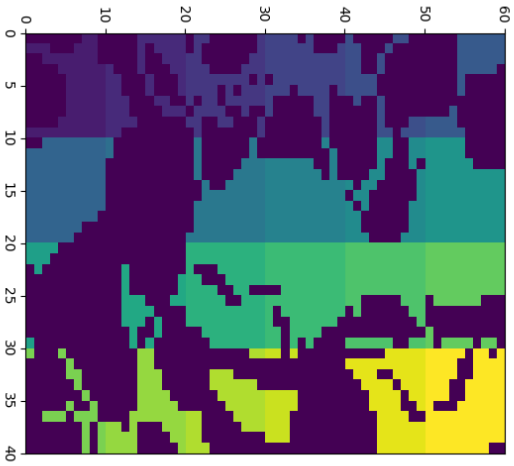

Figure 59: Division of one layer of the synthetic reservoir model into blocks of 10x10x2 cells. Reservoir cells (darkest blue) remain unaffected.

With the grid divided into regions for upscaling, the fine-scale cells within this region then required amalgamation. Amalgamation of cells for upscaling is done via manipulation of connection lists followed by editing cell and connection properties. To demonstrate how connection lists are altered and the grid is re-indexed, a simple example is used. Figure 60 shows a 3x3 grid with its associated connection list.

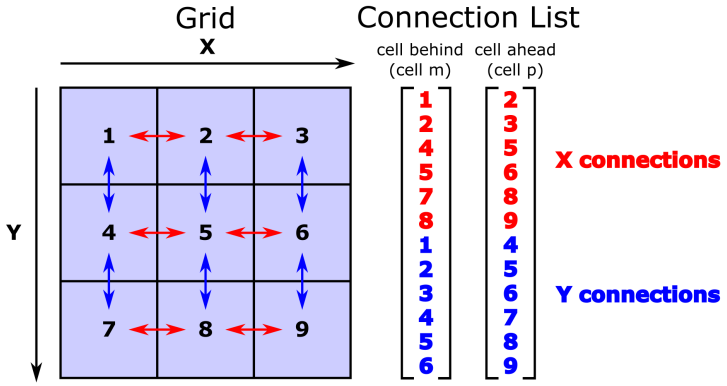

Figure 60: A simple 3x3 simulation grid and its connection list.

.

In this example, the upscaling of the four cells in the bottom right hand corner into a single cell is implemented. In terms of connection list and cell list manipulation, upscaling requires three steps. Firstly, the cells of the grid need re-indexed to account for the reduced number of cells. Then, connections which lie within the upscaled cells need removed from the connection list and finally, connections which connect the fine cells to the upscaled cells require editing to account for the change in cell indices. The implementation of these processes is demonstrated in Figure 61.

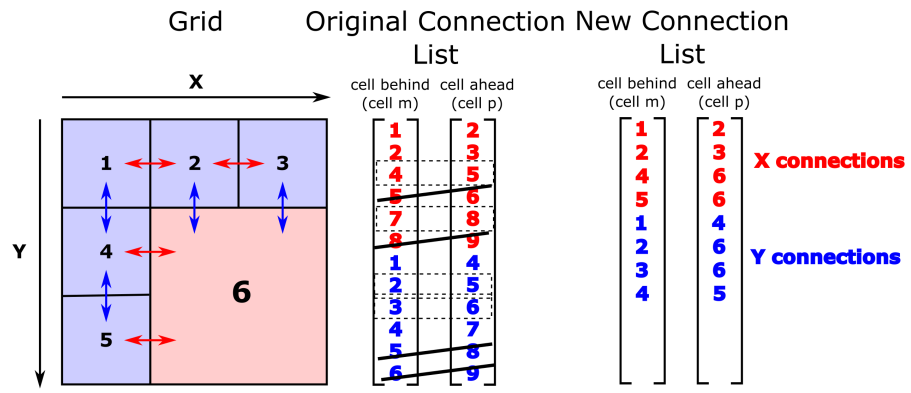

Figure 61: Upscaled and re-indexed 3x3 grid with the new connection list. Solid black lines highlight removed connections, dashed lines highlight edited connections.

In terms of editing cell properties, the properties which need addressed are porosity, temperature and volume. The volume calculation is very simple, with the volume of an upscaled cell (V_I) simply being the sum of the volumes of the constituent smaller cells:

$$V_I = \sum_{i \in I} v_i \tag{18}$$

As in this case, upscaling was implemented on non-reservoir lithologies, the porosity is very low and therefore treatment of porosity is not of paramount importance. In this particular case porosity of the non-reservoir lithology is constant and thus the porosity of the upscaled non-reservoir cell is the same value. However, if porosity of non-reservoir lithologies does still play a significant role in the simulation, then a volume averaged porosity (ϕ_I) would need to be used:

$$\phi_I = \frac{1}{V_I} \sum_{i \in I} v_i \phi_i \tag{19}$$

Similarly, if initial temperature is not constant in the reservoir, then a volume averaged temperature (T_I) should also be used given by:

$$T_I = \frac{1}{V_I} \sum_{i \in I} v_i T_i \tag{20}$$

Finally, the transmissibility and thermal transmissibility lists which control the flow of fluid and heat from cell to cell required editing. Transmissibility is simple because the cells being upscaled are non-reservoir cells and therefore are assumed to not contribute to flow. As such, the transmissibility for the reservoir-upscaled cells could just be set to a very low value.

Thermal transmissbility is more complex and needs to be accounted for more carefully. Assuming thermal conductivity across the grid is constant, then thermal transmissibility (Γ_T) is given by:

$$\Gamma_T = \frac{A}{L} \tag{21}$$

Where A is the area of the connection between two cells and L is the length of connection between two cell centres. For the upscaled cell - reservoir cell connection, the area of the connection remains unaltered. The length does change, however, accurately estimating the distance to the centre of the shale body is difficult as the true centre is unknown. For this reason, it was decided initially to leave the thermal transmissibility of these connections as they were before upscaling. For the upscaled cell-upscaled cell connections, the area is much larger and therefore the value needs altered. To get an approximation of the correct value, the area of all the constituent connections was summed and then this value was divided by the length between the centres of the large cells (equation 22). As mentioned previously, the centre of the large cells do not necessarily constitute the centre of the actual shale bodies and as such this method is only an approximation.

$$\Gamma_T^{IJ} = \frac{\sum_{ij \in IJ}(A_{ij})}{L_{IJ}} \tag{22}$$

6.2.2 Experiment Summary

The experiment run for local upscaling is designed to show the influence of different levels of upscaling when compared to the solution from the fine-grid and 'no non-reservoir cells' cases (see Figure 55 for explanation). A summary of the simulations run for the first experiment is given in Table 9. All simulation experiments are run for 150 years with the parameters outlined in Table 17. The results are displayed in terms of temperature at the producer well vs time.

Experiment 1	
Simulation Name	**Description**
Full Grid	All cells are active in the fine scaled grid
No non-reservoir cells	Only reservoir cells are active
Upscaled - 10	Non - reservoir cells are upscaled into regions of 10x10x2 cells
Upscaled - 6	Non - reservoir cells are upscaled into regions of 6x6x2 cells
Upscaled - 2	Non - reservoir cells are upscaled into regions of 2x2x2 cells

Table 9: Summary of simulation experiments run for local upscaling (Experiment 1)

6.2.3 Results and Discussion

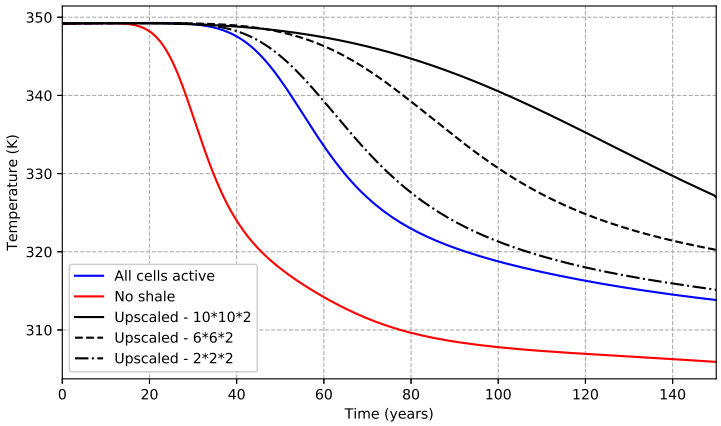

Figure 62: Temperature vs time for local upscaling of non-reservoir cells (Experiment 1)

From the temperature vs time results it is clear that all of the upscaled solutions have a later breakthrough time and a shallower temperature decline gradient than the fine grid solution. What can also be seen from Figure 62 is that as the size of the upscaled blocks is reduced, the upscaled solution moves closer to the fine-scale solution. These observations can be explained by examining enthalpy maps for the upscaled and non-upscaled cases (Figure 63). Figure 63a shows that as flow moves past the non-reservoir lithologies, it quickly depletes the outer most cells of their thermal energy. Once these outer non-reservoir cells are depleted, heat flow from these cells into the injected water will be much lower and conduction from further within the shale is simply not fast enough to recharge these outer cells. This effectively means that thermal energy from the inner areas of non-reservoir cells cannot reach the reservoir cells and so does not contribute to preventing cold front breakthrough. In contrast, Figure 63b shows that large areas of the map have been depleted of thermal energy. The upscaling process which has been applied gives reservoir cells access to the thermal energy from the entire upscaled volume. What this means in practice, is that the upscaled cells can provide far more thermal energy to the reservoir cells given the same thermal transmissibility than the fine cells can. This concept also explains why the solution improves as the upscaled cells become smaller, because as

the size of the upscaled cells reduces, the grid becomes more and more similar to the fine scale grid. The differences in heat flow for the upscaled and non-upscaled case are depicted in Figure 64.

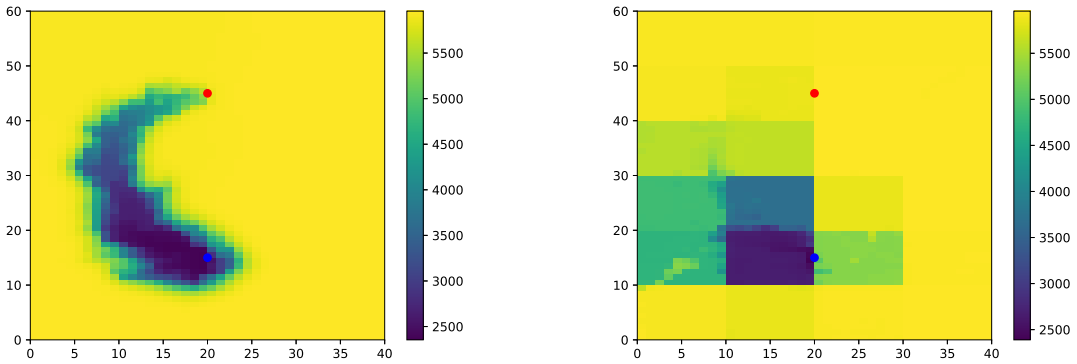

(a) All cells active

(b) Non-reservoir cells upscaled - 10x10x2

Figure 63: Enthalpy maps for simulation runs for local upscaling (Experiment 1) at time = 50 years. Injector well = blue, producer well = red

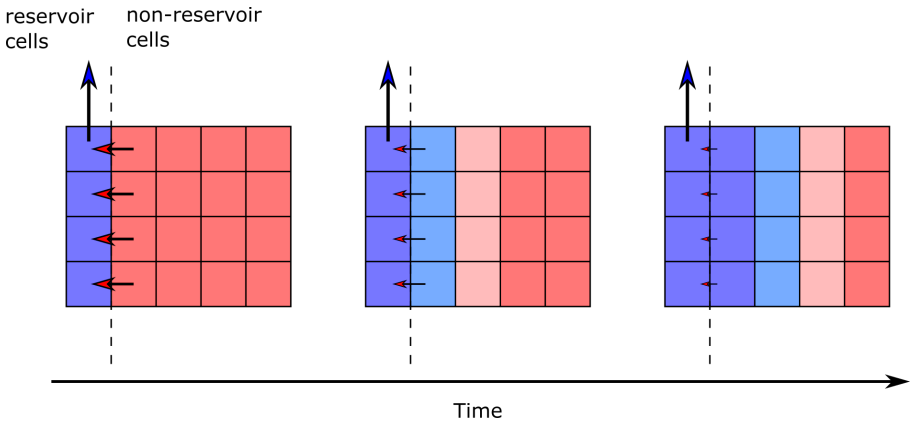

(a) Conductive heat flow (red arrows) from non-reservoir to reservoir cells in the full grid solution. After the outer most layers of cells cool, conductive flux into injected fluid is much lower due to the small thermal gradient. Conductive recharge is not fast enough to recharge these cells significantly.

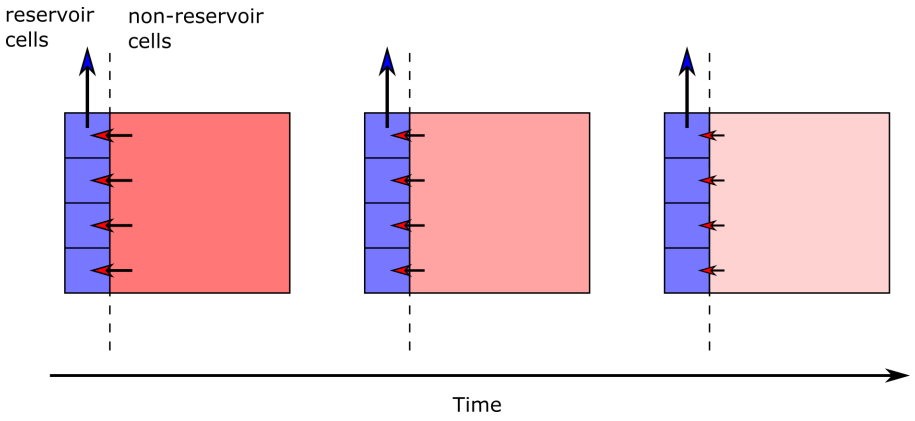

(b) Conductive heat flow (red arrows) from non-reservoir to reservoir cells in the upscaled solution. The upscaled body cools much more slowly than the outer cells in the case given above due to the larger volume. Therefore, conductive flux remains much higher for longer.

Figure 64: Schematic depicting the differences in conductive heat flux from non-reservoir cells into reservoir cells between the upscaled and non-upscaled solution.

The results of the local upscaling serve to show that simply upscaling the cells and leaving thermal transmissbility relatively unchanged results in overly large heat fluxes into the injected water and therefore inaccurate breakthrough curves. As such, different methods have been implemented which attempt to correct the transmissiblity to match the heat flux which flows through the connections.

6.3 Flow-Based Upscaling

Flow-based upscaling utilises simple simulations run on fine grids to calculate flow rates, from which coarse grid transmissiblity values can then be calculated. Determining flow on the fine grid allows much more accurate calculation of the upscaled transmissibility values when compared to local methods. The flow-based method used in this report is based loosely on the one utilised by Karimi-Fard and Durlofsky (2012), however, it has been adapted for use with temperature as opposed to pressure.

6.3.1 Method

Initially, a short simulation was run on the full fine grid with the permeability of the sandstone set very high (1x10^6 mD). The high permeability results in almost immediate breakthrough of the cold front and complete surrounding of the non-reservoir cells that neighbour the flow path with cold water. Conductive heat flow (Q) for all connections in the grid could then be calculated via the following equation:

$$Q_{ij} = \Gamma_T(T_i - T_j) \tag{23}$$

Having found Q of the fine grid, the idea is then to recalculate thermal transmissbility of the upscaled grid so that the Q of the upscaled grid is the same as that for the fine grid. For reservoir - upscaled connections, the new thermal transmissbility could be calculated via equation 24, whilst for upscaled - upscaled connections, the new thermal transmissibility could be calculated via equation 25.

$$\Gamma_T^{iJ} = \frac{Q_{ij}}{(T_i - \overline{T_J})} \tag{24}$$

Where i represents fine-scale reservoir cells, j represents fine-scale non-reservoir cells, J represents upscaled cells and $\overline{T_J}$ is the average temperature of all non-reservoir cells in upscaled cell J.

$$\Gamma_T^{IJ} = \frac{Q_{IJ}}{(\overline{T_I} - \overline{T_J})} \tag{25}$$

Where $Q_{IJ} = \sum_{ij \in IJ} Q_{ij}$.

One of the complexities of applying this flow-based upscaling to temperature as opposed to pressure is that unlike pressure, a truly steady-state situation cannot be achieved. What this means is that Q is constantly changing through time and therefore the thermal transmissibility also changes. The aim is therefore to find a set of upscaled thermal transmissibility values which effectively represent the transmissibility for the whole simulation. Figure 65 shows a plot of the average thermal transmissibility for upscaled non-reservoir cell - reservoir connections (equation 24) through time. What can be seen is that initially transmissibility of the connections declines. This is because the temperature of the upscaled block remains higher for longer, and therefore to balance the flow rate the thermal transmissibility of the connections needs to be reduced. However, towards the end, the thermal transmissibility plateaus. This levelling out represents the arrival of a semi-steady state phase, where temperature decline of the upscaled bodies and heat flux change at a constant rate through time. The logical set of transmissibility values to represent the entire curve is an average of all the points on the curve. This average is shown as a black line in Figure 65. At the point (in time) where the black line meets the red curve, the average thermal transmissibility of the upscaled connections will roughly equal the average transmissibility of the entire curve. Thermal transmissiblity curves for the other two upscaling sizes may be found in Figure 69.

Asides from the altered thermal transmissibility, the rest of the upscaling method is very similar to that described in the local upscaling method (Section 6.2.1).

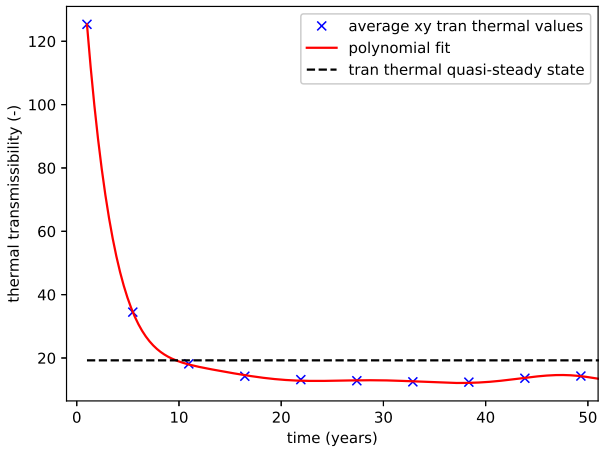

Figure 65: Mean thermal transmissibility of reservoir cell - upscaled cell connections vs time for the upscaling into cells of size 6x6x2. The black line represents the average of transmissibility of the red curve.

6.3.2 Experiment Summary

The experiment conducted for flow-based upscaling was exactly the same as the experiment that was conducted for the local upscaling (section 6.2.2), the only difference being the type of upscaling implemented. A summary of Experiment 2 is given in Table 10.

Experiment 2	
Simulation Name	**Description**
Full Grid	All cells are active in the fine scaled grid
No non-reservoir cells	Only reservoir cells are active
Upscaled - 10	Non - reservoir cells are upscaled into regions of 10x10x2 cells
Upscaled - 6	Non - reservoir cells are upscaled into regions of 6x6x2 cells
Upscaled - 2	Non - reservoir cells are upscaled into regions of 2x2x2 cells

Table 10: Summary of simulation experiments run for flow-based upscaling (Experiment 2)

6.3.3 Results and Discussion

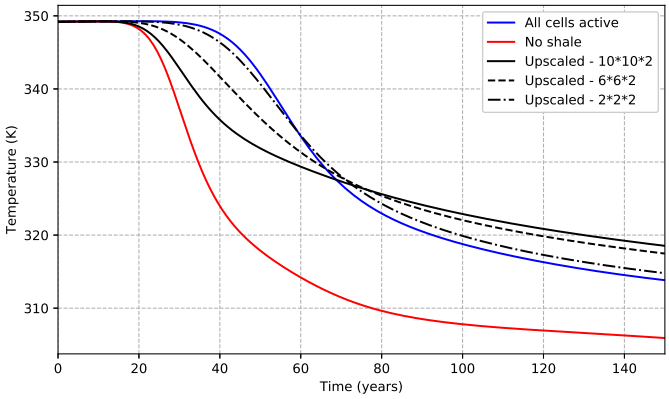

Figure 66: Temperature vs time for flow-based upscaling of non-reservoir cells (Experiment 2)

Figure 66 shows that the use of flow-based upscaling significantly improves the results of the upscaled simulations when compared to local upscaling (Figure 62). The use of calculated thermal

transmissibility values for the upscaled connections means that the total energy being transferred through the connections is much closer to that of the real solution than for the local upscaling. However, Figure 66 also shows that as the upscaled cells become larger, the solution gets worse in terms of accurately representing thermal breakthrough. The reason for this degradation of the solution as the size of the upscaled cells increases is due to the assumption that an average value for the thermal transmissibility is a reasonable representation of the entire thermal transmissiblity curve. Figure 67 shows the 10x10x2 upscaled solution versus the full grid solution, whilst Figure 68 shows the transmissibility curve vs time for the 10x10x2 solution. We observe from Figure 67, that the thermal breakthrough of the upscaled solution occurs earlier than that of the fine-scale solution. This is because the chosen thermal transmissbility values based on the average are initially too low (Figure 68), this means that heat flux into the injected water is not high enough and therefore the breakthrough occurs more rapidly than in the fine grid solution. The problem is a lot less conspicuous for the 2x2x2 solution. This is because the small volume of the upscaled cells means that the new values of transmissbility calculated from the heat flux values are not that different from the original values. This is demonstrated in Figure 69, which shows a comparison between the average thermal transmissibility through time curves for both the 10x10x2 upscaling and the 2x2x2 upscaling. What this means in practice, is that the average of the transmissbility curve for the small upscaled grid (2x2x2) is a much better approximation than that for the large upscaled grid (10x10x2).

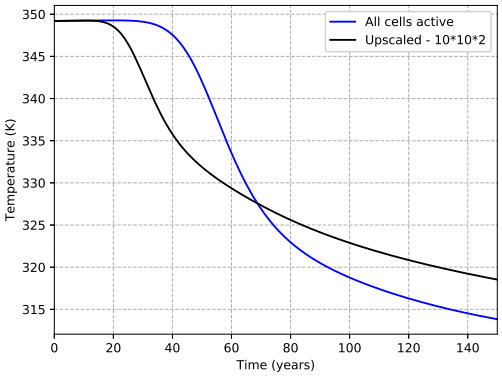

Figure 67: Temperature vs time for the 10x10x2 upscaled grid and full grid models.

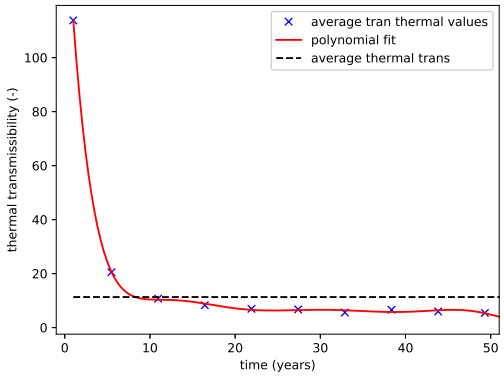

Figure 68: Mean thermal transmissibility of reservoir cell - upscaled cell connections vs time for the upscaling into cells of size 10x10x2.

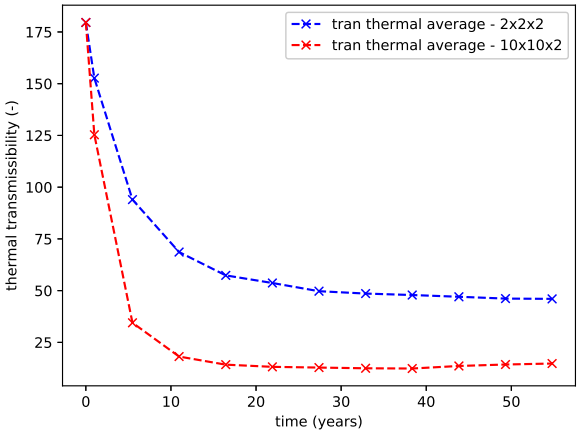

Figure 69: Average thermal transmissibility through time for the upscaled cell - reservoir cell connections for the 2x2x2 and the 10x10x2 upscaled grid.

Resolving the issue associated with the coarser-scale solution would not be a trivial task, because no one single position on the transmissibility curve would provide the correct solution. To get an accurate solution, the whole of the fine-scale grid simulation would need to be run and the transmissibilities adjusted through time to match the changing Q. However, doing this would be defeating the point, as the full fine grid solution could just be run to get the correct solution.

In terms of suitability as an upscaling solution, the flow-based method is far from ideal as very large numbers of upscaled cells are required to make the upscaling accurate and therefore, the potential savings in terms of computational time are minimal.

6.4 Multiple Sub-Region Upscaling

The final method investigated for upscaling of the non-reservoir lithologies was the multiple sub-regions method as used by Awadalla and Voskov (2018), who in turn based their methodology off Karimi-Fard and Durlofsky (2012). This method is similar to flow-based upscaling in that a simple fine-scale simulation is run and used to re-calculate transmissibilities. However, in addition to this, the fine-scale pressure distribution is used to define regions of roughly equal pressure which are then upscaled into single cells. This flow-based gridding technique has been employed to good effect in the modelling of unconventional fractured systems, with the sub-regions used to model the diffusive pressure depletion of the rock matrix (Awadalla and Voskov, 2018). The advantage of this method over upscaling using a standard cartesian grid (as has been implemented so far), is that it preserves the features of the fine grid simulation and captures variability of the property in question more accurately. In this section, the method is adapted for temperature on a simple structured grid.

6.4.1 Method

Initially, the method is similar to the flow-based upscaling, in that a fast, simple simulation was run on the fine grid. However, unlike the previous method, the initial conditions of the simulation were set such that all the reservoir cells start at injection temperature whilst all non-reservoir cells were set to the standard initial temperature. The simulation was then run with no wells in place so that the only energy transfer taking place in the grid is the conductive movement of heat from the non-reservoir cells to the reservoir cells. One of the primary advantages of doing this is that conduction only simulations are very fast and computationally inexpensive.

The initial simulation is left for enough time such that a clear concentric temperature distribution forms in the non-reservoir cells as is shown in Figure 71a. This temperature distribution forms the basis for upscaling. A pre-determined number of temperature bins (in this case 10) are defined which run from the initial reservoir temperature through to the temperature of the injected fluid (Figure 70). The concentrically arranged temperatures of the initial grid are then sorted into these temperature bins to form the sub-regions. For the Model 1 case, the sub-regions are shown in Figure 71b. Each of these sub-regions will go on to be upscaled into a single cell.

In terms of the thermal tranmissibility, at the end of the initial simulation ,Q values are calculated and the thermal transmissibility of the upscaled grid re-calculated in the same way as shown in section 6.3.1. Unlike in the flow-based upscaling method, the time at which the thermal transmissibility is calculated cannot be changed because the length of time which the initial simulation run for also determines the configuration of the upscaled cells. Having recalculated the transmissiblity, the sub-regions are then upscaled in the same way as described in section 6.2.1.

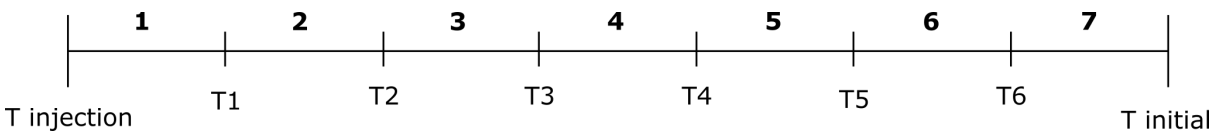

Figure 70: Division of the temperature from the initial simulation into the sub-regions using bins.

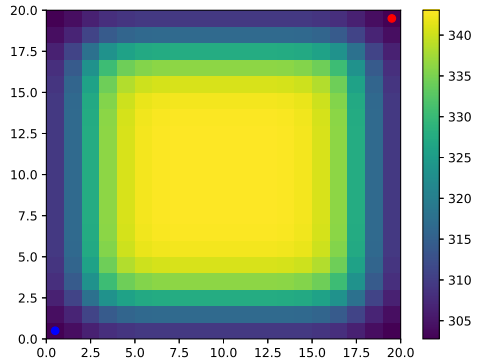

(a) Temperature distribution (^{o}K) for the fine grid simulation at time = 100 years.

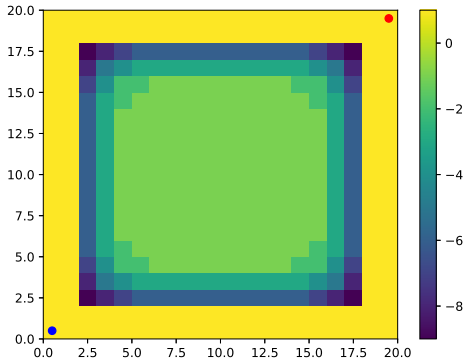

(b) Grouping of temperatures into sub-regions

Figure 71: 2D slices through Model 1 at Z = 9.

Upon running preliminary simulations, an undesirable effect was discovered to be influencing the results. Figure 72a shows a temperature through time curve for a simulation on the upscaled grid for Model 1, whilst Figure 72b shows an enthalpy map through the centre of the reservoir at time = 15 years. From Figure 72a, it is clear that thermal breakthrough is occurring far too early, way before water from the injector has even arrived at the producer. The reason for this early breakthrough can be found by examining Figure 72b. From the enthalpy map, it is clear that despite the fact that the cold front from the injector well is nowhere near the producer well, the water around the producer well is being cooled. The cooling near the producer is a result of the outer layers of upscaled cells having been cooled on the injector side of the body and then acting as a heat sink on the producer side. The effect is almost immediate, because as soon as the upscaled cells are starting to cool close to the injector they also start to cool the hot water near the producer.

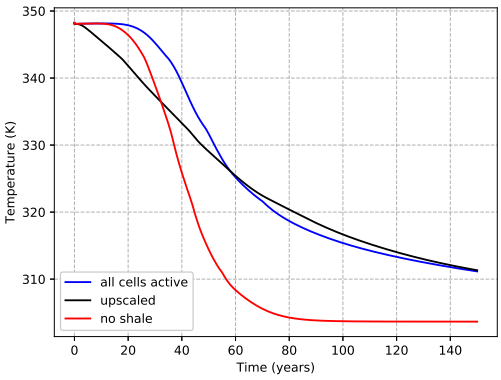

(a) Temperature vs time at the producer well

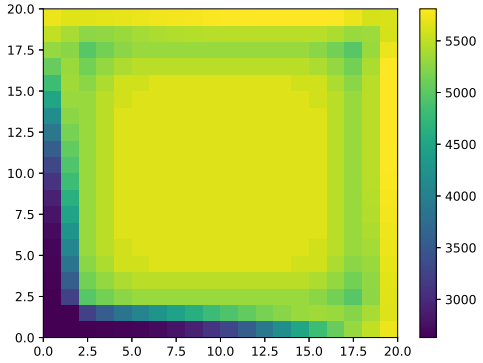

(b) Enthalpy map of the reservoir (Kmol) at Z = 9 and time = 15 years

Figure 72: Plots showing the problem of early breakthrough due to multiple sub-region upscaling.

To solve the problem of this early breakthrough, an adaptation was made to the method. The problem of the early breakthrough is caused by the upscaled cells acting as both a heat sink and a heat source, when in reality they should only act as a heat source. The idea of the time variable thermal transmissibility method is to change the thermal transmissibility such that the upscaled cells may only act as a heat source. This is acheived by shutting and opening various connections at different times throughout the simulation. An explanation of how this method is implemented is given in Figure 73.

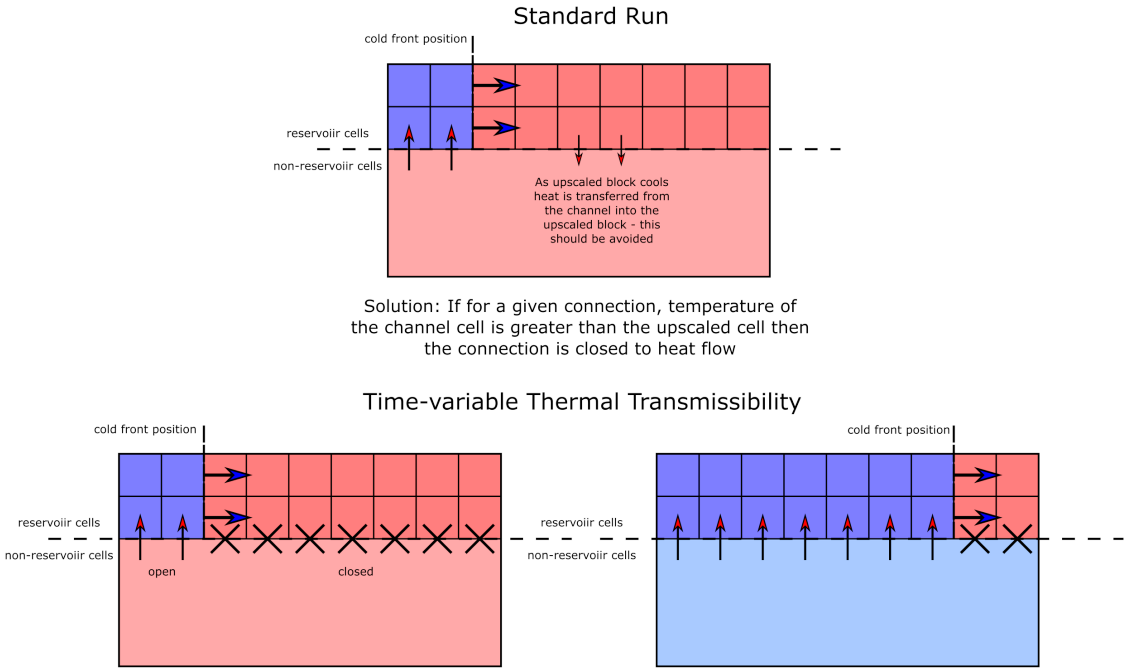

Figure 73: Implementation of time variable thermal transmissibility.

In this section, Model 1 has been used to demonstrate the method, however, the same method has also been applied to Model 2. Figures showing the temperature distributions after the initial simulation and the subsequent sub-regions used for the upscaling of Model 2 may be found in Appendix C (Figures 82 and 83).

6.4.2 Experimental Summary

Experiments run for the the multiple sub-region method have been run on both Model 1 and Model 2, the aim being to determine whether the method works on a model with greater complexity than the very simple Model 1. The simulation runs for both these models are the same and are summarised in Table 11. Parameters used for the different models are given in Tables 18 and 19 in Appendix C.

Experiment 3 (Model 1) and Experiment 4 (Model 2)	
Simulation	**Description**
Full Grid	All cells are active in the fine-scale grid
No non-reservoir cells active	Only reservoir cells are active
Upscaled	Non-reservoir cells have been upscaled using the multiple sub-regions method

Table 11: Experiments 3 and 4 for multiple sub-regions upscaling.

In addition to this experiment, a second experiment was run on Model 2 to test the sensitivity of the upscaled model solution to flow rate by adjusting the injection and production well pressures (Table 12). The upscaled solutions are compared to the full grid solution run at the same flow rate.

Experiment 5			
Simulation	**Injection pressure (bar)**	**Production pressure (bar)**	**Pressure Differential (bar)**
1	231	201	30
2	236	196	40
3	241	191	50

Table 12: Summary of the well pressures used for the flow rate experiment.

6.4.3 Results and Discussion

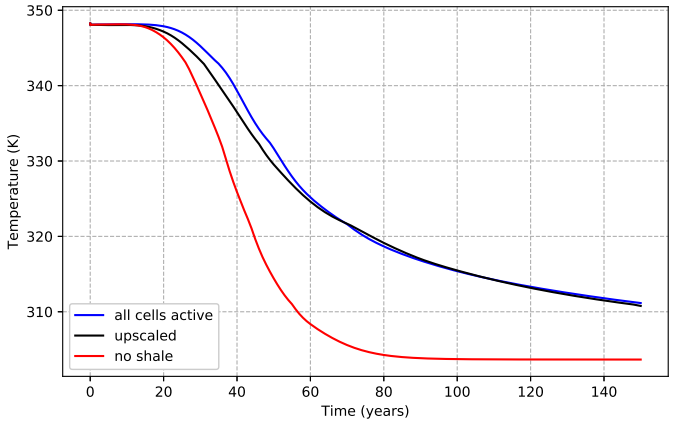

Figure 74: Temperature at the producer well versus time for multiple sub-region upscaling of non-reservoir cells - Model 1 (Experiment 3)

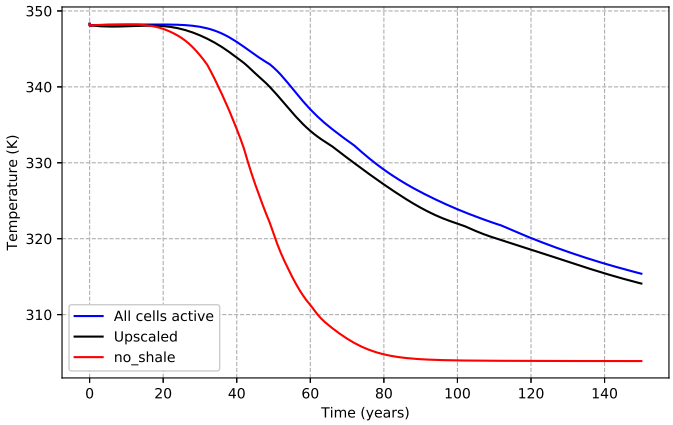

Figure 75: Temperature at the producer well versus time for multiple sub-region upscaling of non-reservoir cells - Model 2 (Experiment 4)

From both Figure 74 and Figure 75 it can be observed that the implementation of time variable thermal transmissibility has a highly positive impact on the quality of the upscaled solution when compared to that observed in Figure 72a. Similarly, in comparison to both the local and flow-based upscaling methods, the solutions for the multiple sub-region upscaling are much closer to the actual fine grid solution. However, not only is the quality of the solution considerably better but because the method only uses 10 different temperature brackets which upscales into 10 different cells, the total number of cells in the simulation is massively reduced when compared to the local or flow-based methods described in Sections 6.2 and 6.3. This method therefore has the potential to greatly reduce total simulation runtimes.

Although the method represents a large improvement in solution relative to the other methods, the solution is still not a perfect match and in both models tends to sit to the left of the full grid case. The results of Experiment 5 show that the quality of the solution is very strongly linked to the flow rate of the simulation, with the match of the solution improving as the flow rate increases (Figure 76).

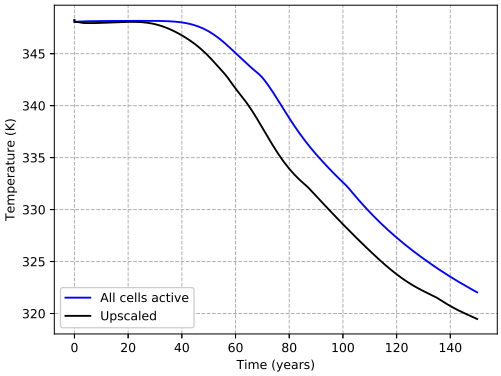

(a) Simulation 1: pressure differential between wells = 30 bar

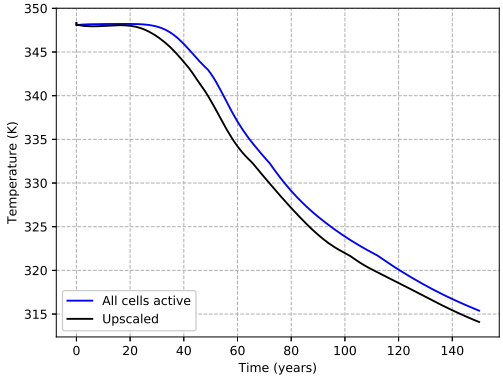

(b) Simulation 2: pressure differential between wells = 40 bar

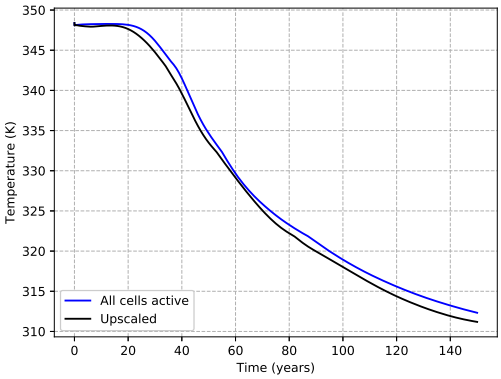

(c) Simulation 3: pressure differential between wells = 50 bar

Figure 76: Effect of changing the flow rate on the multiple-sub region upscaled solution accuracy (Experiment 5).

The reason for the strong link between solution quality and flow rate is again related to assumptions made within the method section. The initial simulation is run in such a way so that cold water completely surrounds the non-reservoir lithology, mimicking a situation where the cold front has passed and the water next to the shale is at, or close to, injection temperature. Therefore, the upscaling will work well if this is the case in the real simulation. If the flow rate is high, then the thermal front is steep and so at a given connection the water of the cell will go from initial reservoir temperature (in which case the connection will be closed) to injection temperature very quickly. This in turn means that the heat flow from the upscaling is valid. However, if flow rate is low, then the thermal front is very diffuse and the temperature of a reservoir cell at a given connection may take a long time to reach the injection temperature. During this transient period, the heat flow will not be accurate. With this said, this upscaling method should not be used in systems where the flow rate is slow and conduction is dominant.

Application of the multiple sub-region method to a heterogeneous geological model, is beyond the scope of this thesis and therefore has not been implemented. However, despite the fact that the method has not been implemented, a prediction on the suitability of the method for the geological grid can be made on based on a comparison of pressure and reservoir characteristics from the synthetic models and the real models. Figure 77 shows the production well and injection well BHP vs time curves for the across graben doublet configuration in the Base Case small grid (for configuration see Figure 27). The grid was run with constant initial temperature and pressure. Based on the fact that Figure 76c has a well matched solution between the upscaled and fine grids, then we would expect

that if the pressure differential between the wells in the real geological grid is the same and the N/G, reservoir thickness and distance between the wells is similar, then the flow rates within the two models should not be significantly different and thus the multiple sub-region upscaling should work relatively well. We can see from Figure 77, that the pressure differential between the wells is in excess of 50 bars (higher than that for Simulation 3 or Experiment 5) and the distance between the wells in the geological model is actually smaller (1.3km as opposed to 1.7km in the Model 2). The reservoir is slightly thicker in the geological model (~100m for the goelogical model vs ~75m for Model 1 and Model 2), however, despite this, the flow rates in the two models should be comparable. If this is the case, then the upscaling should be well suited for implementation onto the geological model.

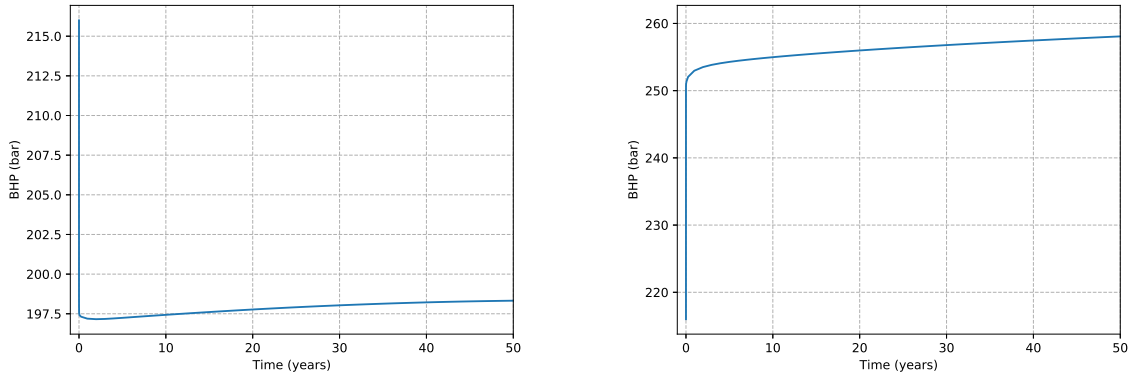

(a) Producer well

(b) Injector well

Figure 77: BHP vs time for wells aligned across the graben in the small grid. Wells are rate controlled.

6.5 Comparison of the Upscaling Methods

Within Sections 6.2, 6.3 and 6.4, the implementation, results and the science of the upscaling methods has been discussed in detail. However, comparison between the results of the different upscaling methods has mostly been qualitative. In this section we conduct a detailed quantitative comparison between the three upscaling solutions and draw conclusions regarding the utility of the three methods. For a quantitative measure of the solution accuracy relative to the fine grid, a normalised root mean square error is used (equation 26). This is effectively a measure of how close the upscaled solution is to the real solution, with 0 being a perfect match.

$$NRMSE = \frac{\sqrt{\frac{\sum_{i=1}^{N}(y_i - y_i^f)^2}{N}}}{\max(y^f) - \min(y^f)} \tag{26}$$

Where: $NRMSE$ = normalised root mean square error, N is the number of data points, y_i is the ith data point of the upscaled solution and y^f is the fine grid solution.

Table 13 shows the NRMSE of the upscaled solutions for the major simulation runs. It also shows the approximate number of upscaled cells which are present for the upscaled solutions and the reduction in number of cells achieved via the upscaling. From Table 13, it is clear that the only solutions which are close to the fine scale solution (low NRMSE), are those from the 2x2x2 flow-based upscaling and the multiple sub-region upscaling with time-variable thermal transmissibility implemented. If we compare these two solutions though, there is a stark difference in the reduction in number of cells in the model, with the flow-based 2x2x2 upscaling only reducing numbers of cells in the model by 5.5 times whilst the multiple-sub-region upscaling reduces the number of cells by a factor of 281.6. This suggests that multiple sub-regions upscaling has the potential to very significantly reduce simulation times whilst flow-based does not. Other trends which have been identified in Section 6.2 through to 6.4 which are reflected in Table 13, is the large rise in error of solution for both flow based and local upscaling as the size of the upscaled cells is increased and the generally higher errors of the local upscaling.

Simulation	**Normalised root mean squared error**	**Number of upscaled cells (approx)**	**Reduction in number of non-reservoir cells (original number of non-reservoir cells/number of upscaled cells)**
Local - 10x10x2	0.415	48	136.4
Local - 6x6x2	0.253	140	46.8
Local - 2x2x2	0.052	1200	5.5
Flow-based - 10x10x2	0.148	48	136.4
Flow-based - 6x6x2	0.091	140	46.8
Flow-based - 2x2x2	0.026	1200	5.5
Multiple sub-region - no time variable thermal transmissbility (Model1)	0.081	10	281.6
Multiple sub-region - time variable thermal transmissbility (Model 1)	0.020	10	281.6

Table 13: Normalised root mean square error and upscaling efficiency for the different upscaling methods.

From this section, we conclude that whilst local upscaling is easy to implement computationally and potentially very fast, it should not be used for modelling heat transfer from non-reservoir lithologies due to significant inaccuracies which become exaggerated as the size of the upscaled body increases. Flow-based upscaling can be used to solve the problem of inaccurate heat transfer, however very large numbers of upscaled cells are required to make the assumptions used in the flow-based upscaling method valid and the solution accurate. This makes computational savings of this method minimal. Finally, the multiple sub-regions method can produce low error solutions and result in a large reduction in the numbers of grid cells. However, the quality of the solution is still linked to flow rate and the implementation of this method is complex and therefore, further work is required to test this method on heterogeneous grids.

7 Conclusions

The large scale development of the Netherlands' low enthalpy geothermal resources has the potential to significantly contribute to the energy mix of the Netherlands and reduce Dutch reliance on natural gas (*Master Plan: Geothermal Energy in the Netherlands* 2018). Futhermore, the use of a play/portfolio based approach to development could markedly reduce costs and risks associated with developing these geothermal resources. Central to this approach is geological modelling and dynamic reservoir simulation which can be used to forecast how geothermal systems may behave under production and what risks and problems may be faced. This thesis, using the example of the Delft Sandstone in the West Netherlands Basin, has examined a number of factors important to simulation of geothermal reservoirs, including: uncertainty and sensitivity of the simulations to geological input parameters, the effect of well position on performance and the effect and efficient simulation of non-reservoir lithologies. The primary findings of the thesis are given below:

- Examination of the literature, well log data and seismic data indicates that the Delft Sandstone is a dual-layer fluvial reservoir which changes in quality both vertically and horizontally across three half-grabens, with the quality of reservoir believed to be linked to the movement of the major fluvial trunk systems throughout geological time. This information has been used to construct a representative 3D geological model of the Delft Sandstone in three inverted half-grabens.
- In the absence of appropriate petrophysical log data (neutron porosity and density) inside the geological model boundaries, using a gamma-porosity correlation to estimate the porosity represents a reasonably effective and accurate method of porosity derivation, as shown by the fact that permeability values match well with well test results.
- Sensitivity and uncertainty analysis shows that the value and distribution of porosity and the intrinsically linked permeability, are the most important factors in controlling time of thermal breakthrough and uncertainty, more so than reservoir architecture. This only holds true in the high N/G Delft Sandstones, if looking at lower N/G fluvial reservoirs, the size of channel belts and particularly whether they connect are known to be factors of paramount importance.
- Well configuration analysis suggests that line-drive configured doublets perform better than diagonally configured doublets in steeply dipping sections of the reservoir, whilst the more even pressure distribution generated by the diagonal well configuration is favourable in flatter and thicker parts of the reservoir. This leads to the suggestion that optimum well configuration needs to be decided on a case-by-case basis.
- For geothermal wells especially, small increases in injector-producer well separation can lead to large gains in breakthrough time due to the massively increased area available to flow (reducing Darcy velocity) and thermal recharge. Additionally, for line-drive configured wells, doublets can be moved closer without a large reduction in breakthrough time (unlike diagonally configured wells) however there are significant local pressure changes if in-line wells are moved too close (<1km).
- Geological anisotropy caused by alignment of the meander belts along the graben axes causes thermal breakthrough to occur on average ~1.4 times slower when doublets are aligned across the axis as opposed to along the axis.
- Non-reservoir lithologies play a vital role in thermally recharging injected water and preventing thermal breakthrough. Unlike in simulations for oil/gas developments, they cannot be excluded.
- An investigation into the use of local upscaling techniques for simulating thermal conduction from non-reservoir lithologies suggests that whilst these techniques might be applicable for simple flow simulations, they are not easily applied to heat transfer. The results show that heat flow out of the upscaled volumes was too large when compared to fine grid simulations.
- Use of flow-based techniques provided improved results compared to the local method because recalculation of upscaled thermal transmissibilities allowed more accurate simulation of total heat flow from the non-reservoir lithologies. However, finding a set of thermal transmissibilities which are representative for the entire time is not possible and so for large upscaled volumes, accurately representing breakthrough times using standard flow-based methods is not possible.

- Multi-sub region techniques applied on synthethic models show promising results for efficiently upscaling non-reservoir lithologies, although the quality of the results is strongly linked to flow rate, with faster flow rates providing more accurate solutions.

8 Recommendations

The breadth of the topics covered within this thesis means that there are a number of areas for further work, both in improving the current work and conducting additional studies.

A primary area where the workflow could be improved is the uncertainty analysis. As mentioned in section 4.4.2, only 20 realisations were used for each of the experiments. This is not enough to get an idea of the true range of uncertainty associated with the Delft Sandstone, however, in this case the work was limited by the segregated nature of PETREL and DARTS. Ideally, for future uncertainty analysis a more efficient interfacing method would be developed, allowing a full Monte-Carlo style uncertainty analysis to be conducted with hundreds of realisations generated, covering all aspects of uncertainty.

Further work is also required in implementing upscaling techniques. It was beyond the scope of this thesis to implement the multiple-upscaling methods on a heterogeneous grid. However, in future, this method should be implemented on a realistic model and tested to further check the method's robustness and assess the quality of solution. Additionally, the upscaling technique needs refining such that the efficiency of the pre-processing for the simulations is significantly increased.

In terms of further development of studies involving low enthalpy geothermal reservoir simulation, a key step is the implementation of history matching studies. History matching is a well established and developed field of study in the oil and gas industry and the benefits of carrying out history matching are well documented (Cancelliere et al., 2011). However, history matching of geothermal reservoirs has mainly been confined to high enthalpy reservoirs (Pritchett et al., 1980; Yoshinobu et al., 1984) and little work (especially in the Netherlands) has focused on low enthalpy projects. The primary reason for this is the lack of data from existing doublets which is publically available. To do proper history matching studies, ideally one would have data from several producer and injector wells (although any amount of production data has significant utility). The matching of results from the simulator with real data from geothermal wells would help give considerable weight to the findings of studies such as this one. It would also serve to both improve our understanding and estimate of the uncertainty as well as increase the accuracy of geological models of the subsurface.

References

Awadalla, T. and Voskov, D. (2018). "Modeling of gas flow in confined formations at different scales". In: *Fuel* 234, pp. 1354–1366.

Cancelliere, M., Verga, F., and Viberti, D. (Jan. 2011). "Benefits and Limitations of Assisted History Matching". In: *Society of Petroleum Engineers - Offshore Europe Oil and Gas Conference and Exhibition 2011, OE 2011* 2. DOI: 10.2118/146278-MS.

Chandrasekharam, D. and Bundschuh, J. (2008). *Low-enthalpy geothermal resources for power generation*. Vol. 149. CRC press Leiden.

Collinson, J.D. (1977). "Vertical sequence and sand body shape in alluvial sequences". In: *Dallas Geological Society*.

Crain, E.R. (2002). *Crain's petrophysical handbook*. Spectrum 2000 Mindware Limited.

Crooijmans, R.A., Willems, C.J.L., Nick, H.M., and Bruhn, D. (2016). "The influence of facies heterogeneity on the doublet performance in low-enthalpy geothermal sedimentary reservoirs". In: *Geothermics* 64, pp. 209–219.

Den Hartog Jager, D.G. (1996). "Fluviomarine sequences in the Lower Cretaceous of the West Netherlands Basin: correlation and seismic expression". In: *Geology of gas and oil under the Netherlands*. Springer, pp. 229–241.

DeVault, B. and Jeremiah, J. (Oct. 2002). "Tectonostratigraphy of the Nieuwerkerk Formation (Delfland Subgroup), West Netherlands Basin." In: *AAPG Bulletin* 86, pp. 1679–1707.

Dongen, B. van (2019). *The economic potential of deep, direct use geothermal systems in the Netherlands*. Delft University of Technology.

Donselaar, M.E., Groenenberg, R.M., and Gilding, D.T. (2015). "Reservoir geology and geothermal potential of the Delft Sandstone Member in the West Netherlands Basin". In: *Proceedings World Geothermal Congress*.

Donselaar, M.E. and Schmidt, J. (Sept. 2005). "Integration of outcrop and borehole image logs for high-resolution facies interpretation: Example from a fluvial fan in the Ebro Basin, Spain". In: *Sedimentology* 52, pp. 1021–1042. DOI: 10.1111/j.1365-3091.2005.00737.x.

Duin, E.J.T., Doornenbal, J.C., Rijkers, R.H.B., Verbeek, J.W., and Wong, T.E. (2006). "Subsurface structure of the Netherlands-results of recent onshore and offshore mapping". In: *Netherlands Journal of Geosciences* 85.4, p. 245.

Fielding, C.R. and Crane, R.C. (1987). "An application of statistical modelling to the prediction of hydrocarbon recovery factors in fluvial reservoir sequences". In: *Special Publications of SEPM*.

Fofonoff, N.P. and Millard Jr, R.C. (1983). "Algorithms for the computation of fundamental properties of seawater." In: *Technical Papers in Marine Science*.

Foix, N., Paredes, J.M., and Giacosa, R.E. (2013). "Fluvial architecture variations linked to changes in accommodation space: Río Chico Formation (late Paleocene), Golfo San Jorge basin, Argentina". In: *Sedimentary Geology* 294, pp. 342–355.

Groot, J. (2014). *The Role of Reservoir Geology and Reservoir Architecture on Geothermal Doublet Performance*. University of Utrecht.

Hansen, J., Sato, M., Ruedy, R., Lo, K., Lea, D.W., and Medina-Elizade, M. (2006). "Global temperature change". In: *Proceedings of the National Academy of Sciences* 103.39, pp. 14288–14293.

ING Economics Department (2018). https://www.ing.nl/media/ING_EBZ_Focus_on_Dutch_climate_20challenge-May_2018_tcm162-147579.pdf. Accessed: 2019-07-21.

Jager, J. de, Doyle, M.A., Grantham, P.J, and Mabillard, J.E. (Sept. 1993). "Hydrocarbon habitat of the West Netherlands Basin". In: vol. 77. DOI: 10.1007/978-94-009-0121-6_17.

Jeremiah, J.M., Duxbury, S., and Rawson, P. (2010). "Lower Cretaceous of the southern North Sea Basins: reservoir distribution within a sequence stratigraphic framework". In: *Netherlands Journal of Geosciences - Geologie en Mijnbouw* 89.3-4, pp. 203–237. DOI: 10.1017/S0016774600000706.

Karimi-Fard, M. and Durlofsky, L. (2012). "Accurate resolution of near-well effects in upscaled models using flow-based unstructured local grid refinement". In: *SPE Journal* 17.04, pp. 1–084.

Khait, M. and Voskov, D. (2017). "Operator-based linearization for general purpose reservoir simulation". In: *Journal of Petroleum Science and Engineering* 157, pp. 990–998.

Khait, M. and Voskov, D. (2018). "Operator-based linearization for efficient modeling of geothermal processes". In: *Geothermics* 74, pp. 7–18.

Loerakker, M. (2009). *A core study to determine the heterogeneities in the Delft Sandstone Member in the Moerkapelle Field*. Delft University of Technology.

Lorenz, J.C., Heinze, D.M., and Clark J.A.and Searls, C.A. (1985). "Determination of widths of meander-belt sandstone reservoirs from vertical downhole data, Mesaverde Group, Piceance Creek basin, Colorado". In: *AAPG Bulletin* 69.5, pp. 710–721.

Master Plan: Geothermal Energy in the Netherlands (2018). https://geothermie.nl/images/bestanden/Masterplan_Aardwarmte_in_Nederland_ENG.pdf.

Netherlands Climate Policy (2019). https://www.government.nl/topics/climate-change/eu-policy. Accessed: 2019-07-21.

O'Sullivan, M.J., Pruess, K., and Lippmann, M.J. (2001). "State of the art of geothermal reservoir simulation". In: *Geothermics* 30.4, pp. 395–429.

Pritchett, J., Rice, L., and Garg, S. (Jan. 1980). *Reservoir simulation studies: Wairakei Geothermal Field, New Zealand. Final report*. Lawrence Berkeley National Laboratory. DOI: 10.2172/6779927.

Qi, D. and Hesketh, T. (2005). "An Analysis of Upscaling Techniques for Reservoir Simulation". In: *Petroleum Science and Technology* 23.7-8, pp. 827–842.

Shetty, S., Voskov, D., and Bruhn, D. (2017). "Numerical Strategy for Uncertainty Quantification in Low Enthalpy Geothermal Projects". In: *43rd Workshop on Geothermal Reservoir Engineering*.

Van Dalfsen, W., Doornenbal, J.C., Dortland, S., and Gunnink, J.L. (2006). "A comprehensive seismic velocity model for the Netherlands based on lithostratigraphic layers". In: *Netherlands Journal of Geosciences* 85.4, pp. 277–292.

Veldkamp, H., Brunner, L., Jong, S. de, Heijnen, N., Langen, C. van, and Wees, J.D. van (2019). "Play-based portfolio approach for geothermal development". In: *European Geothermal Congress*.

Voskov, D. (2017). "Operator-based linearization approach for modeling of multiphase multi-component flow in porous media". In: *Journal of Computational Physics* 337, pp. 275–288.

Wang, Y., Khait, M., Voskov, D., and Bruhn, D. (Feb. 2019). "Benchmark test and sensitivity analysis for Geothermal Applications in the Netherlands". In: *44th Workshop on Geothermal Reservoir Engineering*.

Wang, Y. and Voskov, D (2019a). personal communication.

Wang, Y. and Voskov, D. (2019b). "Paper on the role of non-reservoir lithologies in low enthalpy geothermal systems".

Werker, C., Ubacht, J., and Ligtvoet, A. (2017). "Networks of entrepreneurs driving the Triple Helix: two cases of the Dutch energy system". In: *Triple Helix* 4.1, pp. 1–25.

Wiggers, C. (2017). *The Delft Sandstone in the West Netherlands Basin*. Delft University of Technology.

Willems, C.J.L. (2017). "Doublet deployment strategies for geothermal Hot Sedimentary Aquifer exploitation: Application to the Lower Cretaceous Nieuwerkerk Formation in the West Netherlands Basin". PhD thesis. Delft University of Technology.

Willems, C.J.L., Vondrak, A., Munsterman, D.K., Donselaar, M.E., and Mijnlieff, H. (Dec. 2017). "Regional geothermal aquifer architecture of the fluvial Lower Cretaceous Nieuwerkerk Formation - A palynological analysis". In: *Netherlands Journal of Geosciences* 96, pp. 319–330. DOI: 10.1017/njg.2017.23.

Wong, T.E., Batjes, D.A.J., and Jager, J. de (2007). *Geology of the Netherlands*. Edita-the Publishing House of the Royal.

Yoshinobu, F., Shinji, Y., and Seiichi, H. (1984). "History Matching in a Geothermal Reservoir". In: *Journal of the Geothermal Research Society of Japan* 6.1, pp. 33–42. DOI: 10.11367/grsj1979.6.33.

9 Appendices

9.1 Appendix A

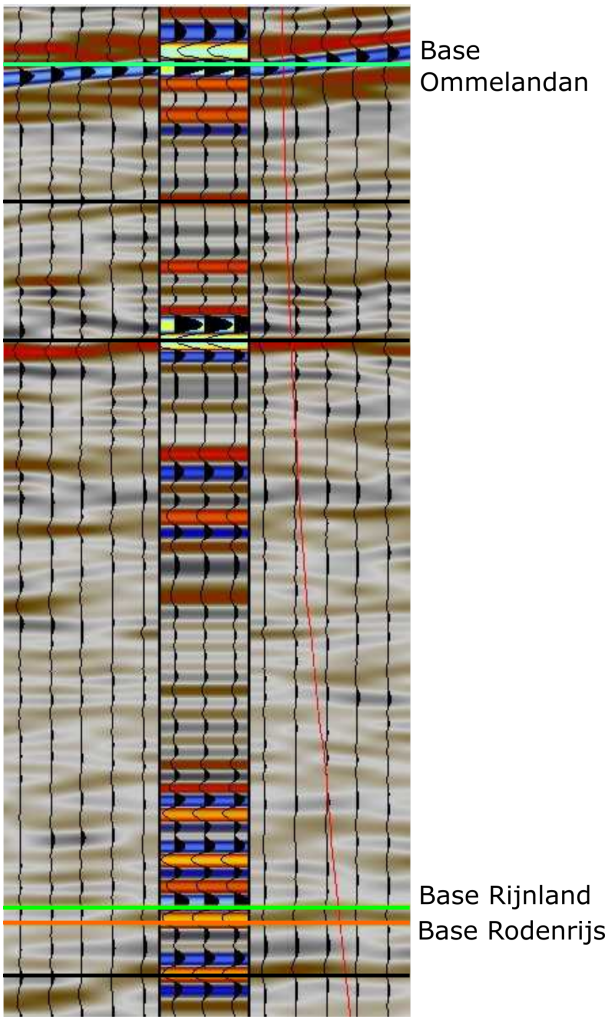

Figure 78: The synthetic seismic for well KDZ-02-S1 showing how the well tops match with reflectors in the seismic section.

Geological Group	**K(s^{-1})**
North Sea	0.288
Ommelandan	0.882
Rijnland	0.492
Schieland	0.658

Table 14: Velocity gradient (K) values for the four relevant geological units taken from work by Van Dalfsen et al. (2006)

Author and Formation	Sandstone body stratigraphic thickness (m)	Channel depth(m)	Meander Belt Width (m)		
			Collins, 1977	Fielding and Crane, 1987	Lorenz et al., 1985
Loerakker, 2009 Delft Sandstone	3.54	2.7435	448.3787248	301.772641	368.4059291
	4.13	3.20075	568.5164736	376.1956529	468.2261314
	3.62	2.8055	464.0782049	311.5720235	381.4364994
	3.86	2.9915	512.3000794	341.5270011	421.4876278
	5.15	3.99125	798.6621569	515.8097374	660.0121059
	5.85	4.53375	971.8517203	618.9250885	804.7132856
	6	4.65	1010.492047	641.7435125	837.0345647
Donselaar and Schimdt, 2005 Huesca Alluvial Fan	3.7	2.8675	479.9661716	321.4649771	394.6280023
	5	3.875	763.1216603	494.4612986	630.3545357
	3.3	2.5575	402.4310126	272.9481361	330.2961561
	5.7	4.4175	933.7427692	596.3568918	772.8490686
	3.7	2.8675	479.9661716	321.4649771	394.6280023
	7.5	5.8125	1424.866971	882.9636109	1184.342261
	2.5	1.9375	262.426439	183.5098631	214.4681605
	3.8	2.945	500.0883217	333.9609918	411.3413258
	4.5	3.4875	648.8245067	425.3036341	535.073794
	7	5.425	1281.241377	800.0099641	1063.830479
	3.8	2.945	500.0883217	333.9609918	411.3413258
	4.3	3.3325	604.9526668	398.533736	498.5443206
Jeremiah et al., 2010 Rodenrijs	5	3.875	763.1216603	494.4612986	630.3545357
	2	1.55	186.1084822	133.3761241	151.5754941
	2.5	1.9375	262.426439	183.5098631	214.4681605
	2.5	1.9375	262.426439	183.5098631	214.4681605
	3	2.325	347.4935167	238.1708426	284.7877714
max	7.5	5.8125	1424.866971	882.9636109	1184.342261
min	2	1.55	186.1084822	133.3761241	151.5754941
mean	4.88	3.292135417	619.8988472	404.3963634	511.6111541

Table 15: Table showing recorded point bar depths and the corresponding meander belt widths given the different empirical relations of Collinson (1977), Fielding and Crane (1987), and Lorenz et al. (1985).

Horner Plot Analysis

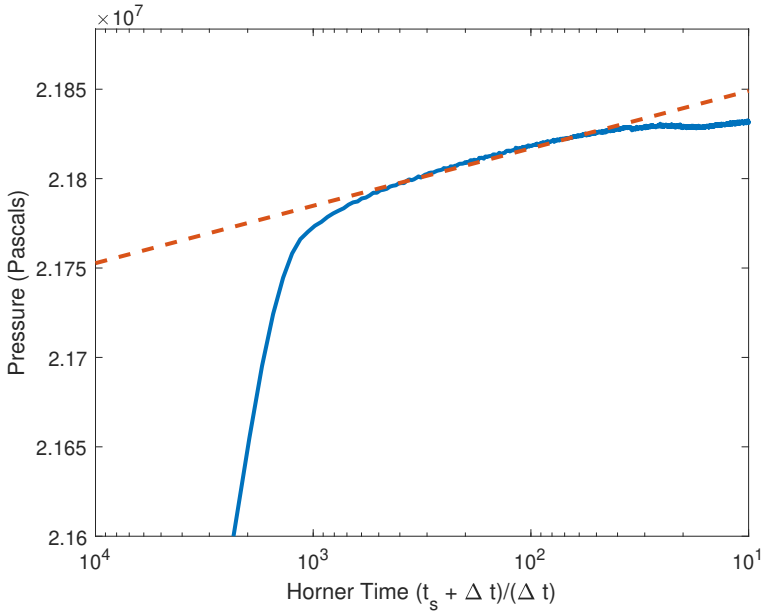

Figure 79: Horner Plot for well A, the real pressure data is shown in blue, the line fitted to the radial flow period is shown in red. The slope of the red line can be used to calculate permeability.

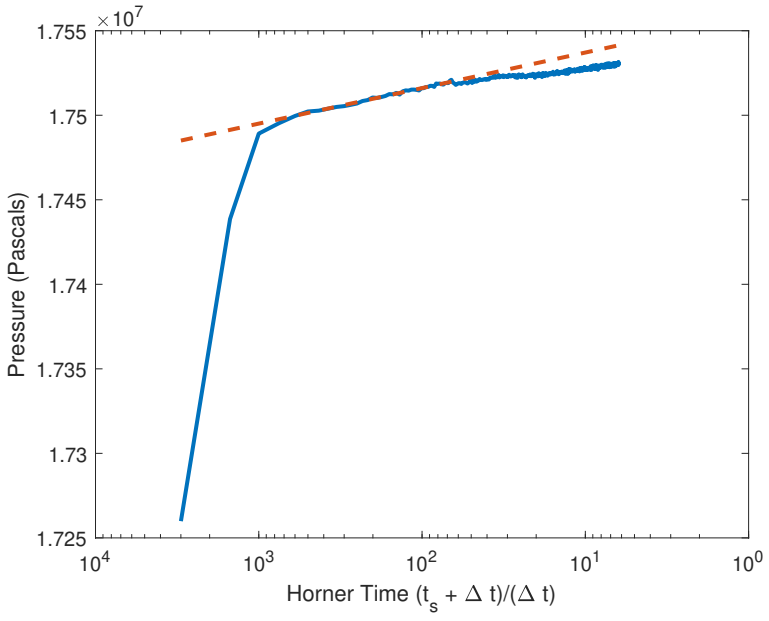

Figure 80: Horner Plot for well B, the real pressure data is shown in blue, the line fitted to the radial flow period is shown in red. The slope of the red line can be used to calculate permeability.

The method for calculating permeability is as follows:

- A line is fitted to the straight line (radial flow portion) of the real data.
- the equation of the line is:

$$P = P_i - \frac{Q_0 \mu}{Kh}[log(\frac{t_s + \Delta t}{\Delta t})] \tag{27}$$

- The slope(m) is therefore given by: $-\frac{Q_0 \mu}{Kh}$
- Given viscosity, height of reservoir and flow rate at shut in, the permeability can be calculated.

9.2 Appendix B

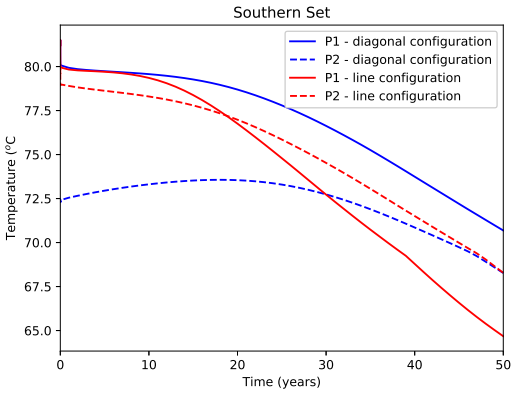

(a) Southern set

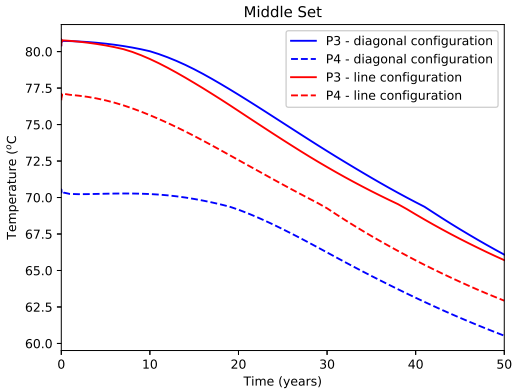

(b) Midde set

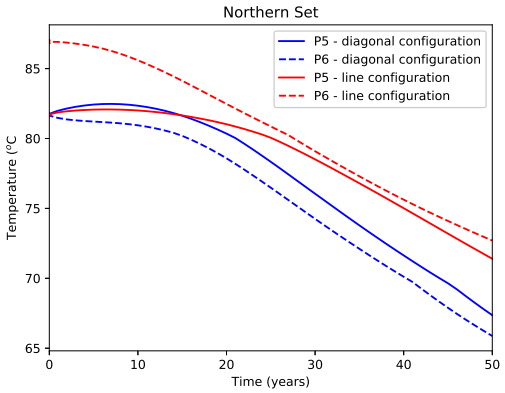

(c) Northern set

Figure 81: Temperature at the production wells vs time for different well sets as part of the well configuration experiments.

Model Parameter	**Value**
Grid size (-)	nx = 50
	ny = 50
	nz = 20
Cell dimensions (m)	dx = 100
	dy = 100
	dz = 5
Permeability (mD)	500
Porosity (-)	0.2
Thermal Conductivity ($W/m^{-1}K^{-1}$)	2.7
Initial pressure (bar)	216
Initial temperature (^oC)	75
Flow at boundary	open
Simulation runtime (years)	100
Max time step (years)	1

Table 16: Model parameters for the box model utilised in Section 5.2.

9.3 Appendix C

Model Parameter	Value
Grid Size (-)	nx = 60
	ny = 40
	nz = 4
Dimensions (m)	x = 1800
	y = 1200
	z = 10
Well Positions	Injector: i = 15 j = 20
	Producer: i = 45 j = 20
Porosity (-)	Shale: 0.01
	Sandstone: 0.15-0.37
Permeability (mD)	Shale: 0.001
	Sandstone: 6.3-3359.1
Thermal conductivity (Watts/$m^{-1}K^{-1}$)	2.7
Initial reservoir pressure (bar)	200
Initial reservoir temperature (^{o}C)	75
Well control (bar, ^{o}C)	Injector: 220, 30
	Producer:180
Flow at boundary	closed
Simulation runtime (years)	150
Max time step (years)	1

Table 17: Simulation parameters for the synthetic reservoir model.

Model Parameter	Value
Grid Size (-)	nx = 20
	ny = 20
	nz = 15
Dimensions (m)	x = 1100
	y = 1100
	z = 75
Well Positions	Injector: i = 1 j = 1
	Producer: i = 20 j = 20
Porosity (-)	Shale: 0.01
	Sandstone: 0.2
Permeability (mD)	Shale: 0.001
	Sandstone: 500
Thermal conductivity (Watts/$m^{-1}K^{-1}$)	2.7
Initial reservoir pressure (bar)	216
Initial reservoir temperature (^{o}C)	75
Well control (bar, ^{o}C)	Injector: 231, 30
	Producer:201
Flow at boundary	closed
Simulation runtime (years)	150
Max time step (years)	1

Table 18: Simulation parameters for Model 1.

Model Parameter	Value
Grid Size (-)	nx = 39
	ny = 39
	nz = 15
Dimensions (m)	x = 1170
	y = 1170
	z = 75
Well Positions	Injector: i = 1 j = 1
	Producer: i = 39 j = 39
Porosity (-)	Shale: 0.01
	Sandstone: 0.2
Permeability (mD)	Shale: 0.001
	Sandstone: 500
Thermal conductivity (Watts/$m^{-1}K^{-1}$)	2.7
Initial reservoir pressure (bar)	216
Initial reservoir temperature (^{o}C)	75
Well control (bar, ^{o}C)	Injector: 236, 30
	Producer:196
Flow at boundary	closed
Simulation runtime (years)	150
Max time step (years)	1

Table 19: Simulation parameters for Model 2.

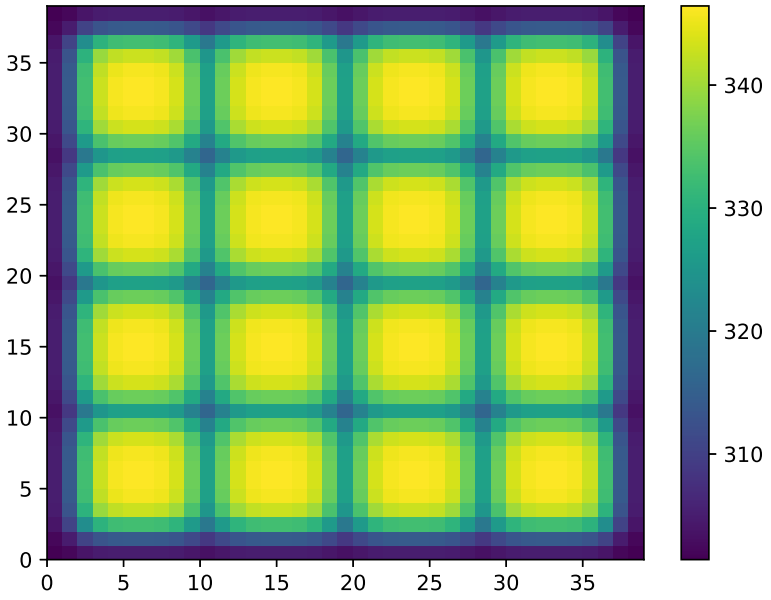

Figure 82: Temperature distribution after initial simulation - Model 2.

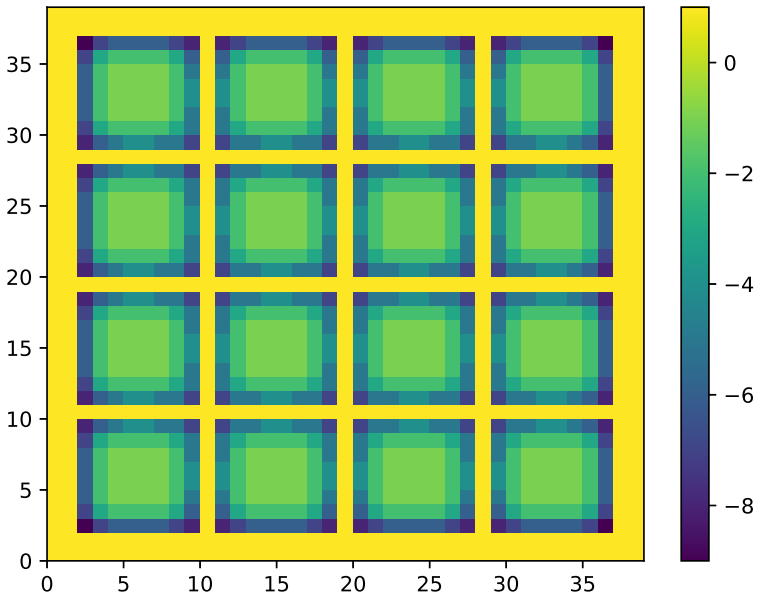

Figure 83: Sub-regions - Model 2.